Stony Brook University

Investigation of the Series Connection of Silicon Photomultipliers for Reduced Noise Readout in Cryogenic Environments

A Thesis presented

by

Eric Raguzin

to

The School of Electrical and Computer Engineering

in Partial Fulfillment of the

Requirements

for the Degree of

Master of Science

in

Electrical Engineering

Stony Brook University

August 2016

Stony Brook University

School of Electrical and Computer Engineering

Eric Raguzin

We, the thesis committe for the above candidate for the

Master of Science degree, hereby recommend

acceptance of this thesis

Harbans S. Dhadwal
Associate Professor - Department of Electrical and Computer Engineering

Leon Shterengas
Associate Professor - Department of Electrical and Computer Engineering

This thesis is accepted by the Graduate School

Nancy Goroff
Interim Dean of the Graduate School

Abstract of the Thesis

Investigation of the Series Connection of Silicon Photomultipliers for Reduced Noise Readout in Cryogenic Environments

by

Eric Raguzin

Master of Science

in

Electrical Engineering

Stony Brook University

2016

Silicon Photomultipliers (SiPMs) are devices capable of achieving the single photon resolution required over the large area (4 m^2) required for the next Enriched Xenon Observatory (nEXO) experiment. In addition, SiPMs function with lower noise at cryogenic temperatures in the range that will be used in the full scale experiment, demonstrating a significant drop in the noise of the sensor. nEXO requires a large photosensitive area inside the time projection chamber (TPC) due to the increased mass of Xenon expected when compared with the previous EXO experiment. Practically implementing a photosensitive area of this scale requires consolidation of multiple SiPMs into fewer readout channels in order to minimize power draw and required electrical connections of the SiPM readout system while maintaining an acceptable photon resolution.

SiPMs were procured to study the photon counting resolution achievable with various connection schemes (series, parallel, or a hybrid of the two) in order to reduce the number of required electronic readout channels. A test setup was assembled in which pulsed light of a controllable frequency and flux were incident on a fixture holding one or multiple SiPMs. Experimental data showed that the series configuration of SiPMs is able to measure the incoming light down to the single photon level. The gain of the series SiPM array agreed with theoretical predictions, although biasing resistors were required to obtain a resolution acceptable for the nEXO experiment.

Table of Contents

List of Figures/Tables/Illustrations

Acknowledgements

I would like to acknowledge Gianluigi De Geronimo, for allowing me to pursue this Master's Degree. I would also like to thank Veljko Radeka for providing me with the opportunity to take on a successful internship at Brookhaven National Laboratory. I would like to thank Harbans Dhadwal for agreeing to serve as my academic advisor and Leon Shterengas for serving as a second reader. I would like to thank Sergio Rescia for an infinite amount of guidance and knowledge, as well as patience. I would also like to thank Hucheng Chen and Thomas Tsang for their incredible helpfulness and patience as well. I would also like to acknowledge Tutu Wan for a a variety of software assistance. Bill Smith, Don Pinelli, Bill King, Kevin Wolniewicz, Kim Ackley, Albert Lum, Anand Kandasamy, Ken Sexton, Gabriele Giacomini, Neena Nambiar and Shaorui Li were also critical in performing the work described in this thesis.

Chapter 1

Introduction

1.1 The nEXO experiment

The nEXO experiment is the next generation of the EXO-200 prototype experiment currently being carried out underground in Carlsbad, New Mexico. EXO (Enriched Xenon Observatory) is an attempt to observe neutrinoless double beta decay ($0\nu\beta\beta$) as opposed to the fully described and measured standard double beta decay ($2\nu\beta\beta$). The detection of $0\nu\beta\beta$ in this experiment would have significant scientific merit by proving that neutrinos are their own antiparticles (and thus Majorana fermions), as well as establishing bounds on the absolute mass of the neutrino.

1.2 Physics Background

1.2.1 Beta Decay and Double Beta Decay

Beta (β) decay is a phenomenon caused by the weak force in which either an atom's nucleus loses a neutron and gains a proton, emitting an electron and electron antineutrino (β^- decay), or loses a proton and gains a neutron, emitting a positron and electron neutrino (β^+ decay).

β decay is only possible when the resulting nucleus has a lower rest mass than the original nucleus. Through different permutations of elements and isotopes, a given nucleus' β decay may not physically be possible due to the higher rest mass of the resulting nucleus. However, if two β decays would result in a nucleus with a lower rest mass, then double beta ($\beta\beta$) decay is physically allowed and would include losing two neutrons, gaining two protons, and emitting two electrons and two electron antineutrinos in a single event.

During β and $\beta\beta$ decay, the total energy from the event is distributed probabalistically between the emitted particles and the recoiling nucleus, although the kinetic energy of the

nucleus is generally negligible. This results in a variation of the energy of the emitted electron and neutrino for each specific decay, although the total energy released, the Q value, must always be constant.

1.2.2 Neutrinoless Double Beta Decay

While the original Standard Model of Particle Physics assumed that neutrinos have no mass, experimental evidence of neutrino oscillation has proved that they do (Westerdale, 2010). One remaining uncertainty related to neutrinos is the question of whether they are their own antiparticle, which would classify them as Majorana Fermions. A consequence of the neutrino being a Majorana Fermion would be that during $\beta\beta$ decay, the emitted neutrinos or antineutrinos have a non-zero probability of annihalating each other, in essence both being absorbed by the nucleus (Avignone, Elliot, and Engel, 2008). The probability of this event would be proportional to the mass of the neutrino. In this case of $0\nu\beta\beta$, the two electrons would be emitted with the full Q value of the decay. Measuring the energy of emitted electrons in standard $2\nu\beta\beta$ results in a distribution in which the difference between the Q value and the electron energy for any given event results in the energy that the neutrino must have been emitted with. If $0\nu\beta\beta$ is occuring, then one would expect some amount of measured electron energy at the full Q value. The blue distribution in Figure 1.1 shows what this should theoretically result in.

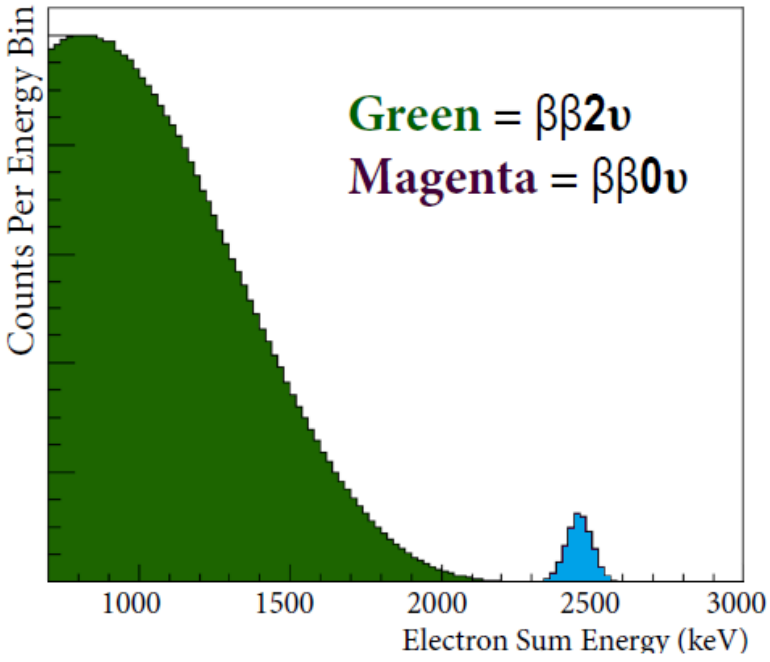

Figure 1.1: $\beta\beta$ energy distributions (Johnson, 2013)

1.2.3 Measuring the Emitted Energy

The EXO-200 experimental setup is in the form of a Time Projection Chamber (TPC), where 200 kg of liquid xenon is contained in a cryogenic chamber, enriched to 80% ^{136}Xe. ^{136}Xe is an isotope that cannot undergo β decay and whose decay is then forced to $\beta\beta$ decay. It was chosen for its relative ease of enrichment, as well as for its Q value, 2.48 MeV. The Q value is higher than common sources of background radiation and noise, which makes it easier to filter out readings not caused by $\beta\beta$ decay. Another reason is to complement ongoing research into "Barium tagging", which is the detection of the Barium ion that results from ^{136}Xe $\beta\beta$ decay. Barium tagging would allow rejection of background noise by confirming that $\beta\beta$ decay has actually occured for any given reading. The EXO-200 experiment is diagrammed in Figure 1.2.

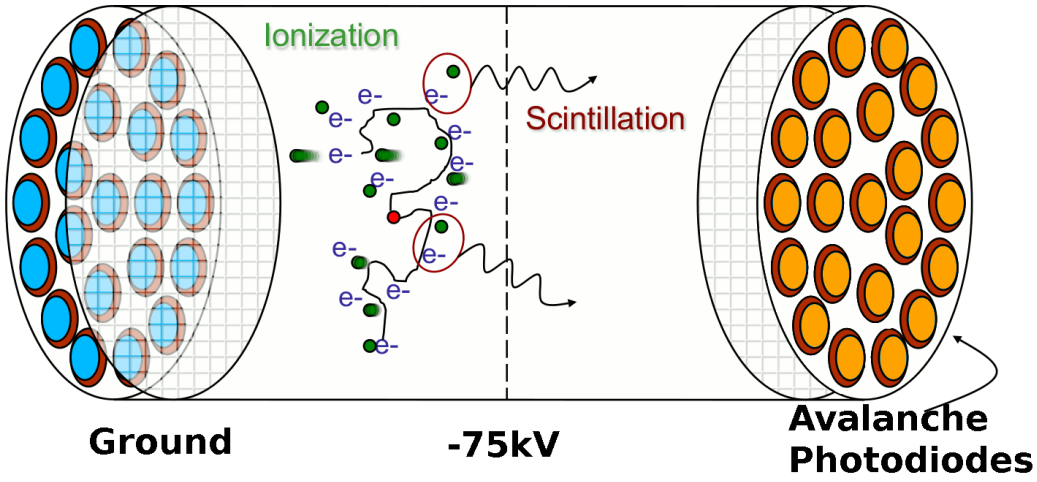

Figure 1.2: Concept of $\beta\beta$ decay detection in a liquid xenon TPC (*About EXO-200* 2015)

The mass of xenon is contained in a chamber with a -75 kV electric potential applied across it by field shaping rings to keep the electric field uniform, which leads to a consistent velocity for all free electrons. Since there is no known way of measuring any properties of a neutrino directly, the experiment is designed to measure the energy of the emitted electrons. When an electron is emitted, it immediately experiences the electric field and begins moving at a constant velocity towards the ground potential electrode. As the high energy electrons move through the xenon, they ionize other xenon nuclei, creating more free electrons that move towards the ground potential. Immediately after the initial ionization, some of the electrons will recombine with the positive xenon ions, a process which emits photons. The inside of the EXO-200 TPC is coated with reflector tiles to ensure that the photons are collected and measured at the end opposite of the ground potential - at the Avalanche Photodiode (APD) array. The electrons that do reach the ground potential electrode induce charge signals, and are collected, in wire grids. By summing the energy measured from the electrons and photons, one can find the total energy given off to the electrons in the $\beta\beta$ decay event, using the initial light signal as a time trigger for when the decay is initiated. The TPC is also used as an imaging detector to map the location of the ionization, with

the transverse coordinate calculated from the induced signals on the wire grids, and the longitudinal coordinate determined by the drift time based on the light trigger.

1.2.4 nEXO

While the EXO-200 experiment continues to be a success in establishing new bounds for the half life of $0\nu\beta\beta$ and has charactarized $2\nu\beta\beta$ decay in ^{136}Xe, greater mass, instrument resolution, and background suppression are needed to successfully identify the Q value peak that would be indicative of $0\nu\beta\beta$. A greater mass will increase the rate at which $2\nu\beta\beta$, and theoretically $0\nu\beta\beta$, will occur, allowing for a much shorter run of the experiment. Greater resolution will allow for more accurate data and a more constrained peak at the Q value. Finally, the suppression of background radiation is needed to prevent cosmic particles from causing false readings. The nEXO experiment ("Next EXO") is in the planning stages, and will improve on the initial concept in many ways, including a higher mass, 5,000 kg of liquid xenon, 90% enriched to ^{136}Xe, more stringent radiopurity requirements for all components, a new charge readout method, and a deeper underground site for the TPC, as seen in Figure 1.3. While EXO-200 is 1,500 feet underground, nEXO is proposed to be 6,000 feet underground in a mine in Sudbury, Ontario. This is expected to remove cosmic sources of background radiation by orders of magnitude.

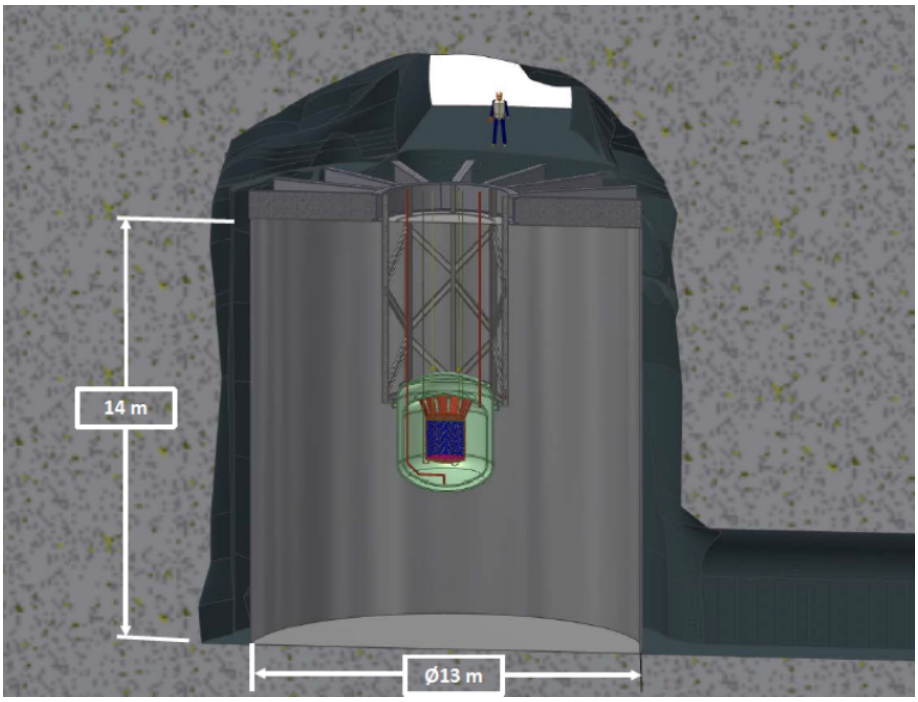

Figure 1.3: Conceptual art of the nEXO experiment (Gratta, 2014)

These various improvements are outside of the scope of this thesis. This thesis focuses specifically on the ongoing research in designing scalable arrays of the Silicon Photomultipliers (SiPMs) used to detect and measure the emitted scintillation. In the EXO-200

experiment, a significant amount of photons are not detected due to optical losses. Difficulties in scaling the effective area of the APDs has led to insufficient coverage of the chamber. nEXO is in the process of being designed for much more comprehensive SiPM coverage of the chamber, approximately 4 m^2 over the round surface of the cylindrical TPC, as seen in Figure 1.4.

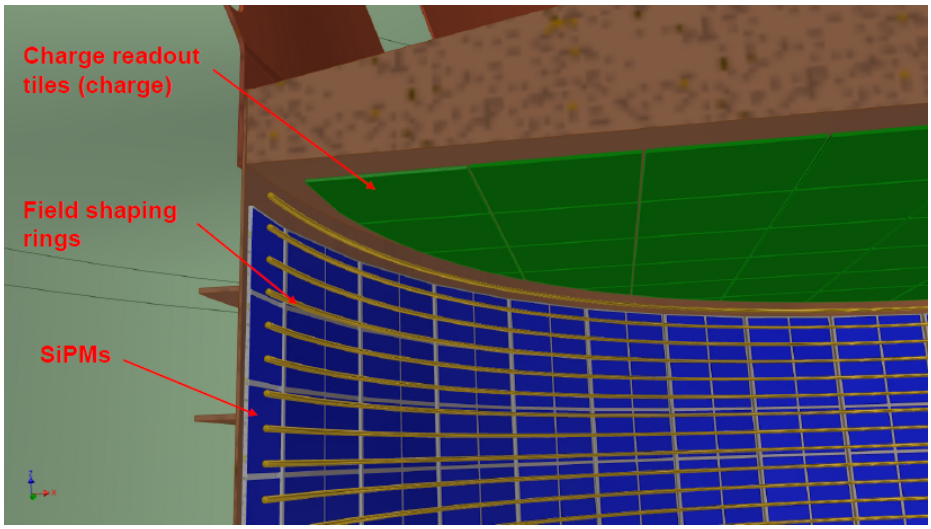

Figure 1.4: Conceptual art of the proposed readout systems for nEXO (Gratta, 2014)

SiPMs are a newer technology that allows multiple Single Photon Avalanche Diodes (SPAD) pixels to be connected together while operating in "Geiger" mode. However, connecting multiple SiPMs in parallel increases the total sensor capacitance, which in turn increases the readout noise. To minimize readout noise, study has been undertaken in connecting the SiPMs in various array schemes, notably being connected in series. These configurations would allow larger arrays to connected to a single amplifier and reduce the noise when the signal is read out.

Chapter 2 of this thesis provides a historical prospective and current theoretical understanding of single and multiple SiPMs. Chapter 3 details computer simulations that are undertaken to predict the result of connecting SiPMs in series. Chapter 4 explains the experimental setups used to measure various characteristics of the SiPMs being considered for use in nEXO. and what their results say about the feasability of connecting SiPMs in series. Appendix A includes the DC analysis results of both individual and series SiPM behavior. Appendix B demonstrates the MATLAB code used to analyze the pulsed light results. Appendix C includes the pulsed light histograms and associated analyses from the MATLAB code.

Chapter 2

The Silicon Photomultiplier

2.1 Introduction

The Silicon Photo Multiplier (SiPM) is a photodetector that is finding use in a variety of fields, from medical imaging to beamline loss monitoring systems. The SiPM, or multi-pixel photon counter (MPPC) is a good choice for low-light sensing applications that require resolution down to the individual photon level. SiPMs consist of multiple avalanche photodiodes (APDs) that are held in a reverse bias voltage, usually within a few volts over the breakdown voltage for the given diode, V_{BR}. The diodes are constructed in such a way where incident photons within a certain frequency range have a probabilistic chance of creating an electron-hole pair. The charge carriers are acted upon by the high reverse bias electric field and move through the diode, inducing a current avalanche in the pixel. The current avalanche is self-sustained and quenched by the circuitry of the array. With a fixed bias voltage in the operating region, a single photon event on an APD will output a current pulse of constant charge. The output signal from the total SiPM is the superposition of all the individual APD pixel outputs. In this sense, the overall output can be modeled as the sum of binary signals from individual detected photons, which yields the total number of photons incident to the SiPM. However, multiple photons incident on the same pixel will produce the same signal as a single photon.

2.2 Physics Background

2.2.1 Single Photon Avalanche Diode (APD)Physics

At the core of an APD, as with any diode, is a pn-junction. While the specifics of the pn-junction can vary depending on the intended use of the APD, it will be reverse biased, which increases the size of the depletion region in the junction. One such APD pn-junction is shown in Figure 2.1.

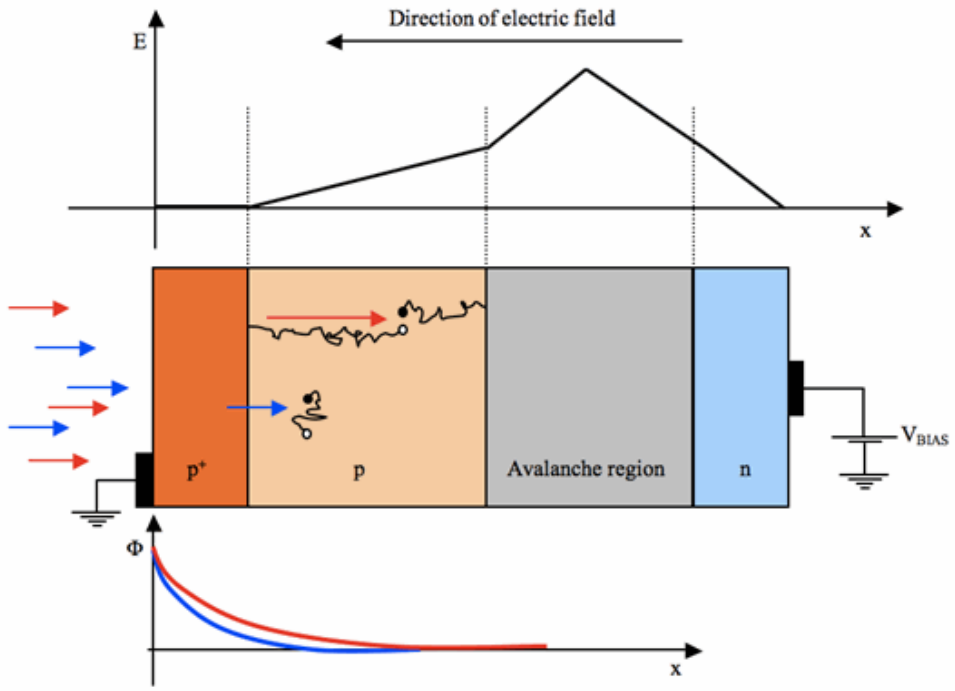

Figure 2.1: Typical SPAD pn-junction (Piatek, 2014b)

In this case, light is incident on the p+ side of the diode. As light travels through the diode, it has a probabalistic chance of being absorbed by the semiconductor and creating an electron-hole pair, depending on the energy of the photon. As can be seen in Figure 2.1, higher energy photons (shown in blue) tend to be absorbed closer to the incident surface than lower energy photons. The total flux of the incident light decreases exponentially through the diode.

When the electron-hole pair is created in the absence of any significant electric field, generally they recombine. However, if the electric field (which depends on the bias voltage) is high enough at the incident area, the electron and hole will be seperated into the two constituent charged particles by the electric field and move in opposite directions. While passing through the depletion region (or "avalanche region" in Figure 2.1), there are very few mobile charge carriers and recombination is unlikely. Eventually the electron and hole will be collected at their respective electrodes.

By controlling the doping and pn-junction properties of the APD, one can create a diode that is sensistive to specific frequencies of light. Through various phenomena, frequencies of light that are too high will not result in electron-hole pairs that can be moved by the electric field. Frequencies of light that are too low will pass through the diode without creating an electron-hole pair. Figure 2.2 shows the mean length that photons of various frequencies travel before being absorbed in Silicon.

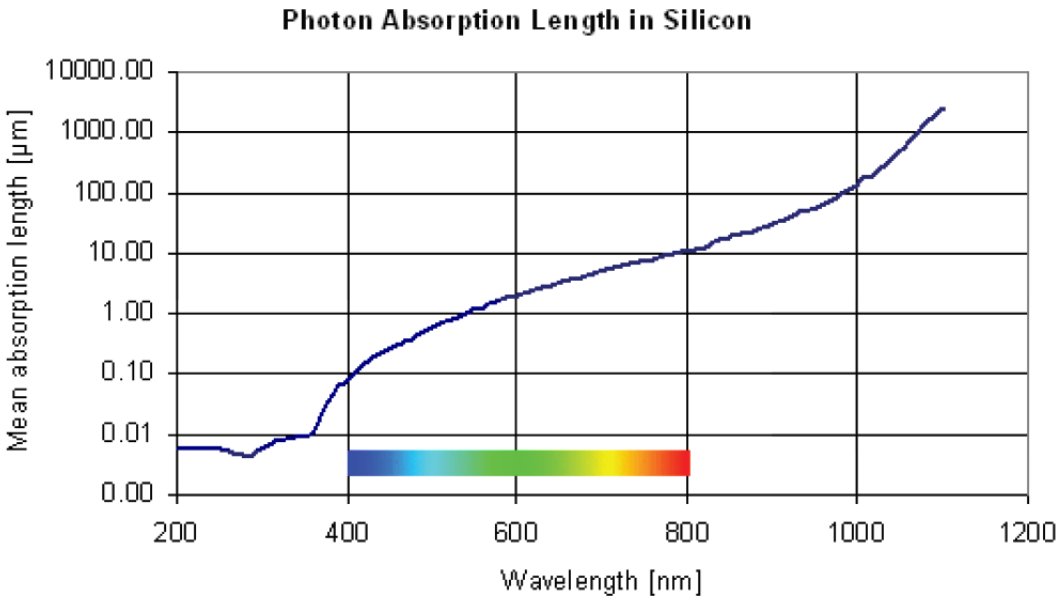

Figure 2.2: Mean absorption length in silicon (*An Introduction to the Silicon Photomultiplier*)

2.2.2 APD Gain

One electron of charge is not enough for single photon detection. In order to provide clear and unambiguous data that a photon has initiated an electron-hole pair, that one electron-hole pair must create significant current that can be measured at the APD's electrodes. The mechanism for this is impact ionization. As the strength of the electric field (which is proportional to the bias voltage) increases, the electron or hole gains enough energy between successive collisions to ionize an atom in the semiconductor lattice. This ionization produces a new electron and hole, which can then again be moved by the electric field, and may result in further impact ionization of other atoms.

Gain, M, is defined in Equation 2.1 as the charge (Q) that is created by one incident photon's initial charge (e).

$$M = \frac{Q}{e} \tag{2.1}$$

The device gain is a function of biasing voltage as illustrated in Figure 2.3. This figure shows three main regions of operation. In the first, the gain is unity as impact ionization is negligible due to the low electric field.

In the second region, the gain is much larger than unity due to the higher electric field, which increases the kinetic energy of the primary charges created from the absorption of a photon. The higher kinetic energy generates secondary charges due impact ionization. The rate of impact ionization depends on α and β, which are the rate coefficients of impact

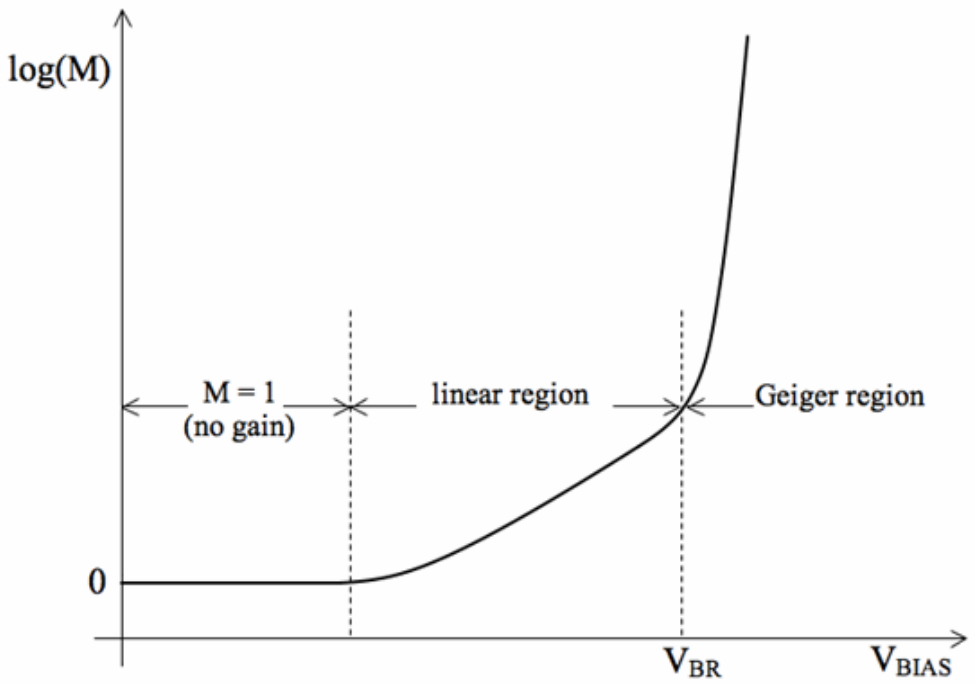

Figure 2.3: Typical SiPM gain relationship to voltage (Piatek, 2014b)

ionization events per unit length in a semiconductor for electrons and holes, respectively. Figure 2.4 shows these coefficients for various semiconductor materials.

In this region of operation for a given SiPM, one incident photon will result in many electrons and holes that are collected at the electrodes, generally on the order of 100 to 1,000. Eventually, the flow of electrons and holes will cease, as the electric field does not provide enough potential to the diode to sustain this charge flow. The linear gain region in Figure 2.3 ends at the breakdown voltage V_{BR}, and the Geiger region begins.

In the third region of operation, the Geiger region, impact ionization is self-perpetuating once it is initiated, as the electric field gives enough energy to the charge carriers to continually induce electron-hole pairs. As shown in Figure 2.4, α and β tend to converge with a higher electric field. In the Geiger region, $\alpha \approx \beta$, and the rate of impact ionization matches the rate at which electrons and holes are collected at the electrodes. This is called a "current avalanche". The Geiger region provides high gain, on the order of $10^5 - 10^6$, although this creates a continuous current that must be "quenched" to be measured as a discrete event.

2.2.3 Output Signal

In order to to separate detection of single photon events it is necessary to quench the gain by reducing the reverse bias voltage below the breakdown voltage of the device, thereby preventing detection of subsequent photon events until the first event has been detected by the data acquisition electronics. Post detection, the reverse bias voltage is increased, ready for the next photon event. One simple method of quenching that using a single bias

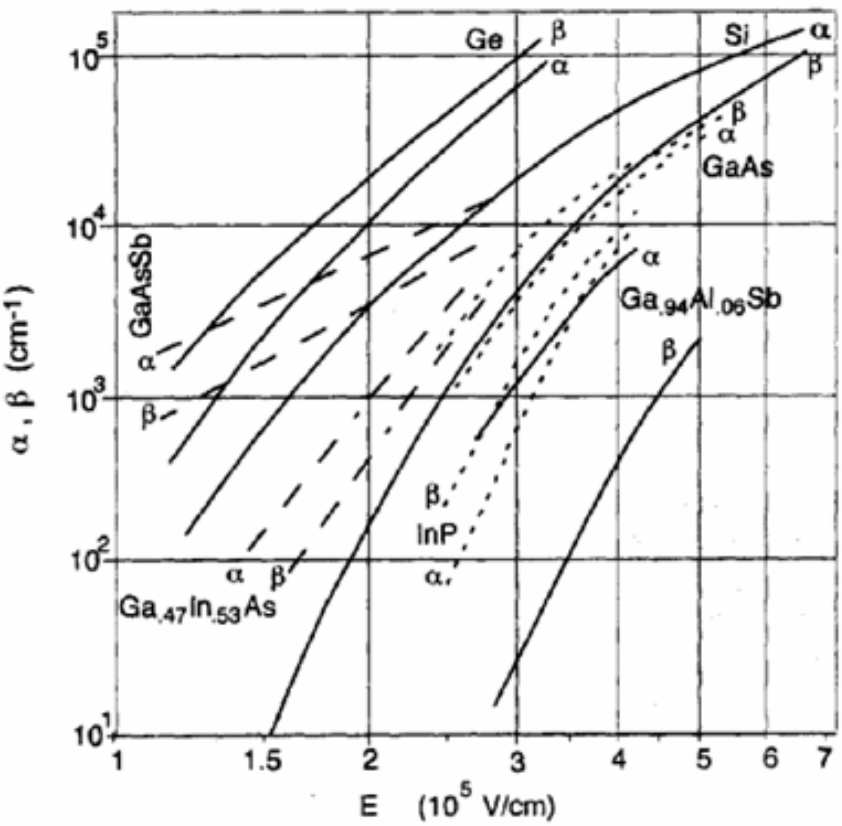

Figure 2.4: α and β Impact ionization coefficients for various semiconductor materials (Piatek, 2014b)

resistor, referred to as passive quenching, is illustrated in Figure 2.5. An APD with quenching circuitry is generally referred to as a single photon avalanche detector (SPAD).

In Figure 2.5, the components inside the dotted lines are inherent to the SPAD. The capacitor C_J represents the junction capacitance in all diodes with a depletion region. Resistor R_S is the series resistance of the undepleted regions of the diode. Resistor R_J (not shown) is the resistance of the depletion region, which is generally negligable when current begins to flow. The resistor R_Q is the quenching resistor external to the SPAD cell, and V_{BIAS} is the external bias voltage applied to the cell. The switch S is not a physical component of the SPAD, but represents an available current path. A fully ready Gieger mode cell has its C_J fully charged and S open, not allowing current flow. The voltage across the SPAD, V_D, is equal to V_{BIAS}.

When an electron-hole pair is created in Geiger mode and begins a current avalanche, the equivalent action on the schematic is the switch S closing. This closing switch creates a current path. Current will flow, discharging the capacitor with the time constant $\tau_{discharge} \approx C_J R_S$. The current will increase according to Equation 2.2.

$$i = i_{MAX}(1 - e^{\frac{-t}{C_J R_S}}) \tag{2.2}$$

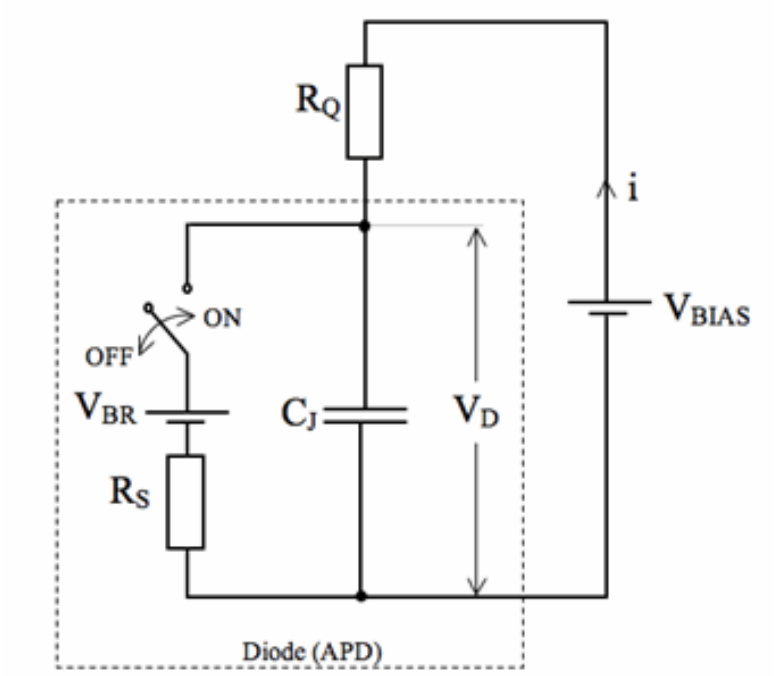

Figure 2.5: Equivalent electrical schematic of a Geiger mode SPAD (Piatek, 2014b)

This current is, by necessity of the series connection, flowing through R_Q. As the current increases, the voltage drop across R_Q increases as well. Eventually, since V_{BIAS} is fixed, this means that V_D will decrease due to the increasing voltage drop across R_Q. Once V_D drops beneath the breakdown voltage of the SPAD, the cell is no longer in the Gieger region, and S opens, closing off that current path. The current at which this happens is described in Equation 2.3.

$$i_{MAX} = \frac{V_{BIAS} - V_{BR}}{R_Q + R_S} \tag{2.3}$$

Immediately, current will stop flowing through R_S, however current will still flow through R_Q to charge C_J. This charging will happen with the time constant $\tau_{recharge} \approx C_J R_Q$. The current will decrease according to Equation 2.4.

$$i = i_{MAX}(e^{\frac{-t}{C_J R_Q}}) \tag{2.4}$$

Eventually C_J will be charged and the current will cease, bringing the SPAD to the initial condition. The entire process outputs a current pulse of the type shown in Figure 2.6.

Since $R_S \ll R_Q$, the initial exponential rise time is much quicker than the fall time. This results in the asymmetrical current pulse shown. A SPAD should ouput the same current pulse every time an avalanche is initiated. It then follows that Q in Equation 2.1 is found

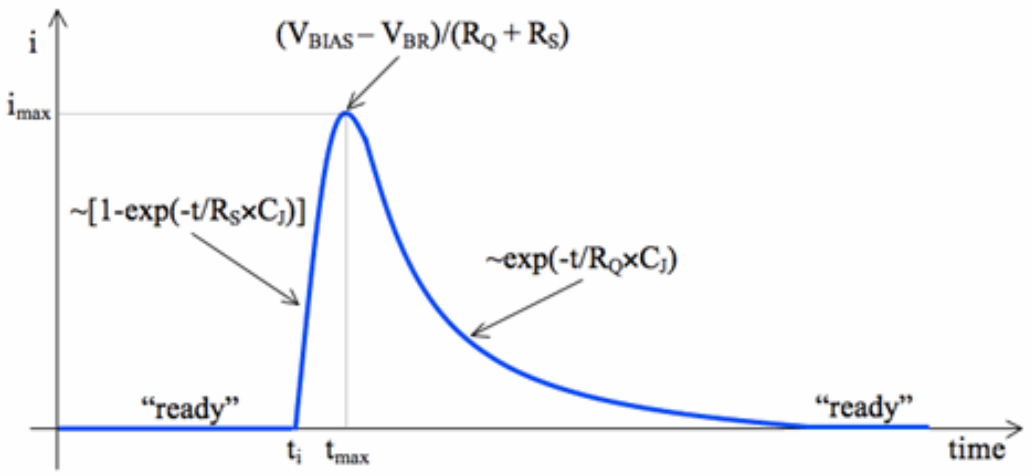

Figure 2.6: Typical current pulse output of an SiPM (Piatek, 2014b)

by integrating the entire current pulse as in Equation 2.5.

$$Q = \int idt \tag{2.5}$$

This total charge is what is stored in C_J. According to Equation 2.3, $V_{BIAS} > V_{BR}$ is required for significant current charge, or else there will be little to no current before V_D drops and ends the flow. The different between V_D (which should be equal to V_{BIAS} for a fully charged cell) and V_{BR} is a crucial property in analysis of SPADs, and results in the overvoltage, V_{OV}, shown below in Equation 2.6.

$$V_{OV} = V_D - V_{BR} \tag{2.6}$$

In the electrical model of a fully charged SPAD biased in Geiger mode, the voltage above V_{BR} applied across C_J is defined as the overvoltage V_{OV}, which gives an expression for the charge stored in C_J:

$$Q = C_J V_{OV} \tag{2.7}$$

Which, substituted for Q in Equation 2.1 leads to:

$$M = \frac{C_J V_{OV}}{e} \tag{2.8}$$

It should be noted that in the absence of a quenching resistor, there is a maximum, self-sustaining current that will flow once a Geiger-mode SPAD avalanche is initiated, sometimes called the latch current, or I_{LATCH}. This is the maximum current that the pixel can

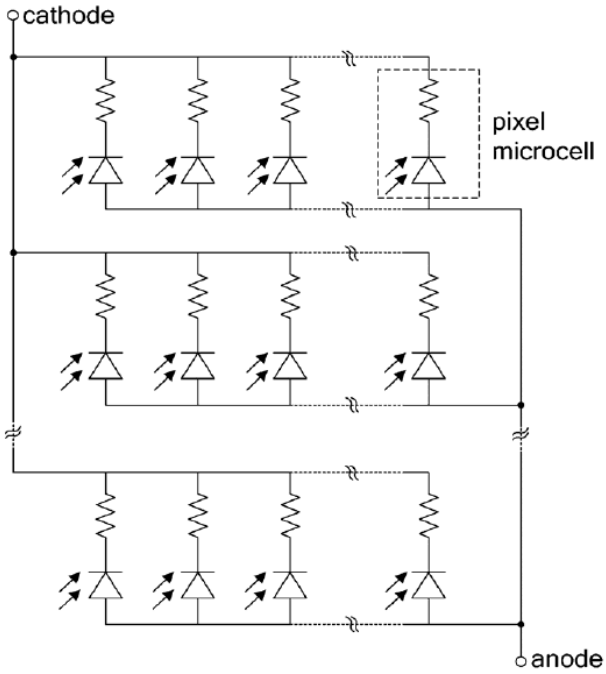

Figure 2.7: Simplified concept of an APD array in parallel (Marano et al., 2014)

physically output. In order to be able to quench the avalanche, $R_Q I_{LATCH} > V_{OV}$. This makes intuitive sense, as the voltage drop across the quenching resistor must at least reduce the voltage across the cell to be below V_{BR} in order to quell the avalanche.

The above analysis provides some guidance as to proper sizing of R_Q for a given V_{OV}, and predicts the behavior if R_Q is too low. If $R_Q I_{LATCH} \approx V_{OV}$, then the current output will remain at I_{LATCH} for some time before statistical fluctuations end the avalanche. If $R_Q I_{LATCH} < V_{OV}$, the SPAD will not quench, and after an avalanche it will continuously output a current of I_{LATCH}. This analysis also provides guidance on biasing SPADs if the R_Q is constant. Although increasing V_{OV} will increase the gain of the SPAD, once it is too large, as shown in the expression above, the SPAD will only output a constant current, not a useful pulse, and the SPAD is said to be in the "instability region."

2.2.4 Silicon Photomultipliers (SiPMs)

As the area that a single SPAD is sensitive to is generally on the order of μm^2, to truly characterize the incident light flux for a larger area, multiple SPADs are required for the measurement. SPADs are often connected in parallel to form an array, seen below in Figure 2.7.

Recent advances in semiconductor processing technologies have enabled manufacturing of many SPADs, on the order of 10^5 cells on a single unit, generally called an SiPM. Manufacturing multiple SPADs on a single substrate is a crucial factor in allowing SiPMs to be effective single photon detectors over a larger surface area. The figure of merit for this

configuration is the Fill Factor, F_G, defined in Equation 2.9, where A_E is the total photo-sensitive area of the SiPM, and A_T is the total geometrical area that the unit occupies. A high F_G is important for efficiency of the sensor, especially for the nEXO application.

$$F_G = \frac{A_E}{A_T} \tag{2.9}$$

Keeping in mind that the anode is biased negatively, the SiPM array in Figure 2.7 allows all SPADs to be biased to the same gain, as described in Equation 2.8, assuming that each pixel is manufactured with identical values of C_J and V_{BR}. When one cell fires, the seperate quenching resistors allow individual pixels to act as current sources and be quenched without affecting the biasing of any other inactive cells. Of particular interest is the response of the structure to two simultaneous photon absorption events. If the two photon are absorbed on a single cell, the two-photon event will be registered as a single event. However, if two (or more) photons are absorbed in different cells then each branch of the SiPM will generate a current pulse. According to Kirchoff's Current Law, the total current generated will be a summation of independently firing cells N_F, as given in Equation 2.10.

If the output current pulse is amplified by a current amplifier, then the composite current pulse for one, two, three, and four simultaneous photon detection events is illustrated in Figure 2.8.

$$Q_{OUT} = N_F C_J V_{OV} \tag{2.10}$$

In Figure 2.8, it can be seen that as long as all photons of an event arrive simultaneously, each additional firing cell will add its charge to the total current pulse. "1 p.e." designates a one photon event, where one pixel fires. "2 p.e." designates a two photon event, where two pixels simultaneously fired, leading to an output where the current pulse is double that of a 1 p.e. at every point. As each p.e. is quantized, by analyzing the value of the peak, one can come to a conclusion as to how many cells fired for a given event.

For many applications, the total number of incident photons is often required to fully quantify light flux arriving at the detector. Non-ideal behavior of practical SiPMs is accounted by defining a figure of merit called the Photon Detection Efficiency (PDE) , which is defined as a ratio of photo-electrons generated to the incident number of photons. PDE, defined in Equation 2.11, defines the probability of detecting a single photon.

$$PDE = F_G \; \eta(\lambda) \; P_A \tag{2.11}$$

F_G is the probability that a photon strikes a sensitive part of the array, P_A is the probability that an electron-hole pair will trigger an avalanche, and $\eta(\lambda)$ is the quantum efficiency of photon detection at the given wavelength, defined in Equation 2.12, where η_λ is the number of incident photons for a given wavelength and η_{e-h} is the number of those

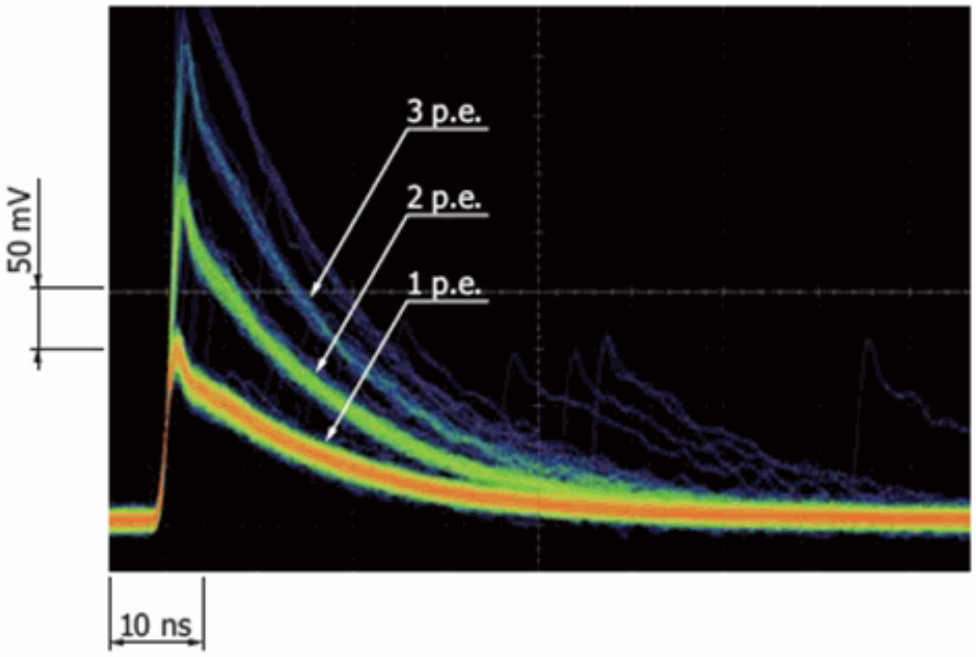

Figure 2.8: Resulting signal from multiple SiPM pixels firing in a parallel array (Piatek, 2014b)

photons that create an electron-hole pair. It can be thought of as the probability that an incident photon will produce an electron-hole pair.

$$\eta(\lambda) = \frac{\eta_{e-h}}{\eta_{\lambda}} \tag{2.12}$$

$\eta(\lambda)$ and P_A are both dependant on wavelength, while P_A is also dependent on V_{OV}, as the electric field is critical in inducing impact ionization. Thus, knowledge of the PDE enables the experimenter to determine the incident photon flux. Of course, a high value of PDE is always desirable at the operating wavelength. In general, due to the quantum model, the PDE is described by random process, leading to quantum noise as discussed below.

2.3 SiPM Noise

When measuring SiPMs in practice, an experimenter will inevitably see noise in any measurement taken. The noise inherent to an SiPM can limit the resolution and ability to count to the single photon level. Careful consideration of the causes of noise must be taken into account to design an experiment that efficiently utilizes SiPMs.

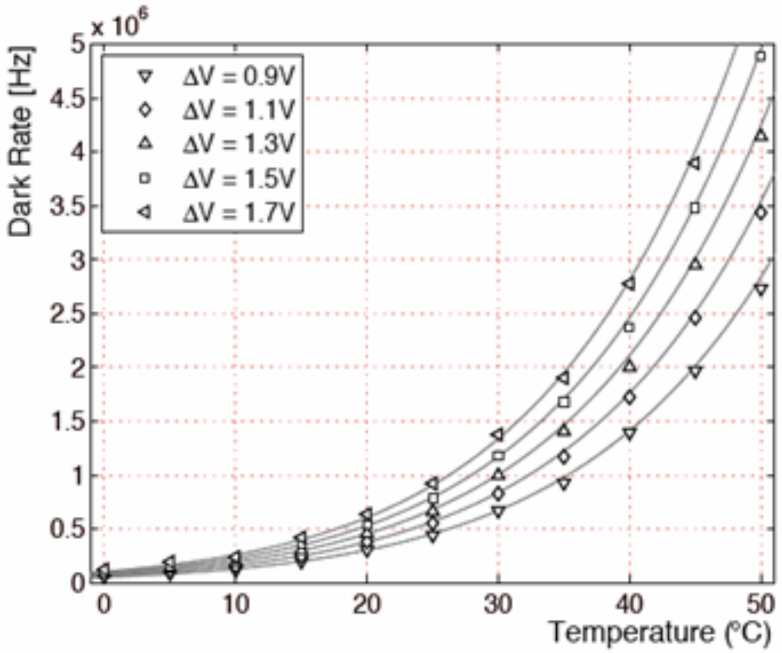

Figure 2.9: Hamamatsu S10362-11-050C dark count rates (Piatek, 2014b)

2.3.1 Dark Noise

Dark noise is mainly caused by thermally generated electron-hole pairs in the semiconductor. There is a non-negligable probability of an electron moving from the valence band to the conduction band of a semiconductor due to energy from the temperature of the device. When this happens, the electron is indistinguishable from one generated by a photon. It may very well recombine, although if the free electron is close enough to the depletion region, it may be siezed by the electric field and induce an avalanche. If this happens, the avalanche current pulse will be identical to that of a one photon event of the SiPM. In an SiPM, dark noise will constantly be occuring in seperate cells with no correlation to each other, resulting in randomly occuring 1 p.e. current peaks. Typical dark rate values for a Hamamatsu S10362-11-050C in a variety of temperature and V_{OV} conditions are shown in Figure 2.9.

Dark noise is generally measured in terms of the frequency of 1 p.e. peaks when there is no light incident on the device. For a one square millimeter SiPM at room temperature, the dark count rate will typically be $10^5 - 10^6 Hz$. Since the occurence of dark noise is heavily dependent on temperature, lowering the operating temperature of the device can drastically reduce the dark count rate. Dark noise is also proportional to the pixel size of the device, as a larger area increases the probability of thermally generated electron-hole pairs. Lastly, the dark count rate depends also on V_{OV}, as a larger overvoltage leads to a stronger electric field, making it more probable that the electron-hole pairs are seized and generate an avalanche. A lesser factor in dark count - tunneling, also is proportional to V_{OV} (Collazuol, 2012).

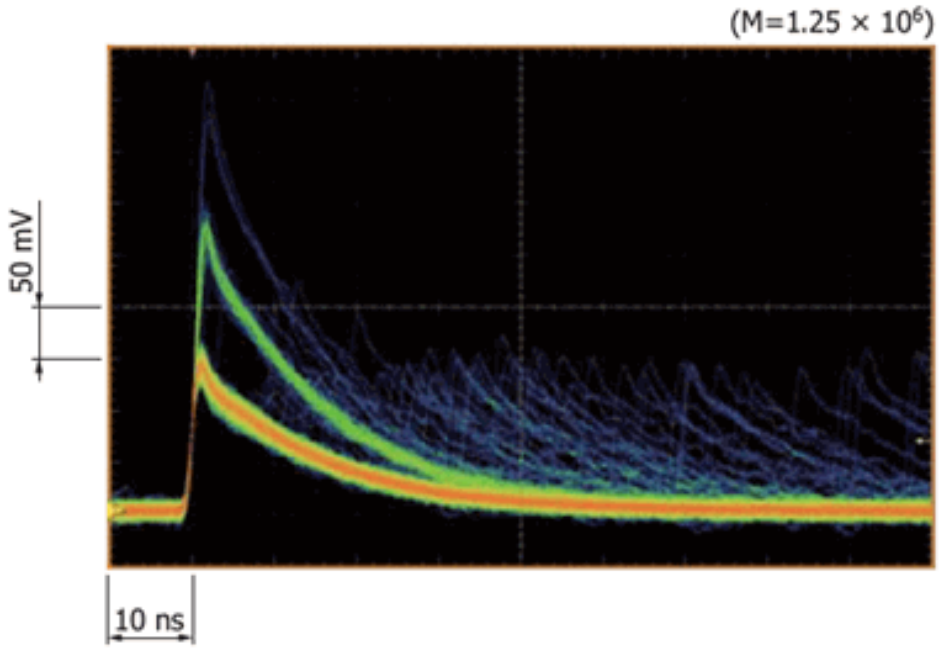

Figure 2.10: Overlay of afterpulses (Piatek, 2014b)

2.3.2 Afterpulsing

Afterpulsing is a phenomenon in which electrons are trapped in semiconductor lattice defects during an avalanche. Some time after the peak current, the electrons are dislodged from the trap and induce another current avalanche. This secondary current avalanche also releases a total charge as described in Equation 2.6. However, if the afterpulse occurs after the current peak of the primary avalanche, while the pixel is recovering and C_J is charging, the V_{OV} will be less than the difference between the external V_{BIAS} and the V_{BR}, resulting in a lower total charge Q being released. If the afterpulse occurs after the pixel is fully recovered and charged, the resulting avalanche will be identical to that of a one photon event. Overlays of both types of afterpulsing are seen in Figure 2.10.

Afterpulsing is a stochastic process, generally characterized by the probability that an avalanche will result in afterpulsing, as well as the time after the primary pulse that the afterpulsing occurs. The probability of afterpulsing increases with V_{OV}, as more charge carriers are released in the primary avalanche, as well as providing a higher electric field that is more likely to cause a trapped electron to induce an avalanche. This results in afterpulsing being less likely immediately after the current pulse peak since, as described above, V_{OV} is not at it's maximum during pixel recovery. This can be seen in Figure 2.10. While detailed studies of afterpulsing in SiPMs are still ongoing (Para, 2015), a summary of the probability of afterpulsing for three Hamamatsu SiPMs is shown in Figure 2.11. It should be noted that the difference between the three studied SiPMs are the pixel size, with the 100C being the largest with $100\mu m^2$ pixels and the 25C being the smallest with $25\mu m^2$ pixels.

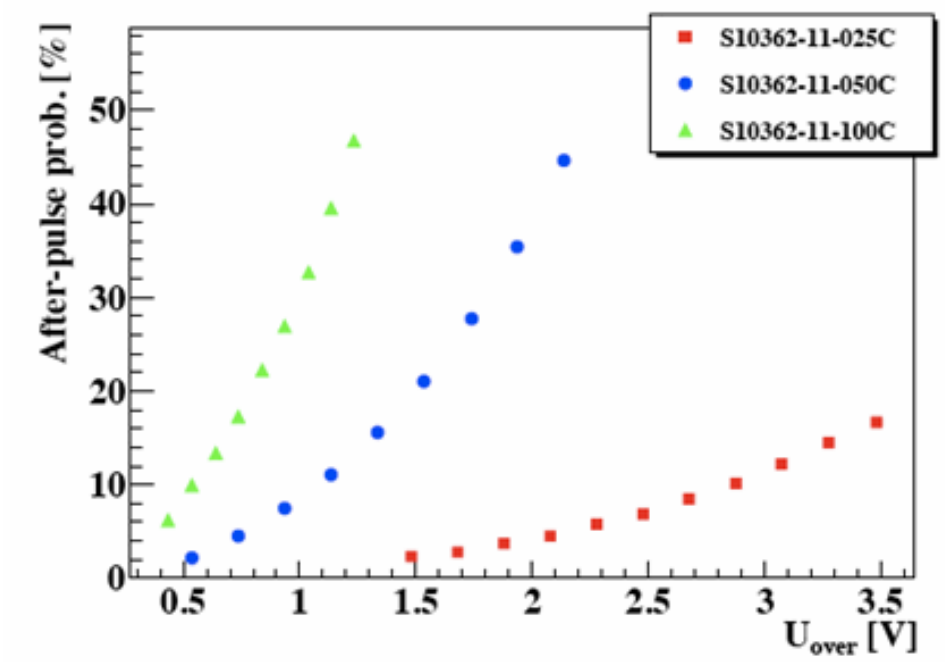

Figure 2.11: Probability of afterpulsing vs. overvoltage (Piatek, 2014b)

2.3.3 Crosstalk

Crosstalk is another source of SiPM noise caused by the emission of photons as charge carriers are moving through the depletion region during a current avalanche. The mechanisms of photon emission are due to semiconductor phenomena such as indirect and direct interband recombination, and Bremsstrahlung radiation (Piatek, 2014b). When these photons are emitted, they may travel to an adjacent SiPM pixel. In depth studies have shown that these photons can be directly captured in the second pixel, producing an electron-hole pair, or may possibly induce charges from a distance that can migrate to the depletion region and be seized by the electric field. Both of these scenarios are shown in Figure 2.12.

In either case, an avalanche may be induced in the same way that one is initiated from the signal light. The probability of the avalanche is then dependent on the wavelength spectrum of the released photons. Generally, an avalanche of 10^6 charge carriers in silicon results in around 30 photons with an energy high enough to create an avalanche in neighboring cells. Since the travel time of a photon to an adjacent pixel is negligeable compared to the recovery time of the primary pixel, if crosstalk does occur, the SiPM will output a 2 p.e. pulse, as crosstalk will appear to happen instantaneously. Crosstalk is found to depend mostly on gain, as more charge carriers during an avalanche leads to more emitted photons with a high enough energy to induce crosstalk. The relative crosstalk probabilities for select SiPMs are shown below in Figure 2.13.

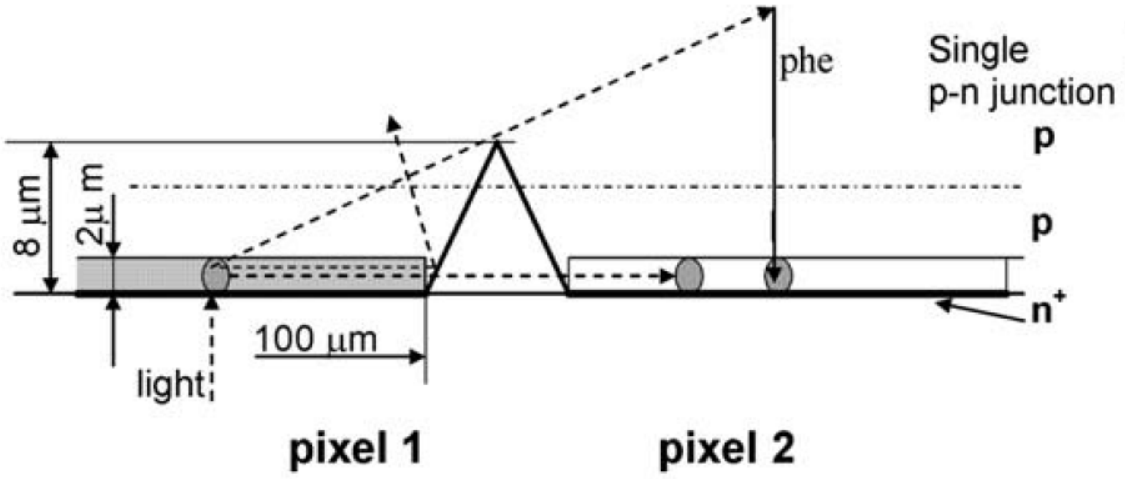

Figure 2.12: Visual diagram of the occurence of crosstalk (Buzhan et al., 2009)

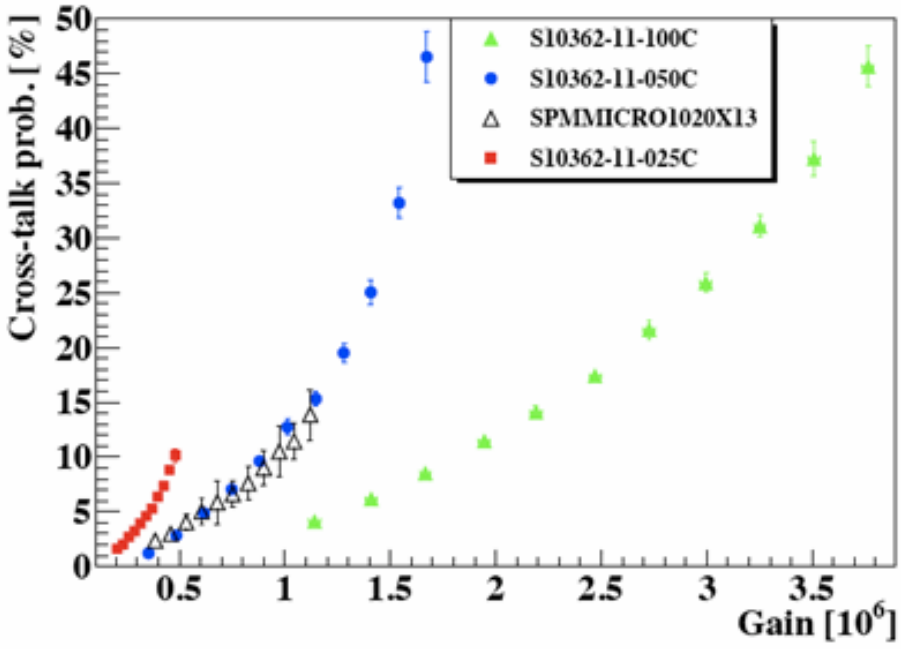

Figure 2.13: Probability of crosstalk vs. gain (Piatek, 2014b)

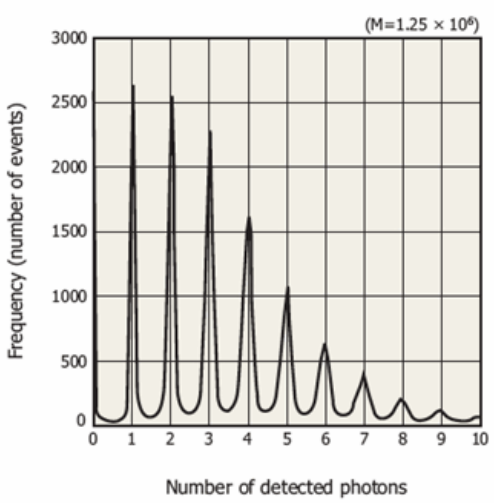

Figure 2.14: Generic histogram output for an SiPM (Piatek, 2014b)

2.4 Amplification and Measurement

2.4.1 Output Signal

The typical pulse output from an SiPM has a maximum current value in the μA range. This requires an amplifier to be used to amplify the current pulse into a voltage pulse that can analyzed by readout electronics. When an ideal current amplifier is used to amplify an SiPM current pulse, its output will be a voltage pulse of the same shape of the current pulse, the values of which are determined by the gain of the amplifier. The gain of a charge amplifier is measured as in Equation 2.13, as Volts per Coloumb.

$$G = \frac{V_{OUT}}{Q} \tag{2.13}$$

When analyzing results from SiPMs, generally the pulse heights measured from the amplifier are arranged in a histogram, as seen in Figure 2.14. The X-axis in Figure 2.14 is some measure of the total charge of the event, interpreted as the probability of a discrete number of photons that must have triggered the avalanche, and the Y-axis is the total amount of occurences of that bin.

Adapting the typical sensor output in Figure 2.6 to its amplified output, the voltage peak for an N photon event should be $NV_{1p.e.}$, where $V_{1p.e.}$ is the voltage peak of a one photon event. If the peak of each voltage pulse output from the amplifier is sampled and recorded, a histogram of the type in Figure 2.14 would result, with voltage on the X-axis. After many events, the repeated voltage peaks for N photon events will be the ones that occur the most, giving the characteristic peaks seen. It should be noted that for a constant flux pulse of light, there will still be variations in whether the identical light pulse results

in, say, a 1 p.e. or 2 p.e. output, since the mechanism behind the creation of electron-hole pairs is probabalistic.

Ideally, if each photon event is perfectly reproducible, there would be no width to the peaks. However, with the SiPM noise described in Section 2.3, as well as electronic noise, there will be some variance to the repeatability of the readings, leading to the width of the peaks. For single photon resolution, the variance of the peaks must be kept as low as possible, through mitigation of sensor and electronic noise. If the peak widths bleed into each other, it becomes difficult to determine exactly how many photons the SiPM has sensed. The resolution and FWHM of an individual peak is analyzed as a Gaussian, while the distribution of all photon event peaks is Poissonian.

2.4.2 SiPM Capacitance

The capacitance of an SiPM is crucial when considering the output pulse noise. As previously mentioned, the typical junction capacitance of a single SPAD cell, which is the dominant capacitance, is typically around 30 fF. If the SiPM consists of an array of 30,000 cells in parallel, this gives a total array capacitance of 0.9 nF, which is on the order of the capacitance typically measured from an SiPM.

An analysis of amplifier noise will show that due to the origin of noise sources, the input capacitance C_{IN}, the sum of the sensor capacitance and input transistor capacitance, is critical. The series noise component of the total noise variance is proportional to C_{IN}. This means that reducing the load capacitance will increase the signal to noise ratio of the amplifier output. Given the properties of adding capacitors in series vs. parallel, it can be seen why the subject of connecting SiPMs in series is attractive in large scale arrays. Connecting N SiPMs in parallel and amplifying their sum leads to N times the load capacitance, while connecting those same N SiPMs in series will give a load capacitance of $\frac{1}{N}$, lowering the noise variance rather than raising it. An investigation on the signal to noise consequences of the series connection will be shown when discussing the results from the simulation.

Chapter 3

Modeling the Series Connection

3.1 Introduction

One of the goals during R&D of the nEXO experiment is to explore the feasibility of alternative light measurement schemes to the standard one of connecting SiPMs in parallel. As mentioned in Section 2.2.3, the parallel connection of multiple arrays has inherent advantages. A fixed external voltage source can ensure that each array is biased at the same voltage as the others, and multiple input signals neatly sum at the output, producing good resolution for repeat events. However, research has been undertaken into the series connection to try to take advantage of reduced input capacitance of the series array, which lowers noise seen at the charge amplifier, as well as provide a more convenient configuration for the logistics of connecting the pixels in a $4m^2$ array.

3.2 The SiPM Model

As a starting point, the SiPM electrical model brought forward by Corsi et al., 2006, is considered, shown in Figure 3.1. This model consists of N pixels in the SiPM. One of them, the one enclosed in the dotted area on the left, is firing. The other $N-1$ non firing microcells are identical and connected in parallel to each other, shown in the dotted area in the middle. The dotted section on the far right includes the parasitic capacitance C_g from the anode to the cathode of an SiPM array. This is due to the metal grid that connects all SiPM pixels to the bias contact, seen in Figure 3.2, but also includes other fringe capacitances. Generally, C_g is proportional to the area of the SiPM, and has a typical value of about $0.03\frac{fF}{\mu m^2}$, which, for an SiPM of, say, $1mm^2$, gives a C_g of $30pF$.

The functionality of this model is similar to that of the one shown in Figure 2.5. Some additional factors are considered. The switch and R_S are replaced by a Dirac current generator that contains the entire charge pulse generated from an incident photon event as

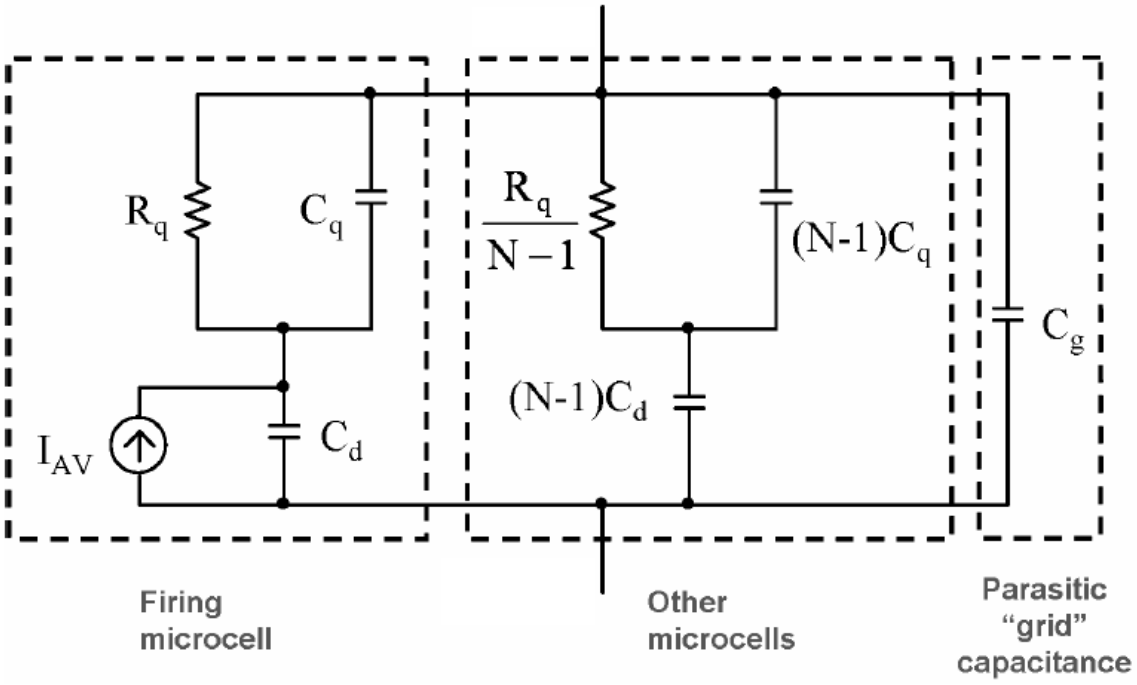

Figure 3.1: Corsi electrical model for a SiPM with one cell firing (Corsi et al., 2006)

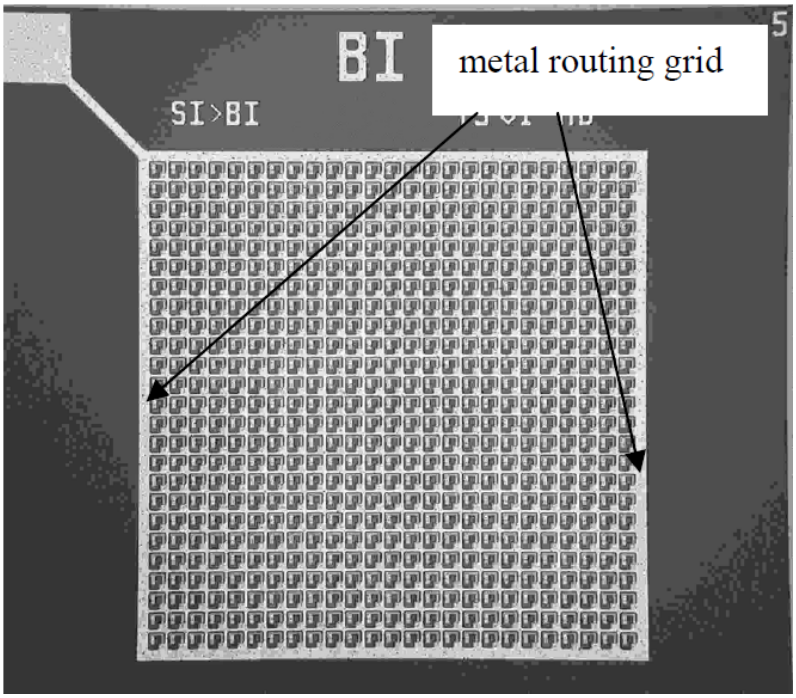

Figure 3.2: Origin of C_G for SiPMs (Corsi et al., 2006)

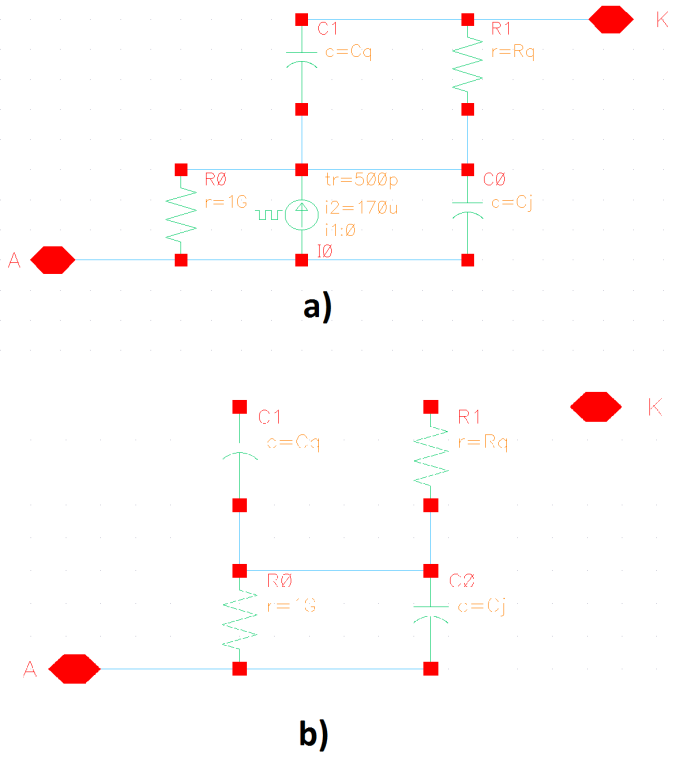

Figure 3.3: Simulation model of single firing cell

described in Equation 2.7. Also, the parasitic capacitance of the quenching resistor, C_q is included. C_d represents the junction capacitance.

Computer models are created for analysis in Cadence Virtuoso based on the Corsi model. A 1 $G\Omega$ resistor is added in parallel to the junction in order to provide a DC path for the leakage current of the pixel. Figure 3.3a shows the circuit equivalent model fo an active firing pixel as used in the simulation and the circuit model for the inactive pixel is shown in Figure 3.3b.

One example of the SiPM array models used is in Figure 3.4. Each symbol is a representation of either the "Active" or "Inactive" cells seen in Figure 3.3. The array next to each symbol (1:n) describes how many of these cells are in parallel. The capacitor C_P represents the parasitic grid capacitance described above. The parameter A allows it to be scaled to simulate larger array sizes. R_{OUT} represents the input impedance of the charge amplifier.

The simulation is set to model the type of Hamamatsu SiPM that would later be physically tested. Typical values for all parameters were obtained from Hamamatsu, a manufacturer of SiPMs, and verified from testing. The values are summarized in Table 3.1.

Values for the current pulse characteristic are determined in order to emulate a Dirac pulse of an accurate magnitude. For example, with the trapezoidal current pulse generator

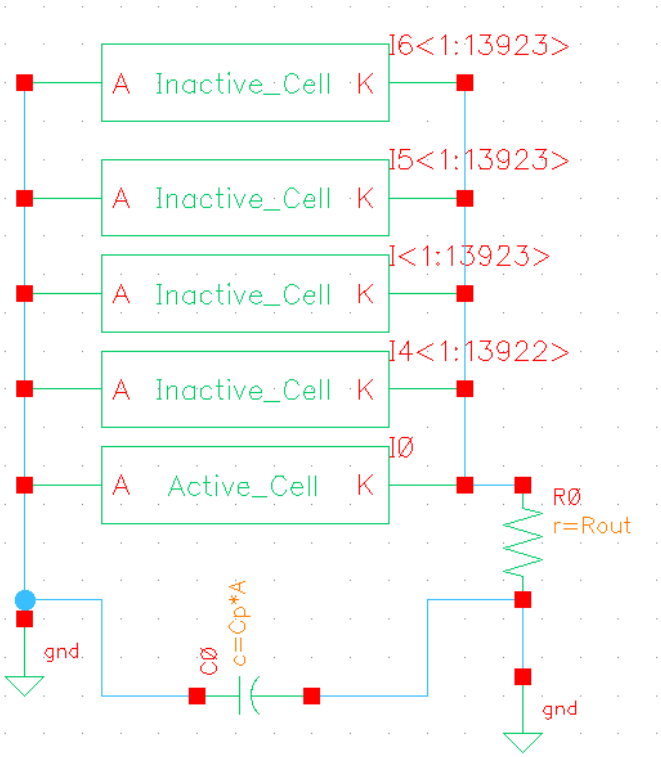

Figure 3.4: Simulation - Parallel configuration, 1 firing cell

Parameter	**Nominal Value**
A	$3mm$ x $3mm$
R_Q	$150k\Omega$
C_Q	$2fF$
C_P	$20pF * A$
C_J	$90fF$
R_{OUT}	50Ω
I_{PULSE}	$170\mu A$
I_{RISE}	$500ps$
$I_{DURATION}$	$100ps$
I_{FALL}	$1ns$

Table 3.1: Summary of simulation parameters

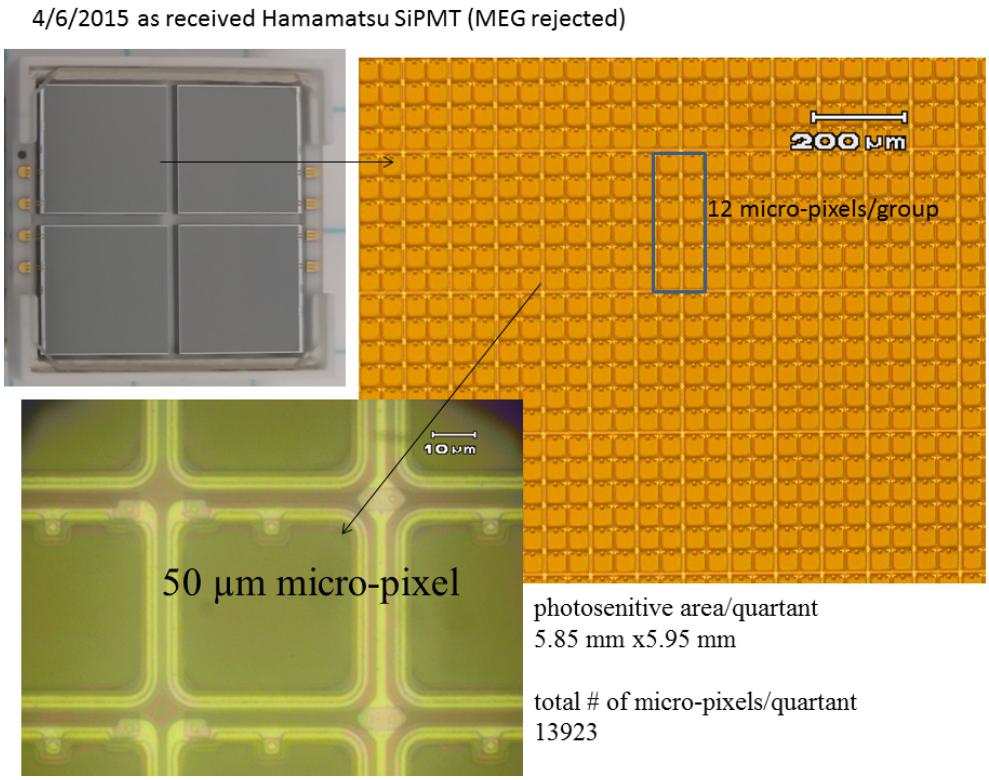

Figure 3.5: Receiving notes for Hamamatsu MEG SiPM unit

used in the computer model, the total charge is givin by

$$Q = 170\mu A(\frac{500ps}{2} + 100ps + \frac{1ns}{2}) = 145fC \tag{3.1}$$

By substituting into Equation 2.7, with the nominal value of C_J=90fF, it can be seen that this current pulse simulates the case of $V_{OV} = 1.6V$. R_Q, C_Q, C_G, and C_J are all properties relating to the design of the SiPM, which is outside of the control of the experimenter. With regards to the test setup, R_{OUT} can be controlled by the design of the amplifier used in the experiment. When R_{OUT} is included in the SiPM model, the voltage across R_{OUT}, the input to the amplifier, is given in Equation 3.2 (Corsi et al., 2006) where Q is the total charge, $\tau_{IN} = R_{OUT}(C_G + C_{EQ})$, $\tau_r = R_Q(C_J + C_Q)$, $\tau_q = R_Q C_Q$, and C_{EQ} is the equivalent capacitance of the N-1 C_J and N-1 C_Q of the unfiring cells. To study the complex effect of R_{OUT} on the output pulse, the circuit response is simulated for various values of R_{OUT}.

$$V_{IN}(t) \cong \frac{QR_{OUT}}{\tau_r - \tau_{IN}} \left(\frac{\tau_q - \tau_{IN}}{\tau_{IN}} exp\left(\frac{-t}{\tau_{IN}}\right) + \frac{\tau_r - \tau_q}{\tau_r} exp\left(\frac{-t}{\tau_r}\right) \right) \tag{3.2}$$

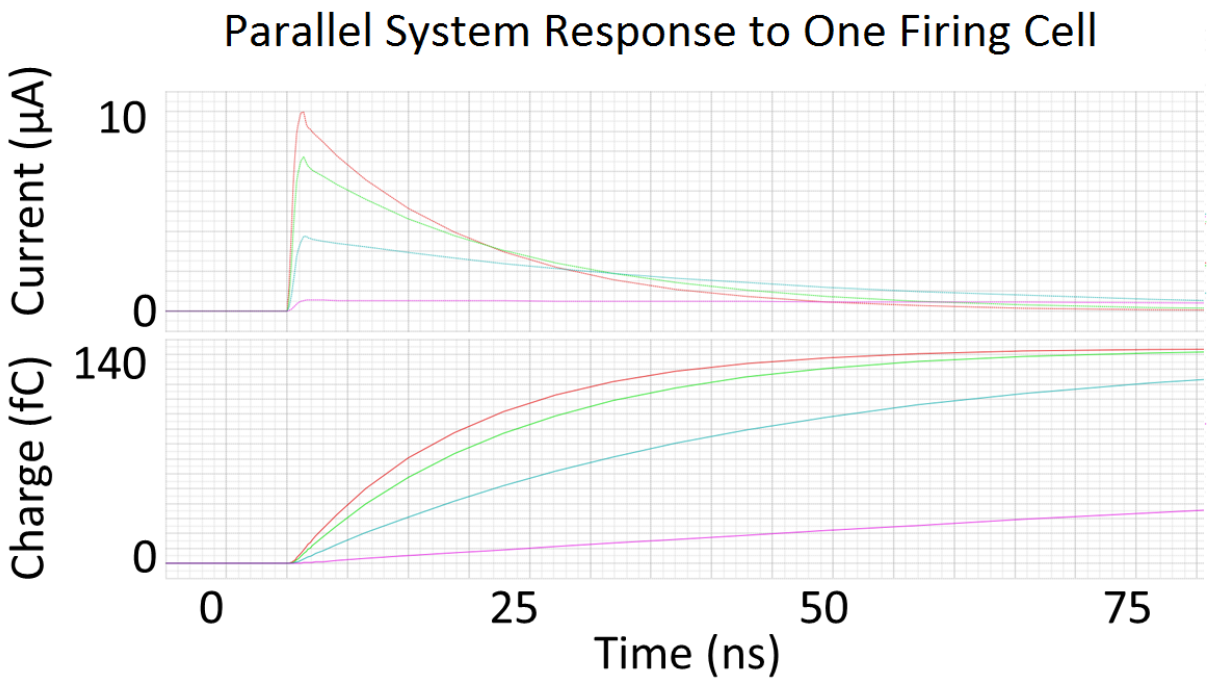

Figure 3.6: Simulation - Parallel configuration, 1 firing cell results
$R_{OUT} = 0.1\Omega$ $R_{OUT} = 1\Omega$ $R_{OUT} = 5\Omega$ $R_{OUT} = 50\Omega$

3.3 Simulation Results

Figure 3.5 shows images of a Hamamatsu SiPM which is used to obtain experimental data to validate the modelling and simulations described above. The unit included four "quadrants" that are each functionally an individual SiPM. To simulate a quadrant with a size of about 6 mm x 6 mm, 13,923 pixels are introduced into the model for each SiPM. The scale factor is set to 2, to increase the parasitic capacitance to the size of the pixel of this unit. To begin with, four SiPMs are connected in parallel with one sensor including one firing pixel, which is the standard, well studied operation of SiPMs. The model is shown in Figure 3.4, and the results are shown in Figure 3.6, where the top half of the plot is the output current across R_{OUT} and the bottom half is the total charge pulse at the output.

As can be seen, the pulse height and shape depends heavily on the input resistance to the amplifier. As suggested by Equation 3.2, a higher input resistance to the amplifier results in a lower maximum pulse height and a longer time for the full discharge to occur. However, in a realizable readout system, after amplification, the signal will be further shaped before sampling, and it is this shaping that will determine the shape of the measured pulse. As a benchmark, it is noted that the peak current for the lowest simulated input resistance, 0.1 Ω, is approximately 10 μA.

A second simulation in which the four quadrants are connected in series, and one pixel of one of the quadrants is firing is shown in Figure 3.7, and the results are shown in Figure 3.8. The maximum current at the benchmark input resistance is now 2.5μA, a division of four.

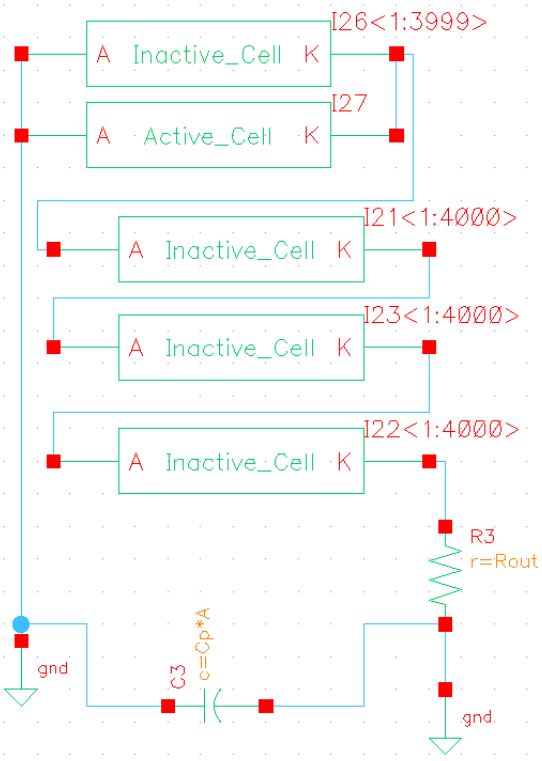

Figure 3.7: Simulation - series configuration, 1 firing cells

Additionally, the input resistance appears to have less of an effect on the pulse height and shape.

The adjusted pulse shape can be explained by Equation 3.2, as C_{EQ} is now reduced by four. This means that the denominator in the first term is larger, and a changing R_{OUT} has less effect. However, as mentioned above, after amplification, the readout chain determines the final pulse shape. The maximum current being divided by four is a consequence of the four series capacitors. Figure 3.9 illustrates an explanation of why this occurs. Figure 3.9a shows a simplified model of a firing SiPM in series with another one that is not firing. Figure 3.9b shows the same circuit with the firing SiPM transformed to its Thevenin equivalent circuit. In the Thevenin model, the two series capacitors combine to an equivalent capacitance of $\frac{C}{2}$. When transforming back into the equivalent Norton model, in Figure 3.9c, with the combined capacitors, the current source now has a value of:

$$\begin{aligned} I_{Norton} &= V_{Thevenin} * R_{Thevenin} \\ &= \frac{I}{j\omega C} * \frac{j\omega C}{2} \\ &= \frac{I}{2} \end{aligned}$$

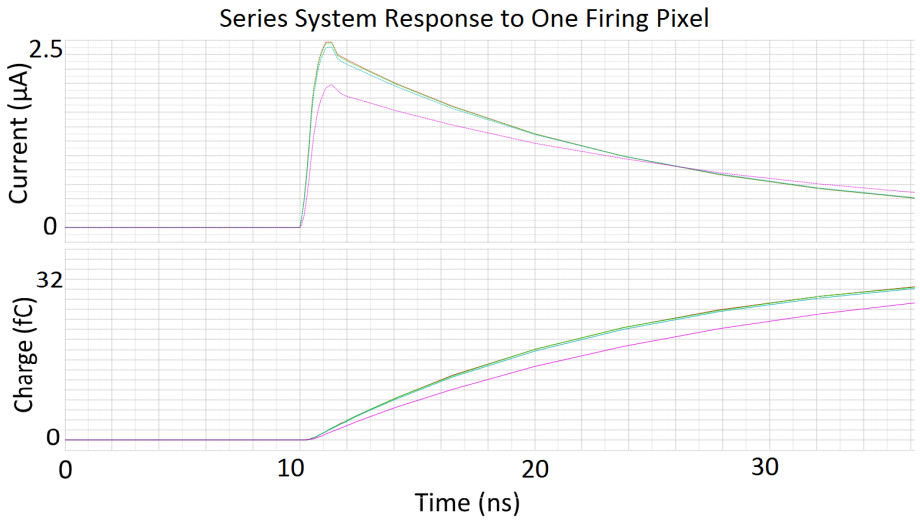

Figure 3.8: Simulation - Series configuration, 1 firing cell results
$R_{OUT} = 0.1\Omega$ $R_{OUT} = 1\Omega$ $R_{OUT} = 5\Omega$ $R_{OUT} = 50\Omega$

Therefore, as the equivalent capacitance of N series SiPMs is $\frac{C}{N}$, the total charge output will similarly result as $\frac{Q}{N}$.

3.4 Analysis

3.4.1 Noise Model

The sensor/amplifier system can be analyzed as the model in Figure 3.10, where $Q\delta(t)$ is the signal charge, C_D is the detector, or sensor, capacitance, C_{IN} is the total input capacitance of the amplifier, feedback capacitor, and any other parasitic capacitances. e_n and i_n are the series and parallel noise generators, with units of $\frac{V}{\sqrt{Hz}}$ and $\frac{A}{\sqrt{Hz}}$, respectively. When considering only white noise, the noise generators are equivalent representations derived from shot noise and thermal noise specific to the topology of the amplifier. A shaper is also used after the amplifier to limit the bandwidth to the frequency of interest to the signal, which impoves the noise response. The response of the system to an input of $Q\delta(t)$ is $v_\delta(t)$ and the variance of the output is v_n.

One form of representing a detector system's noise properties is by expressing it in Equivalent Noise Charge or ENC. The ENC of a system is the corresponding signal charge equivalent of the amplifier's output variance, or in other words, the signal magnitude required for a signal to noise ratio of 1. The lowest possible ENC is always desired for a given system. If the signal is filtered so that the output pulse has a maximum (or minimum, depending on polarity) at time t_p, and the response of the system is measured such that the signal value is taken at this maximum shaped value, the ENC can be expressed in rms electrons as in Equation 3.3 (De Geronimo, 2014), where A_S and A_P are shaping coefficients specific

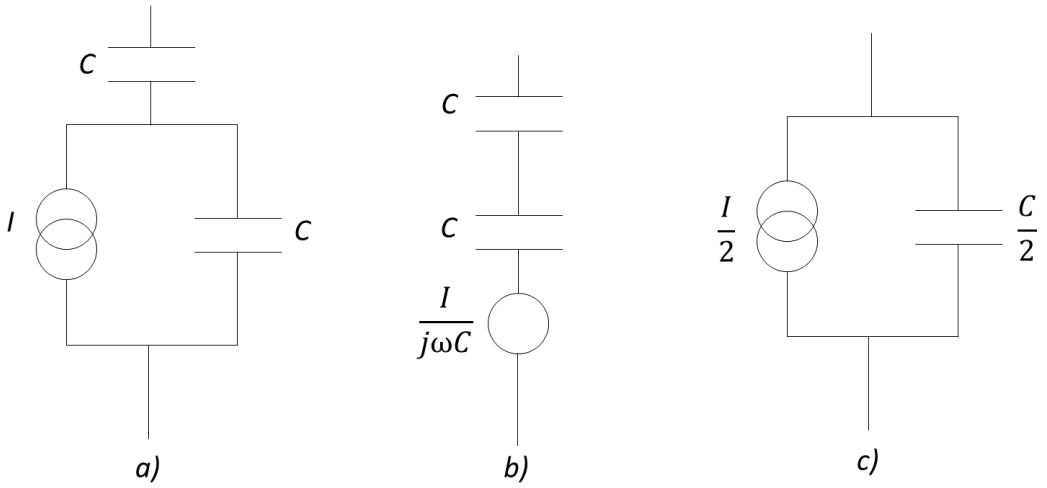

Figure 3.9: Reduced charge model

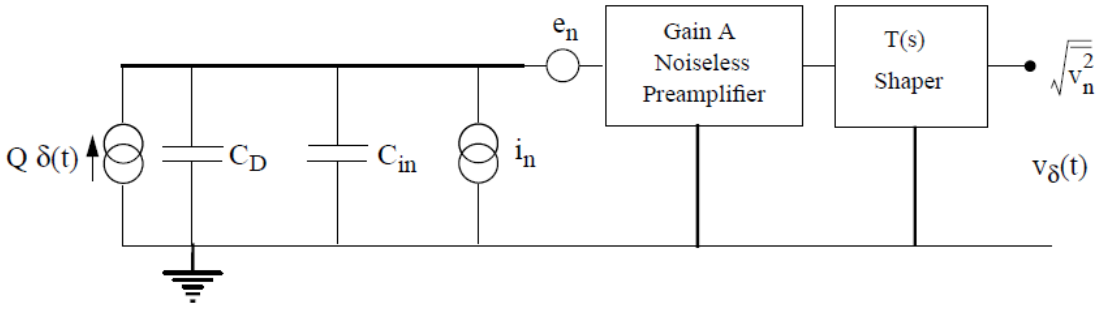

Figure 3.10: Amplifier noise generator schematic

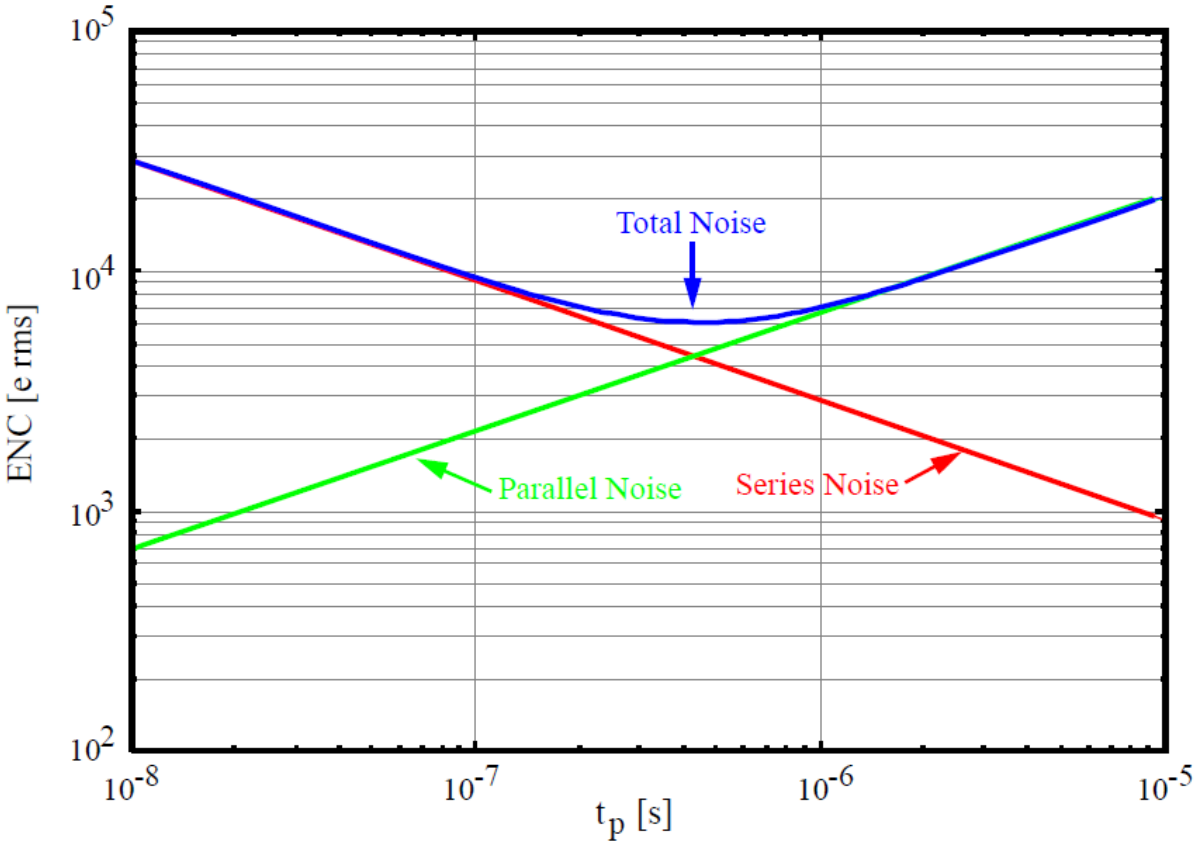

Figure 3.11: ENC contributions vs. Shaping time

to the method of shaping used and q is the charge of an electron. The dependence on the shaping time t_p for each contribution results in the relationship in Figure 3.11 when plotted logarithmically with typical values, in which the minimum total ENC is achieved when the series and parallel contributions are equal.

$$ENC = \frac{1}{q}\sqrt{\left(e_n{}^2(C_D + C_{IN})^2\frac{A_S}{t_p} + i_n{}^2 t_p A_P\right)} \tag{3.3}$$

3.4.2 SiPM Noise Analysis

The results from the simulation are then analyzed to understand the noise performance of the series connection. As seen in Table 3.2, the number of SiPM units that can be connected in parallel is limited by the approximately linear increase in ENC (neglecting parallel noise) due to the linear increase in capacitance from each unit, as suggested by Equation 3.3. The relationship is approximate, as capacitance matching with the input transistor also plays a part in the measured signal, which can be seen through a derivation of e_n, which has a dependance on both C_D and C_A, the amplifier's input transistor capacitance.

n Unit Arrangement	**Capacitance**	I_{MAX}	**ENC**
Parallel	nC	I	$\approx n * ENC_1$
Series	$\frac{C}{n}$	$\frac{I}{n}$	$\approx ENC_1$

Table 3.2: Analysis of one firing pixel in an SiPM array

An equal detector and input transistor capacitance maximizes the transfer of signal charge from detector to amplifier. However, as C_D is generally significantly larger than C_A, and the parallel connection only increases the equivalent detector capacitance, each additional parallel SiPM tends to increase the ENC linearly, as the signal charge remains the same for any firing pixel in the parallel array, but noise due to the increase in capacitance increases linearly.

Similarly, ignoring any capacitance matching effects, arranging n SiPMS in series lowers the noise seen at the amplifier inversely, since the total sensor capacitance becomes $\frac{C_{IN}}{n}$. However, as explained above, the signal from one SiPM is also divided by n. This gives the net effect of an ENC that is approximately equivalent to that of a single SiPM.

When comparing the parallel equivalent capacitance (nC) to the series equivalent capacitance ($\frac{C}{n}$), the difference is a factor of n^2. This is mathematically equivalent to n turns of an electromagnetic transformer. The use of electromagnetic transformers for capacitance matching between detectors and front end electronics is a well studied technique. Even if there are orders of magnitude in the difference between the detector capacitance and input transistor capacitance, the loss of energy transfer can be mitigated by the use of a transformer, so that the apparent capacitances are closer to a matching condition. This is because the effect of a transformer on both capacitances for the series contribution of the detector system is as shown in Equation 3.4 (Willis and Radeka, 1974), where ${\sigma_s}^2$ is the series noise variance and n is the number of SiPMs (or alternatively, the transformation ratio). The optimum number of SiPMs in series, n_{opt}, is given by Equation 3.5. The adjusted effect of capacitance matching on the ENC is seen in Equation 3.6, where the series array's ENC is in comparison to what the parallel array's ENC would be with the same amount of SiPMs.

$$\sigma_s^2 \propto \frac{C_D}{n} + nC_A \tag{3.4}$$

$$n_{opt} = \sqrt{\frac{C_D}{C_A}} \tag{3.5}$$

$$ENC_{series} \approx \frac{1 + \left(\frac{n}{n_{opt}}\right)^2}{n} * ENC_{parallel} \tag{3.6}$$

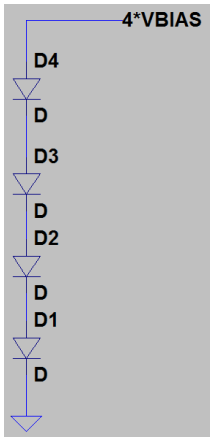

Figure 3.12: Biasing of series SiPM array

For the array to output usable data, the gains of the SiPMs must be significantly close to one another. This ensures that no matter which cell the photon collides with, the output current pulse will be the same. As shown in Equation 2.8, the gain of the SiPM depends on its bias voltage. If the SiPMs are manufactured identically, then when a bias is applied across an array of them in series, there should be an equal voltage drop over each one. If this is the case, then each SiPM will have the same gain. It should be noted that biasing an array of series connected SiPMs requires a higher total voltage, as seen in Figure 3.12. If the typical biasing voltage for one SiPM is V_{BIAS}, then the biasing necessary for n series SiPMs is nV_{BIAS}.

With a realistic approximation of capacitive values, such as a detector capacitance of $1nF$ and a transistor capacitance of $10pF$, the optimum number of series SiPMs would be 10. However, in practice, each successive SiPM placed in series will lead to additional capacitive connections to ground, creating a capacitive ladder divider. As more SiPMs are configured in parallel, more of the signal charge will be attenuated, limiting the usefulness of extensive series SiPMs, the equivalent of limiting the amount of turns on an electromagnetic transformer due to capacitances between each successive turn. Therefore, in the above example, where $n_{opt} = 10$, the actual number of series SiPMs is limited to four. In this case, the ENC will actually be reduced by ≈ 3.5 compared to the parallel array.

While biasing series-connected SiPMs, one additional concern is that the dark current is very low ($\approx 10pA$). In the case of manufacturing differences, the SiPMs may have have different leakage currents, which lead to unequal voltage drops across the sensors, and will result in unpredictable gains. One solution is to include high value resistors in parallel with the SiPMs, as shown in Figure 3.13. In this case, the current through the resistors will dominate over the dark current. If the resistors are well matched, this will create even voltage drops across each SiPM. When the photon event happens, the signal current will be prevented from flowing through the resistor due to its high impedance, and the output current will be amplified as normal.

While the natural voltage drop across the resistor-less series array depends on the properties of the SiPMs, in this case, it will depend on the resistor matching. As a starting point,

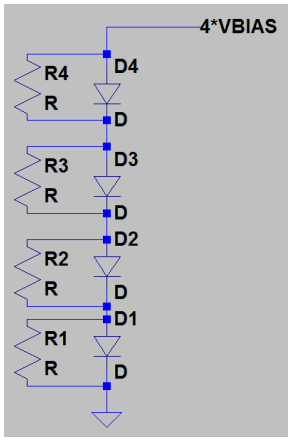

Figure 3.13: Biasing of series SiPM array with resistors

assume a desired gain matching within 5%, an operating V_{OV} of 2 V, and the relationship between the two shown in Equation 2.8. The difference in voltage drops across any identical series SiPM must be less than 100 mV. Given a nominal V_{BR} of 50 V, and the equivalency of $\frac{\Delta R}{R} = \frac{\Delta V}{V_{BR}+V_{OV}}$, the resistor matching must be within 0.2%, which is commercially available, but may be less so for resistors of higher values with similarly matched temperature coefficients at the cryogenic conditions of the nEXO experiment.

Choosing the values of the biasing resistors is also another consideration. As a resistor as large as 1 GΩ would still lead to bias current that dominates the SiPM's leakage current, there is no upper bound on what the resistors could be, besides availability and tolerance. However, the lower the resistor is, the more bias current will be flowing, leading to more power being used. With this information, initial concepts of larger size arrays are conceptualized. Two such arrays are shown in Figure 3.14. These are concepts for a hybrid series/parallel arrangement of 16 SiPMs. Both methods would result in the overall capacitance and Signal to Noise ratio of a single SiPM, as well as a required overall voltage of $4V_{BIAS}$. However, analysis shows that the arrays would require a different number of resistors, as well as different minimum resistor values.

As a baseline value, assuming that the array of 16 SiPMs covers an area of approximately $10cm^2$, approximately 4000 such arrays would be required for the expected area of $4m^2$. Additionally, a practical value for the "Power Budget" associated with biasing the array is 1 W, and the V_{BR} of a typical SiPM is $\approx 50V$, which means the total biasing voltage would be larger than $200V$. In accordance with $P = \frac{V^2}{R}$, the equivalent resistance of the entire setup must be larger $40k\Omega$ for the default power draw to remain under 1 W. As each array of 16 SiPMs would be arranged in parallel with the others, each individual array of the 4000 requires an equivalent resistance of $160M\Omega$.

The array in Figure 3.14a) requires 16 resistors, each with a value of $160M\Omega$ to achieve this equivalent resistance (only one column of the resistors is shown). In comparison, Figure 3.14b) requires only 4 resistors, and each can be $40M\Omega$ and the array resistance will equate to $160M\Omega$. Overall, if resistors are required, an array similar to b) appears to be more effective, as it requires fewer resistors, and resistors of smaller values, which will be

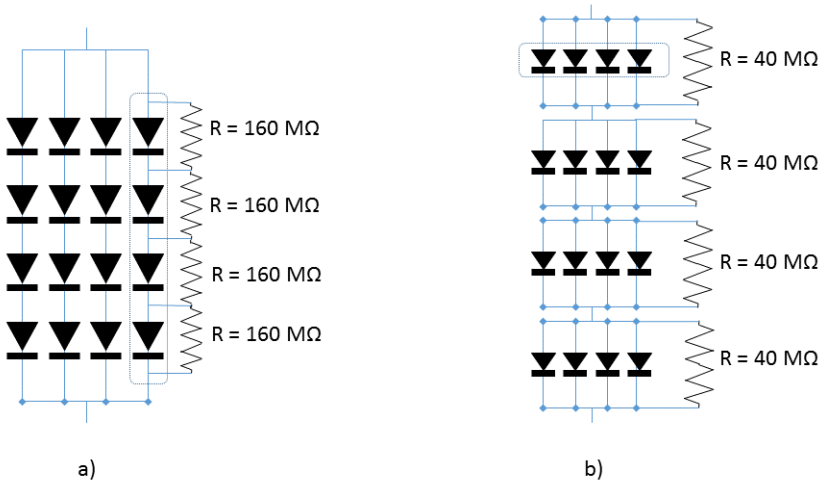

Figure 3.14: Concepts of mixed series/parallel arrays (Adapted from Rescia et al., 2016)

easier to source with the tolerance and temperature coefficient required.

Chapter 4

Measurements

4.1 Introduction

The nEXO collaboration used SiPMs obtained from two manufacturers, Hamamatsu and FBK. The SiPMs from Hamamatsu are four quadrant units, shown in detail in Figure 3.5. Units that had one defective quadrant were sent to the collaboration for testing, so only three of the quadrants are able to be used for each unit. An image of a Hamamatsu MEG unit is shown in Figure 4.1, where each cell has an anode and cathode output that is connected to 8 pins on the back of the unit.

Additionally, FBK sent samples of SiPMs from their NUV product line. These SiPMs are sent as bare dies, with the cathode on a conductive plane on the back of the substrate, and the anode connection on a bonding pad at the top of the unit. Upon being received, a housing was designed to mount the units. Then, their response to pulsed light is analyzed to see if the units could be connected in series.

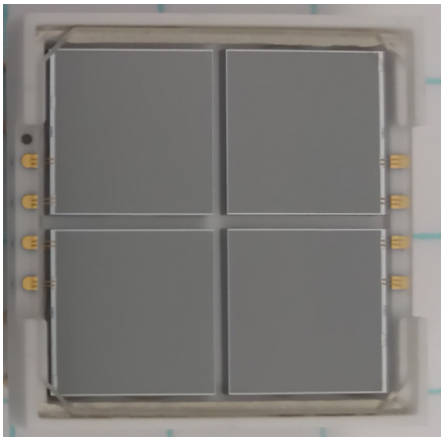

Figure 4.1: Hamamatsu MEG SiPM

4.1.1 SiPM Housing

Since the SiPMs have a unique size and shape, a new housing is necessary for each device. The housing provides a threaded input for the optical FC connector to deliver incident light to the SiPM, while also blocking ambient light. It also needed to provide a method of connecting the anode and cathode of the SiPM to any circuitry used to apply the bias voltage and output the current pulses.

The housing is designed to be 3D printed as two circular parts, a bottom that mounted the SiPM and connected it with its output pins on the other side, and a top that would cover the sensor while including an FC-threaded input that directed light from a fiber-optic cable into it. For the MEG units, the bottom piece is designed to include eight through holes to match the sensor's pin array. The through holes had female receptacles installed which the SiPM could plug in to. For the DC measurements, the probes could be attached directly to the receptacles connected to the quadrants to be measured. For the pulsed light measurements, a custom PCB is fabricated that would filter a bias voltage and apply it to a single or multiple quadrants in parallel or in series depending on a 0 Ω resistor network that could be altered to the configuration desired. The circuit also provided a low impedance output for the signal through a micro-coaxial (MCX) output. A side view of the components of the fixture is shown in the top image of Figure 4.2. The threaded part of the fixture had a recess that the square SiPM would fit into to block ambient light. Two versions of this part are designed, allowing the optical cable to shine on one or all of the quadrants as desired for the tests, as seen in Figure 4.3. Mounting holes are aligned and threaded so that screws would be inserted through the circuit mounting holes and bottom piece and threaded into the top piece, securing the unit as a whole. The sensor holder as used in the pulsed light experiment is shown in the bottom image of Figure 4.2.

The FBK NUV SiPM housing required a bare die to be mounted. As with the above housing, the bottom piece had two pins inserted to mate with the Sensor Holder circuit. Offset from those pins is a recess in which a small copper plate is glued to. The back (cathode) of the SiPM is connected to the copper plate with silver epoxy to preserve conductivity. Then, the copper plate and the anode tab are wire bonded to the two pins. The top piece, as in the first housing, consisted of a male-male FC connector positioned so that it would shine directly on the sensor. The top and bottom piece, along with the front and back of the final assembly, are shown in Figure 4.4.

4.2 DC Properties

4.2.1 Experimental Setup

DC properties of the SiPMs are measured unsing an Agilent B1500A Semiconductor Device Analyzer. The instrument includes various Source-Measurement Units (SMUs) and Capacitance Measurement Units (CMUs) that can be used to analyze the SiPMs through I-V and C-V curves. The instrument, with the testing fixture on top of it, is shown in Figure 4.5.

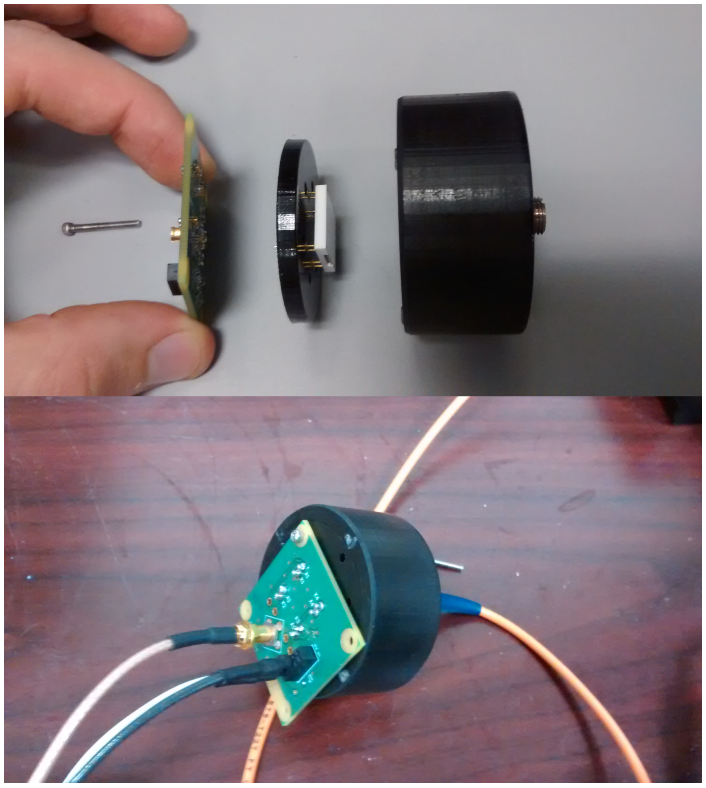

Figure 4.2: Hamamatsu SiPM fixture

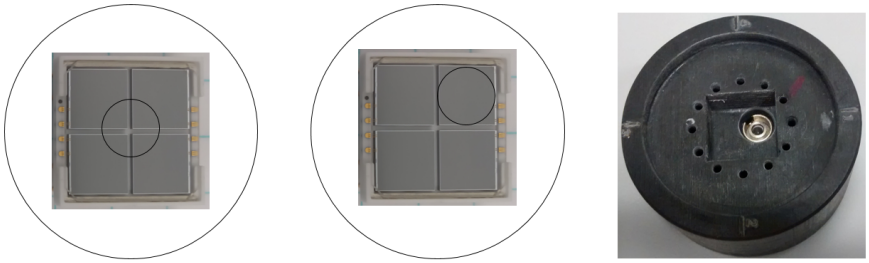

Figure 4.3: Hamamatsu SiPM fixture configured for various light patterns

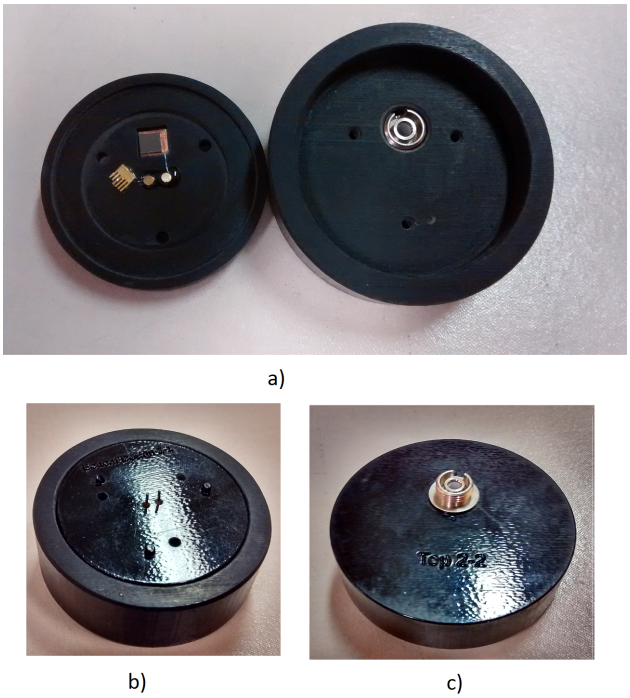

Figure 4.4: FBK SiPM holder

Figure 4.5: Agilent B1500A Semiconductor Device Analyzer

Figure 4.6: Cloth used to block light for DC measurements

The SMU connections, located in the testing fixture on top, include various voltage and current probes that can either "Force", providing a bias or "Sense" and measure the electrical property. For these measurements, no circuitry or optical connector is needed, and the probes are directly connected to the pins. The measurement fixture has a hinged top. To ensure that the ambient light affected the measurement as little as possible, a black felt cloth is placed over the fixture, as in Figure 4.6. Additionally, the room lights are switched off during measurement. All tests are conducted at both room temperature and with the sensor submerged in liquid nitrogen in order to approximate the SiPM behavior in the reduced temperature of liquid xenon.

4.2.2 Results

4.2.2.1 Forward Bias IV Curve

All three functioning quadrants on each MEG SiPM are charactarized individually at room temperature. The resulting I-V and C-V curves are included in Appendix A. Firstly, the forward bias characteristics of the SiPMs are measured. In this case, each cell functions as a diode, where applying a forward bias voltage higher than the built-in potential results in exponentially increasing current. In this case, the quenching resistor R_Q limits the output current linearly. A representative forward IV curve is shown in Figure 4.7.

In accordance with Ohm's Law, the inverse of the slope of this linear current will be the value of the resistor in series with the diode, which in this case is the equivalent resistance of all the quenching resistors in parallel. While measuring the different quadrants, the equivalent resistance generally ranged from $18.5 - 19.5\Omega$. Since all N cells in an array are in parallel, the equivalent resistance is actually $\frac{R_{EQ}}{N}$. For the MEG device, the total number of active pixels in a quadrant is 13923. Assuming manufacturing uniformity, this leads to an R_Q

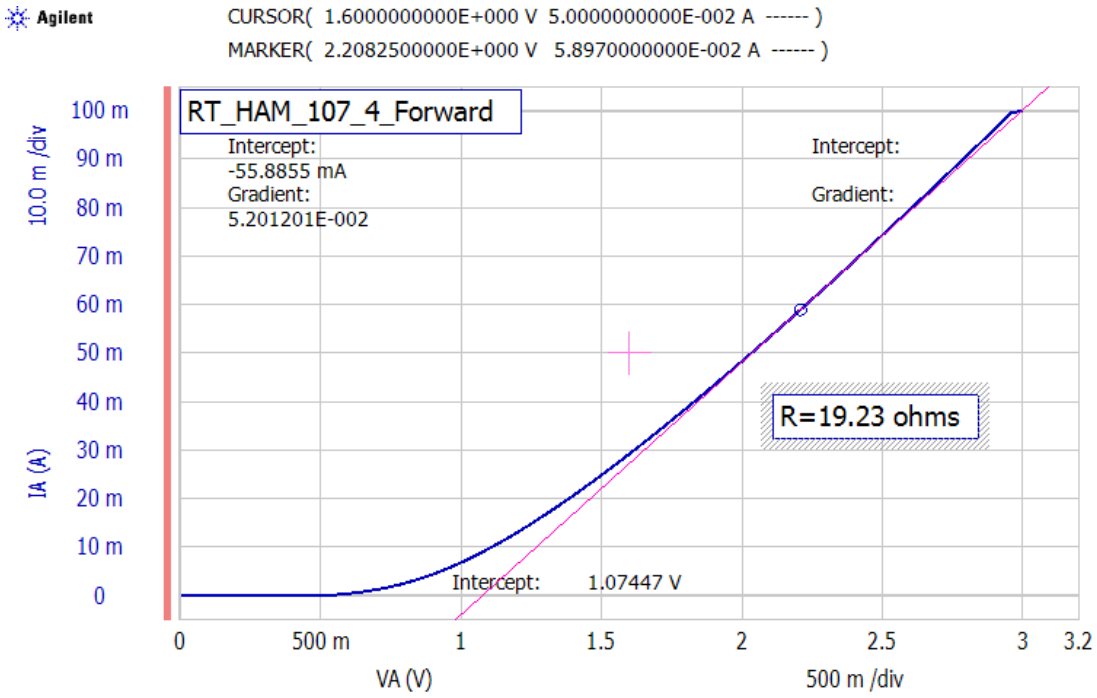

Figure 4.7: Hamamatsu MEG Unit 107, Quadrant 4, forward IV curve - Room temperature

of about 260 $k\Omega$ for each individual cell. The measurement is repeated while submerging the sensor holder in liquid nitrogen. The resulting forward IV curves are of the same shape, with the calculated R_{EQ} values generally ranging from 21.4 - 21.7 Ω, giving an approximate R_Q of 300 $k\Omega$. This illustrates that the polysilicon R_Q's resistance increases as the temperature is lowered.

The FBK NUV sensor is measured as well. At room temperature, the measured equivalent resistance is 46.5 Ω. As the number of pixels in the NUV device is 8,645, this corresponds to an R_Q of 400 $k\Omega$. While submerged in liquid nitrogen, it is 115.6 Ω, which means on average, each R_Q is 1 $M\Omega$. While the details of the polysilicon resistors are unknown, it's evident that the type used in the FBK device changes more with temperature.

4.2.2.2 Reverse Bias IV Curve

Of utmost importance is the the reverse bias IV curve for each sensor. The data obtained in this measurement provides information on what the bias voltage can be set to, and gives a measure of the relative dark rate for the device. The result for a typical Hamamatsu quadrant at room temperature is shown in Figure 4.9. The blue plot is the measured current, while the orange plot is the normalized derivative of the current (defined as $\frac{1}{I}\frac{dI}{dV}$), which assists in identifying the regions of operation. With a voltage lower than V_{BR}, the leakage current is steady at around 5 nA. The first peak of the derivative signals the breakdown voltage, in this case, 64.27 V. At this point, the current increases with the increasing negative voltage, due to the relationship between V_{BIAS} and the dark rate. The next derivative peak,

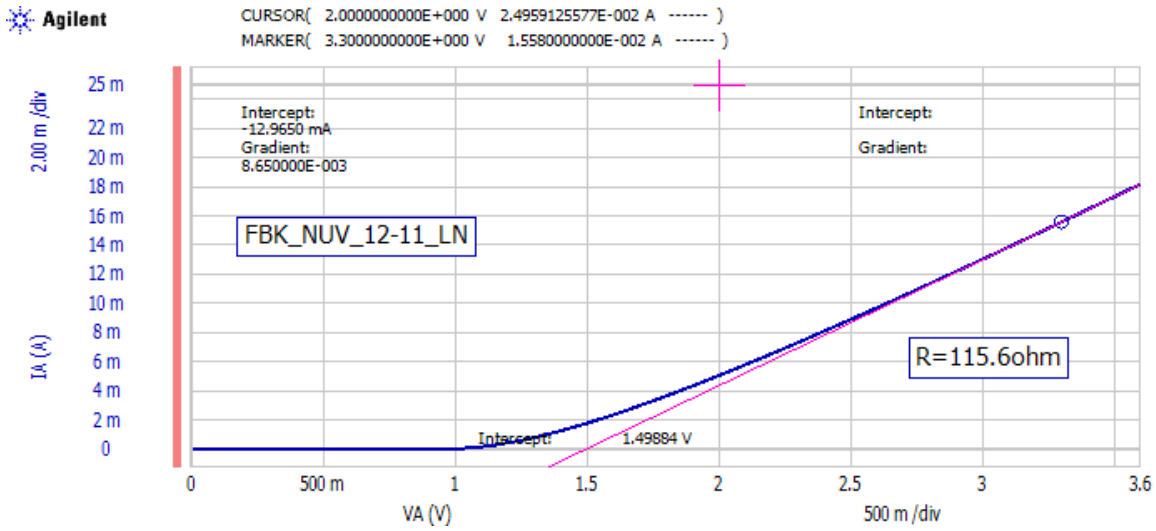

Figure 4.8: FBK NUV 12-11 Unit forward IV curve - Room temperature

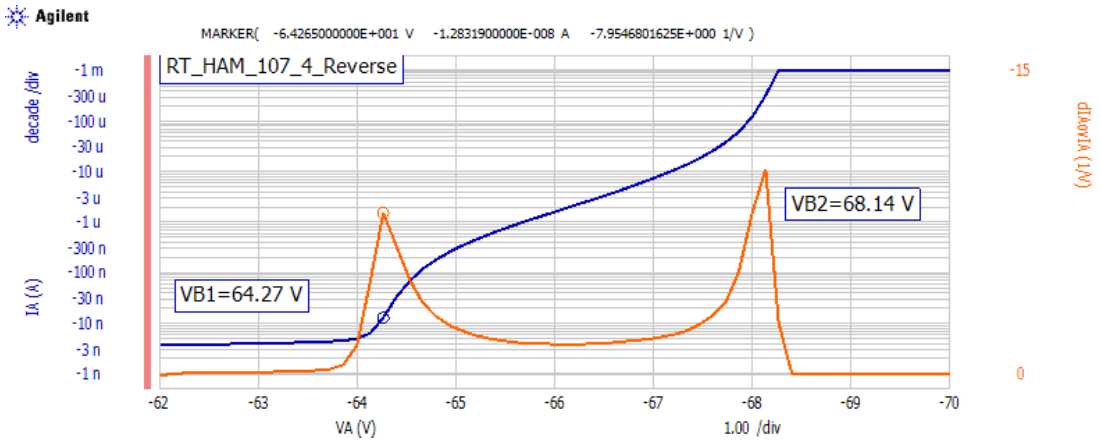

Figure 4.9: Hamamatsu MEG Unit 107, Quadrant 4, reverse IV curve - Room temperature
Blue line - Current (A) Orange - Normalized derivative of current

sometimes informally known as the "Second Breakdown Voltage", marks the beginning of the "instability" region described in Section 2.2.3. The current is limited at 1 mA to prevent damage to the unit. This plot shows that there is roughly a 4 V operational range where the unit can operate in Geiger mode.

Submerging the unit in liquid nitrogen and repeating the reverse bias test gives results such as those seen in Figure 4.10. As is shown, for a well functioning SiPM being tested in a dark environment, lowering the temperature to 77K reduces dark current to very low levels. The leakage current up until the second breakdown voltage is generally below 100 pA, which actually makes it more difficult to identify the first breakdown voltage. Measurements with this response at cryogenic temperatures are then repeated with the cloth removed in order for ambient light to provide noticeable current at the breakdown voltage. However, as seen in Figure 4.11, some quadrants exhibited enough leakage or dark current at cryogenic temperature to identify the separate regions of reverse bias. This is most likely due to

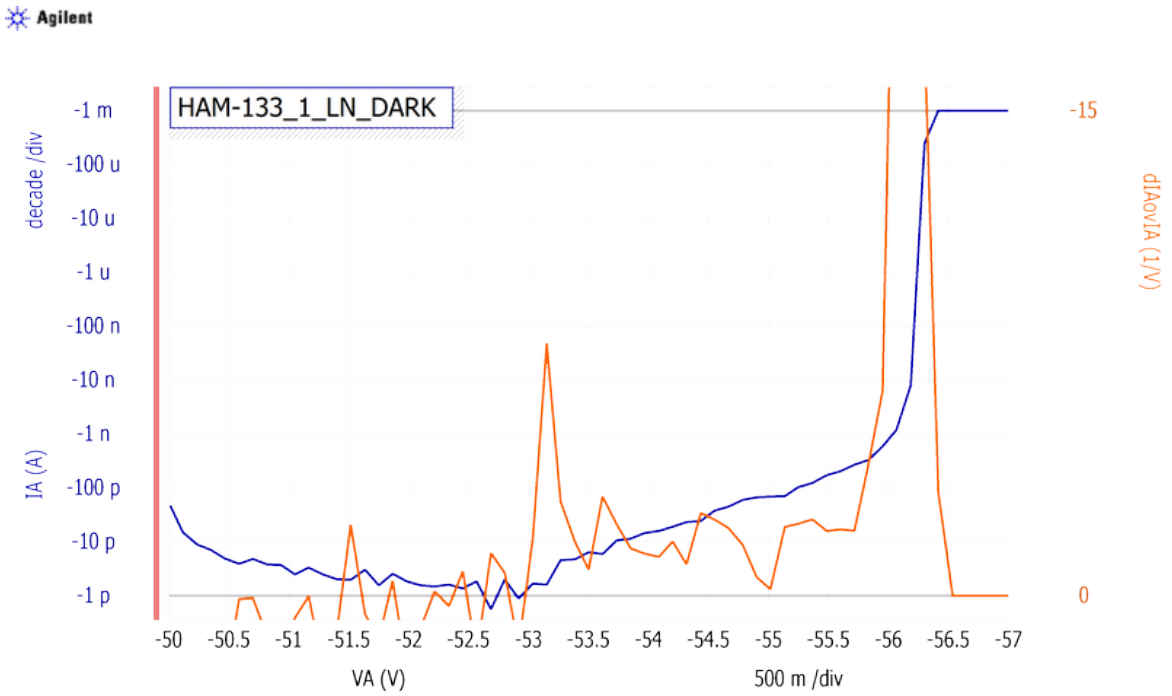

Figure 4.10: Hamamatsu MEG Unit 133, Quadrant 1, reverse IV curve - Liquid nitrogen
Blue line - Current (A) Orange - Normalized derivative of current

manufacturing defects, as the SiPMs procured were rejected from the MEG experiment, although the quadrants measured are not the one identified as the defect. More samples would be required to fully characterize the MEG units' cryogenic reverse bias characteristics. In general, leakage current is much lower at cryogenic temperatures, and the breakdown voltage dropped as well. The total operating voltage window remained approximately the same size, but both breakdowns shifted about 12 V lower.

The same measurement is repeated for the FBK SiPM. The room temperature results are shown in Figure 4.12 and the cryogenic temperature results in Figure 4.13 in a dark environment and Figure 4.14 with some light. Lowering the SiPM to cryogenic temperature appears to be very effective at reducing dark current down to the hundreds of pA. One immediate observation that can be made is that the 8 V operating voltage at room temperature is significantly lowered to less than 2 V at cryogenic temperature. This is believed to be due to the the changing depletion region at operating voltages, and is discussed below.

4.2.2.3 Reverse Bias CV Curve

Additionally, the overall capacitance of the SiPMs is measured against an increasing negative bias. The results for the Hamamatsu unit while submerged in liquid nitrogen are shown in Figure 4.15. Multiple plots are shown as the capacitance measurement can be taken at different frequencies. As can be seen, the capacitance decreases until about -25 V, at which point the junction is fully depleted. As the voltage approaches the operating

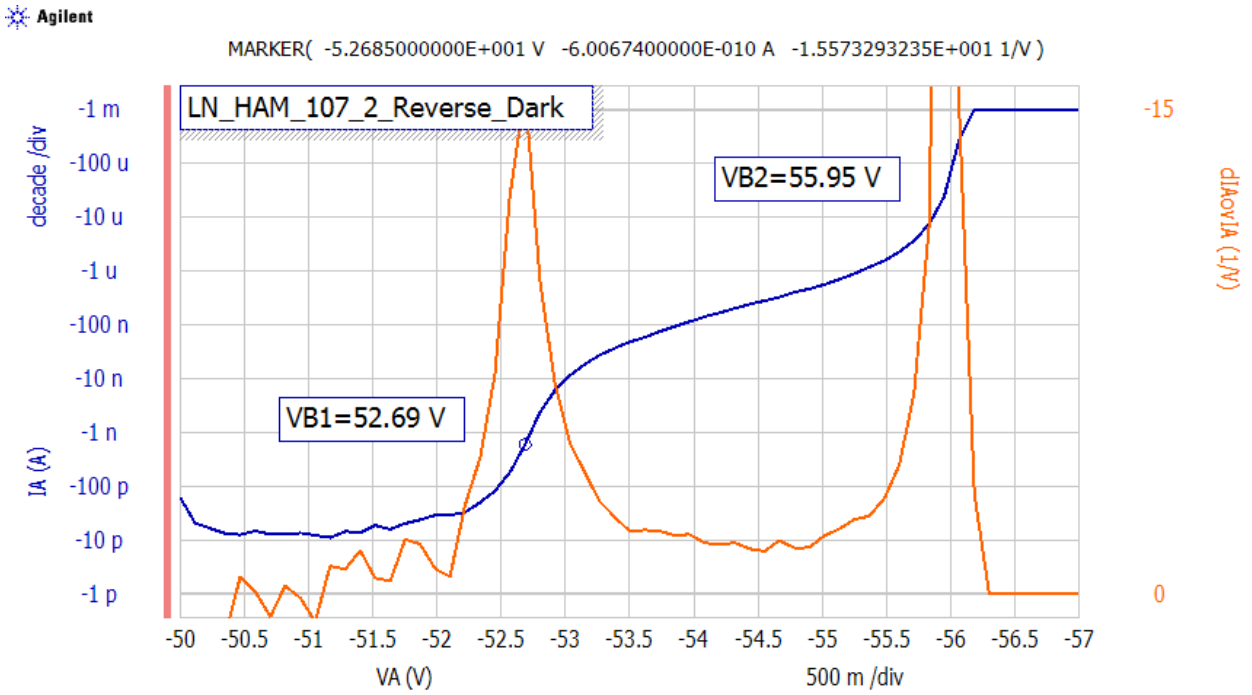

Figure 4.11: Hamamatsu MEG Unit 107, Quadrant 2, reverse IV curve - Liquid nitrogen, second type of response
Blue line - Current (A) Orange - Normalized derivative of current

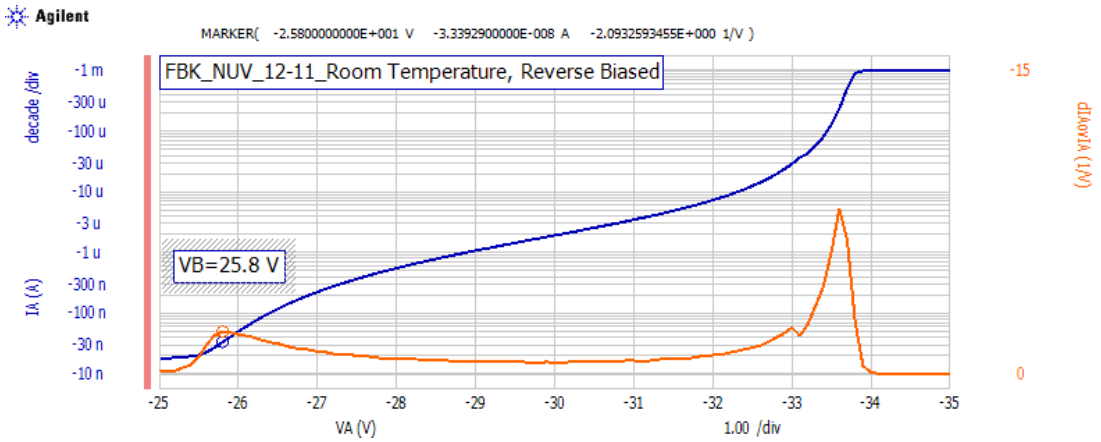

Figure 4.12: FBK NUV 12-11 Unit reverse IV curve - Room temperature
Blue line - Current (A) Orange - Normalized derivative of current

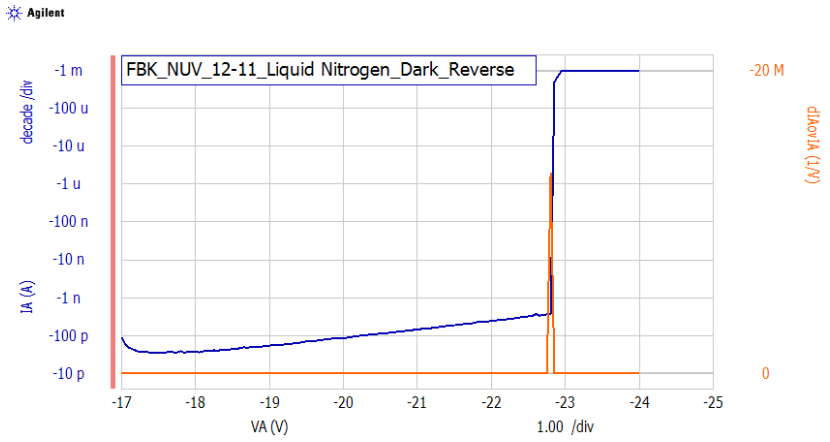

Figure 4.13: FBK NUV 12-11 Unit reverse IV curve - Cryogenic temperature - Dark
Blue line - Current (A) Orange - Normalized derivative of current

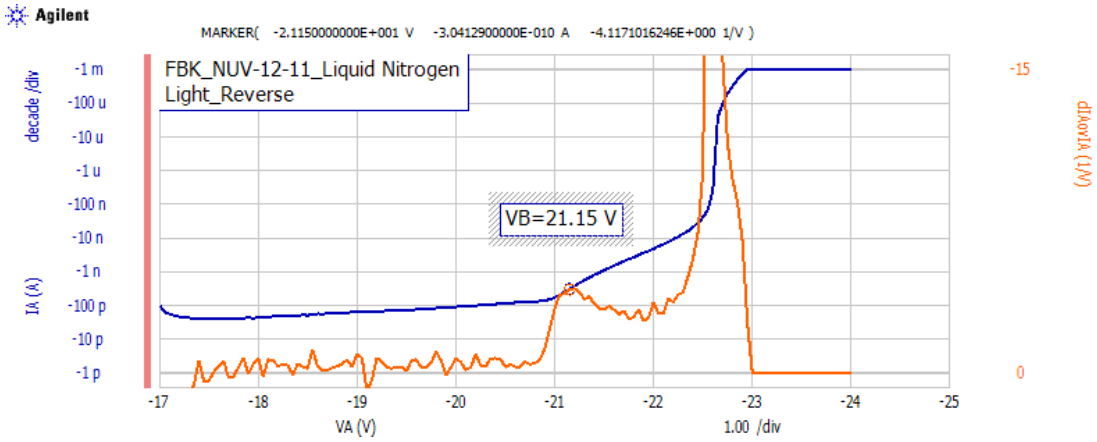

Figure 4.14: FBK NUV 12-11 Unit reverse IV curve - Cryogenic temperature - Light
Blue line - Current (A) Orange - Normalized derivative of current

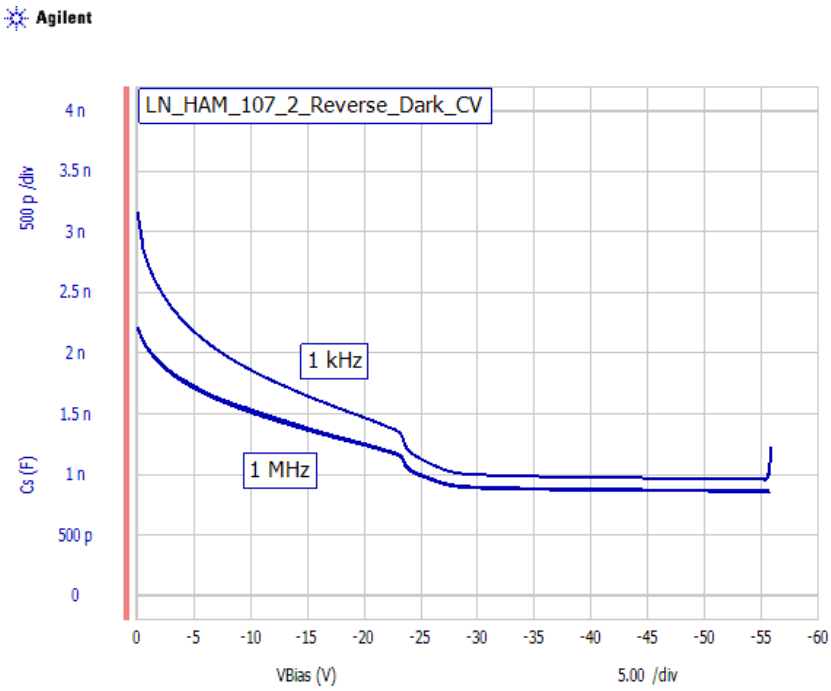

Figure 4.15: Hamamatsu MEG Unit 107, Quadrant 2, reverse CV curve -Liquid nitrogen

range, the capacitance is constant at approximately 0.9-1 nF. As previously noted, this is the total capacitance of 13923 pixels in parallel, so the average individual capacitance is approximately 70 fF. The capacitance is higher at room temperature at about 1.2 nF.

Similarly, the FBK NUV unit's CV parameters are analyzed. As seen in Figure 4.16, it appears that the junctions are not fully depleted, and the operating capacitance actually changes with bias voltage in the operating region. Also, while the capacitance does fall at cryogenic temperature relative to the operating voltage, the operating capacitance is actually higher at that lower temperature than the operating capacitance at room temperature.

4.2.2.4 Series Connection Measurements

The next DC measurements are taken with the three functioning quadrants of the Hamamatsu MEG units connected in series, both with and without external resistors. This is done by connecting the pins in the manner of Figure 4.17, shown schematically in Figure 4.18a) and b).

As described in Section 3.4, the three quadrants will generally have an equal voltage drop, although inherent differences in the SiPMs mean the array may not bias evenly, leading to different V_{OV} values for each quadrant, and thus different gains. One method to force a fixed voltage drop across each quadrant would be to connect a large resistor in parallel with each quadrant. Ohmite 1 G Ω resistors are used, as they had previously been tested at cryogenic temperatures for the MicroBooNe experiment at Fermilab. A small current will flow through the resistors and bias the SiPMs so that each quadrant has an equal voltage drop. As soon

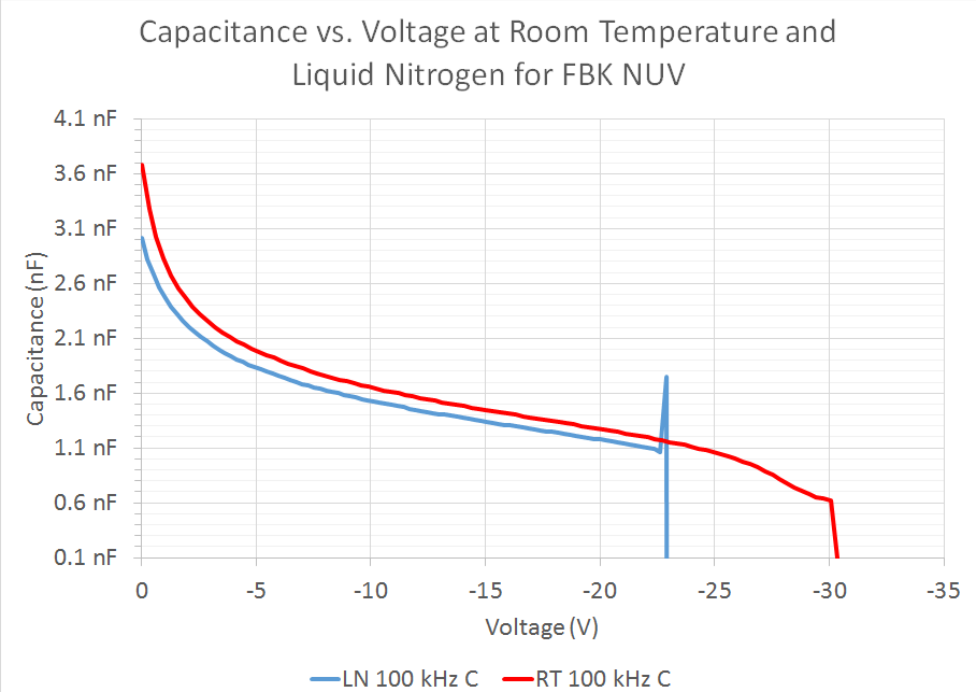

Figure 4.16: FBK NUV 12-11 Unit reverse CV curve - Room and cryogenic temperature

as a quadrant fires, that current will dominate and the resistor current will be insignificant to the output pulse.

As there are only three Hamamatsu SiPM units able to be tested, it's difficult to ascertain what the "typical" response. is. While the measurement is taken at both room temperature and with the unit submerged in liquid nitrogen, the liquid nitrogen result is of most interest in this case. A representative series IV sweep with a dark environment and no resistors is shown Figure 4.19. The blue plot is the current, and the other colored plots are the difference in voltage drops, e.g., $V_{AK1} - V_{AK2}$ from Figure 4.18. As expected, the breakdown voltage of the series connection is approximately three times higher than the individual breakdown for any quadrant in the array. As can be seen, at liquid nitrogen temperatures, there is very low leakage current before the breakdown voltage, and subsequently, there is enough mismatch between the SiPMs that there is a significant (more than $1V$) difference in the self-imposed voltage drop of one of the quadrants when compared to the others. At the breakdown voltage, where current begins flowing, the voltage drops become fairly close, within approximately 200 mV. However, as the applied voltage increases, the voltage drops diverge, before converging again at the instability region.

This general pattern is observed in the SiPMs tested, although there is some variation in how well matched the voltage drops are before the breakdown voltage and after the instability region. One explanation for this behavior could be that the separate quadrants exhibit different dark count rates. When each SiPM's individual quadrants' reverse IV curves are measured at the liquid nitrogen temperature, with great care being taken to minimize the ambient light in each case, they still exhibited slightly different rates of increase for the current. This is thought to be due to inherent manufacturing differences in the quadrants,

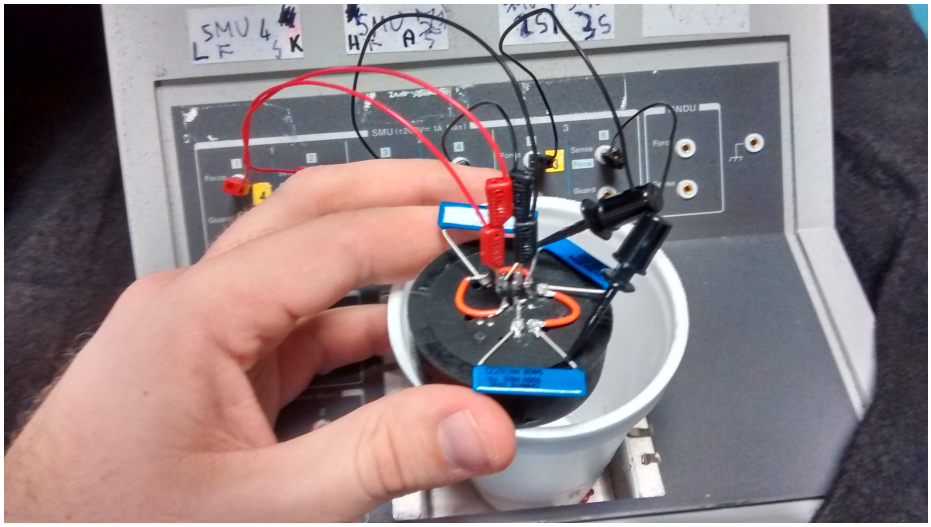

Figure 4.17: Series connection of Hamamatsu MEG unit for DC measurement

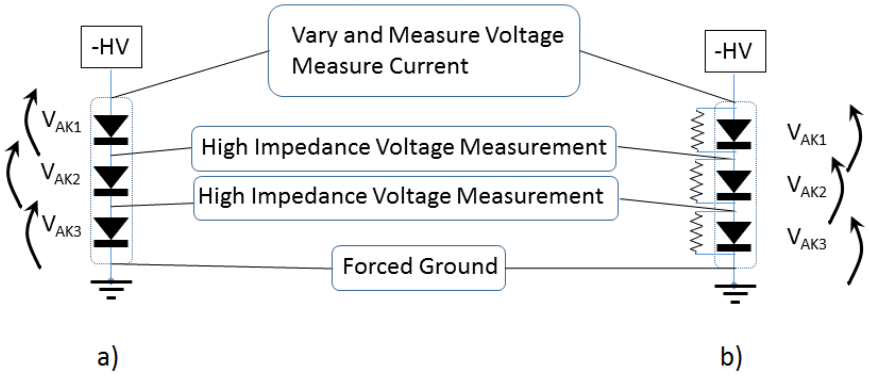

Figure 4.18: Series connection schematic of Hamamatsu MEG unit for DC measurement (Adapted from Rescia et al., 2016)

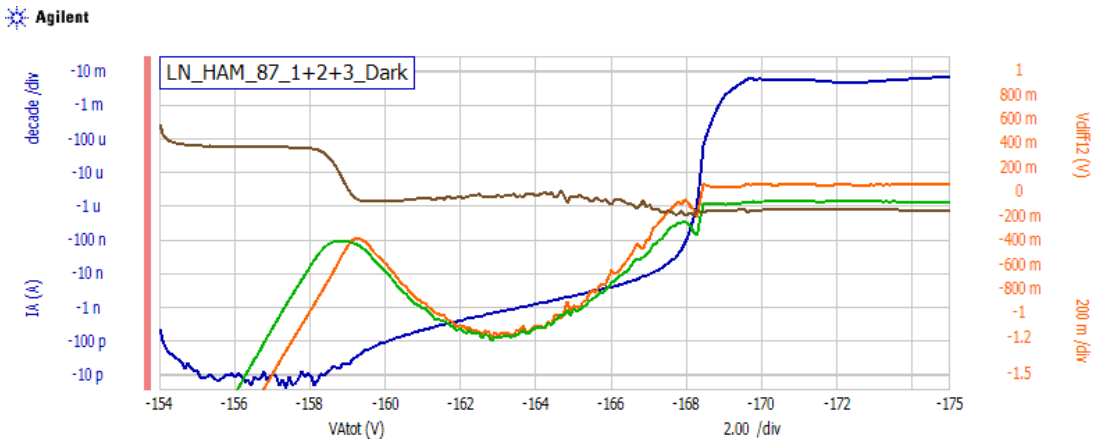

Figure 4.19: Series connection IV results of Hamamatsu MEG Unit 87 at liquid nitrogen temperature with no resistors
Blue: Current (A)
Orange: $[V_{AK1} - V_{AK2}](\mathrm{V})$
Green: $[V_{AK1} - V_{AK3}](\mathrm{V})$
Brown: $[V_{AK2} - V_{AK3}](\mathrm{V})$

or it could be related to the SiPMs received being defective units. In either case, for a given applied bias voltage, different quadrants on the same SiPM may exhibit dark currents up to an order of magnitude different from each other. Since significant dark current begins flowing at the same breakdown voltage for each quadrant, it's possible thatthe middle of the operating region is where different SiPM's dark currents tend to have the largest relative difference between them. This may lead to the type of response seen in Figure 4.19, where immediately after the breakdown voltage, the quadrant whose dark current increases the most "decides" the voltage drop across it, which would lead to another quadrant's individual voltage drop being reduced. However, as all the quadrants' dark current approaches the μA level, all the quadrants' dark rates increase exponentially and the differences become less significant, leading to individual voltage drops that are more uniform. While this is only speculation, the effect on the IV curve is clear, and there appears to be a local maximum of the difference in the "naturally occuring" voltage drop right at the operating region where the SiPMs would actually be biased in normal use, although, as discussed below, this may be a limitation of this method of measurement.

The same measurement is repeated with Ohmite $1G\Omega$ resistors connected across each quadrant. The resistors are chosen to be matched to 0.1% at room temperature, and the liquid nitrogen IV curve of only the resistors connected in series is shown in Figure 4.20. As can be seen, around the operating applied voltage, their voltage drops differ by less than 200 mV. A typical result of the three resistors connected in series during an IV with the three series SiPM quadrants is shown in Figure 4.21. The resistors help to keep the dark current below the breakdown voltage at a steady value, which means the individual voltage drops below the breakdown voltage are closer together than without the resistors. As the dark current increases though, the current through the resistors becomes negligible, and the "natural" behavior of the SiPM array takes over, although the maximum voltage mismatch

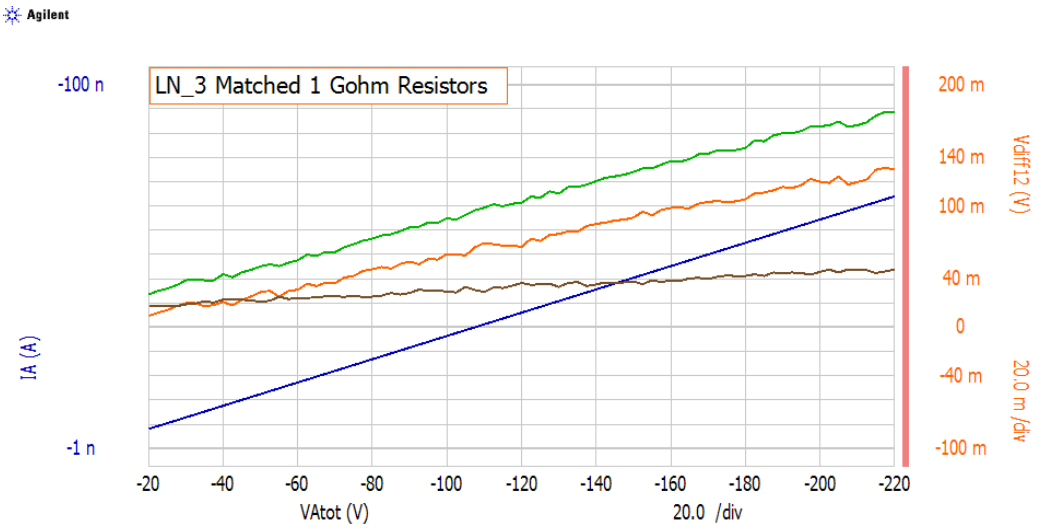

Figure 4.20: Series connection IV results for Ohmite $1G\Omega$ resistors at liquid nitrogen temperature
Blue: Current (A)
Orange: $[V_{R1} - V_{R2}](\mathrm{V})$
Green: $[V_{R1} - V_{R3}](\mathrm{V})$
Brown: $[V_{R2} - V_{R3}](\mathrm{V})$

in any two quadrants is 200 mV in the case with the resistors, compared to around 1.2 V without the resistors.

While the IV curves give approximations on the behavior of the reverse biased photodiodes, it's difficult to definitively come to a conclusion about the effectiveness of either array. The Semiconductor Analyzer used for these measurements is unable to record an individual transient event, so the current and voltage drops seen are more of a measure of the average dark current within the settling time of the machine's discrete measurements. To truly characterize the series array's usefulness, pulsed light measurements must be taken.

4.3 Pulsed Light Measurements

4.3.1 Experimental Setup

In order to test the SiPMs' responses to pulsed light, the setup in Figure 4.22 is used. The original schematic for the setup used is documented in Figure 4.23.

The light source used is from a Caen SP5601 LED Driver, seen in Figure 4.24. The driver outputted blue light pulses at a 405 nm wavelength at selectable frequencies or based on an external trigger. The flux intensity of the light could be adjusted by the knob on the front. The light is outputted through an optical fiber, and an electrical signal coincident to every light pulse could be outputted through a LEMO cable in order to synchronize the trigger

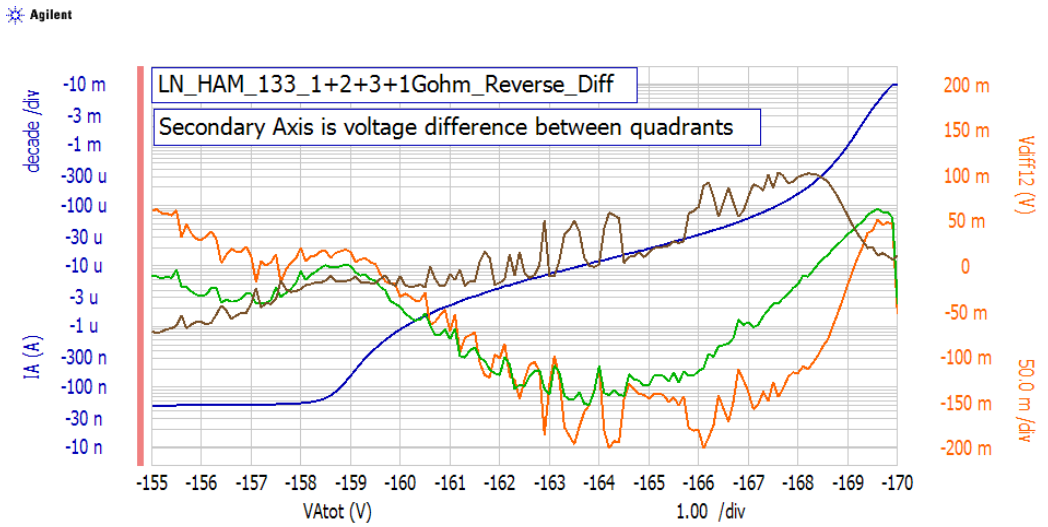

Figure 4.21: Series connection IV results of Hamamatsu MEG Unit 133 at liquid nitrogen temperature with resistors
Blue: Current (A)
Orange: $[V_{AK1} - V_{AK2}](\mathrm{V})$
Green: $[V_{AK1} - V_{AK3}](\mathrm{V})$
Brown: $[V_{AK2} - V_{AK3}](\mathrm{V})$

Figure 4.22: Pulsed light experimental setup

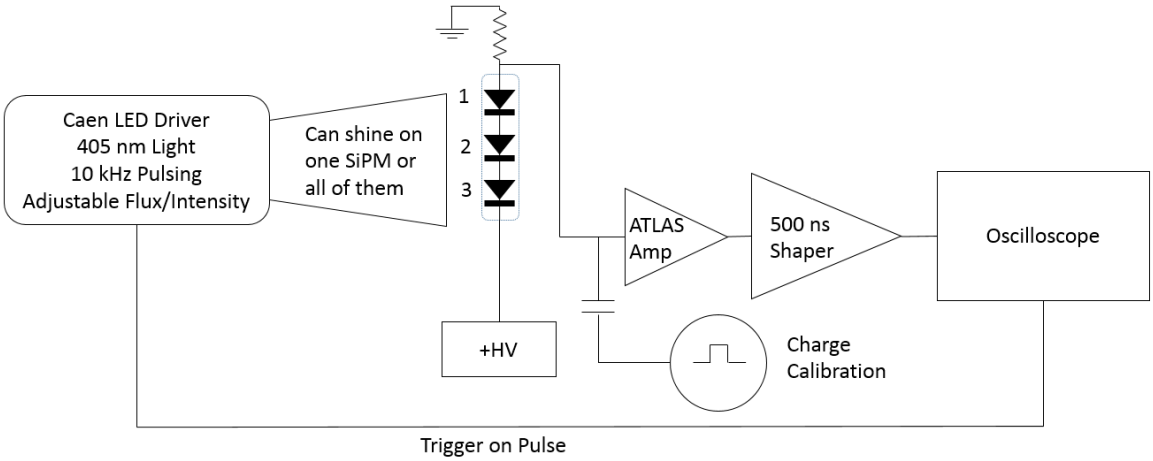

Figure 4.23: Pulsed light experimental setup schematic

on the oscilloscope. The SiPM or array of SiPMs is biased with the custom PCB, and the output MCX cable connected to the amplifier and shaper, which finally outputted the signal on the oscilloscope, a Tektronix DPO7354. All instruments are powered through a isolation transformer to mitigate the effect of a ground loop that had been initially measured.

The amplifier and shaper had been chosen based on availability. Brookhaven National Laboratory (BNL) had previously designed a high-performance amplifier, seen in Figure 4.25, for the ATLAS Calorimeter experiment and had extra amplifiers available. A CR-RC2 shaper has been modified to filter the output signal at a pulse time of approximately 500 ns.

4.3.2 Test Method

The SiPMs are tested in their sensor housings while submerged in liquid nitrogen, with ambient light blocked off. Initially, the LED driver provided the light source at it's lowest frequency, 10 kHz, and a Stanford Research Systems PS325 voltage source biased the voltage to the SiPMs. In this setup, with a bias voltage set within the operating region of the SiPM or SiPM array, the expected oscilloscope output similar to the type seen in Figure 2.8 is observed. The expected pulse heights could be interpolated by identifying the 0 p.e. peak coincident with the signal baseline, and noting the discrete peak heights that occur. The flux is adjusted so that most bursts of light from the pulser resulted in 1 p.e. events detected on the SiPM. A typical oscilloscope output for a 1 p.e. pulse can be seen in Figure 4.26. The trigger from the LED driver can be seen as the yellow signal. Also apparent is the histogram on the left side of the screen. For each acquisition of the scope, the value of the signal is recorded at the blue vertical line, which is positioned to coincide with the peak of the signal. These recorded values are used to build up a histogram of maximum signal heights that coincided with the pulsed light, as seen in Figure 2.14.

After acquiring enough data, relevant information about the SiPM (gain and noise of

Figure 4.24: Caen SP5601 LED Driver

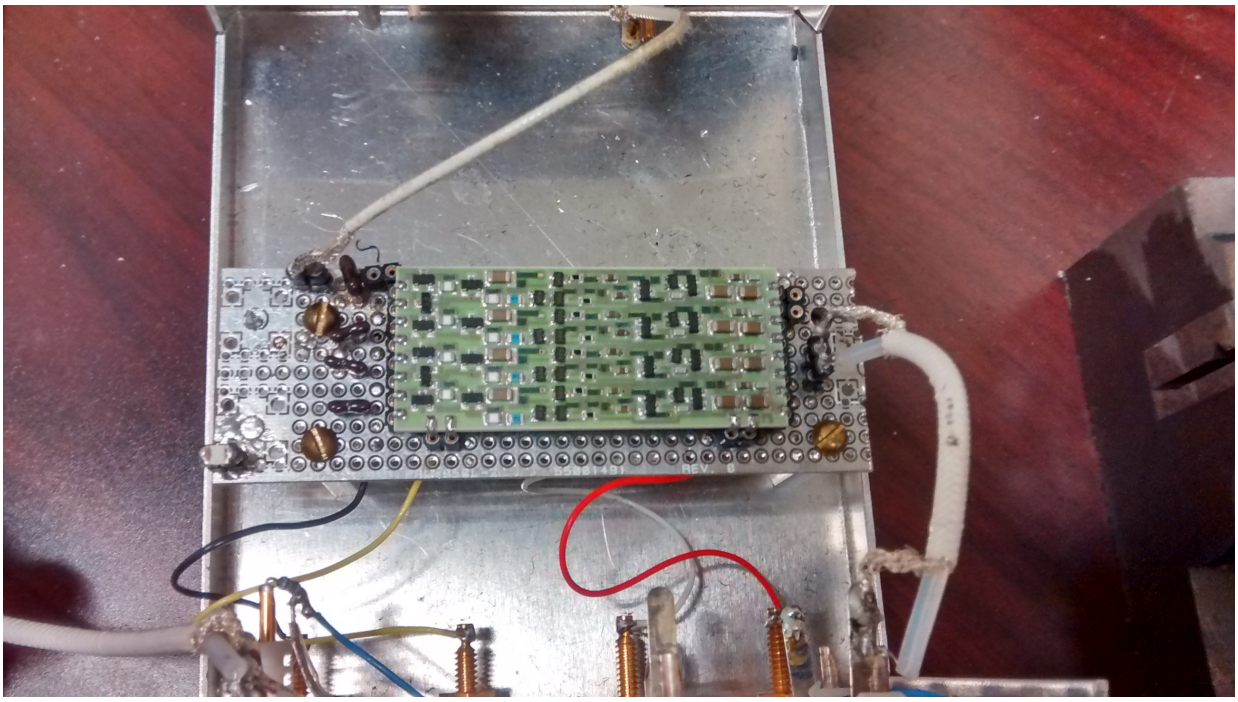

Figure 4.25: ATLAS calorimeter amplifier

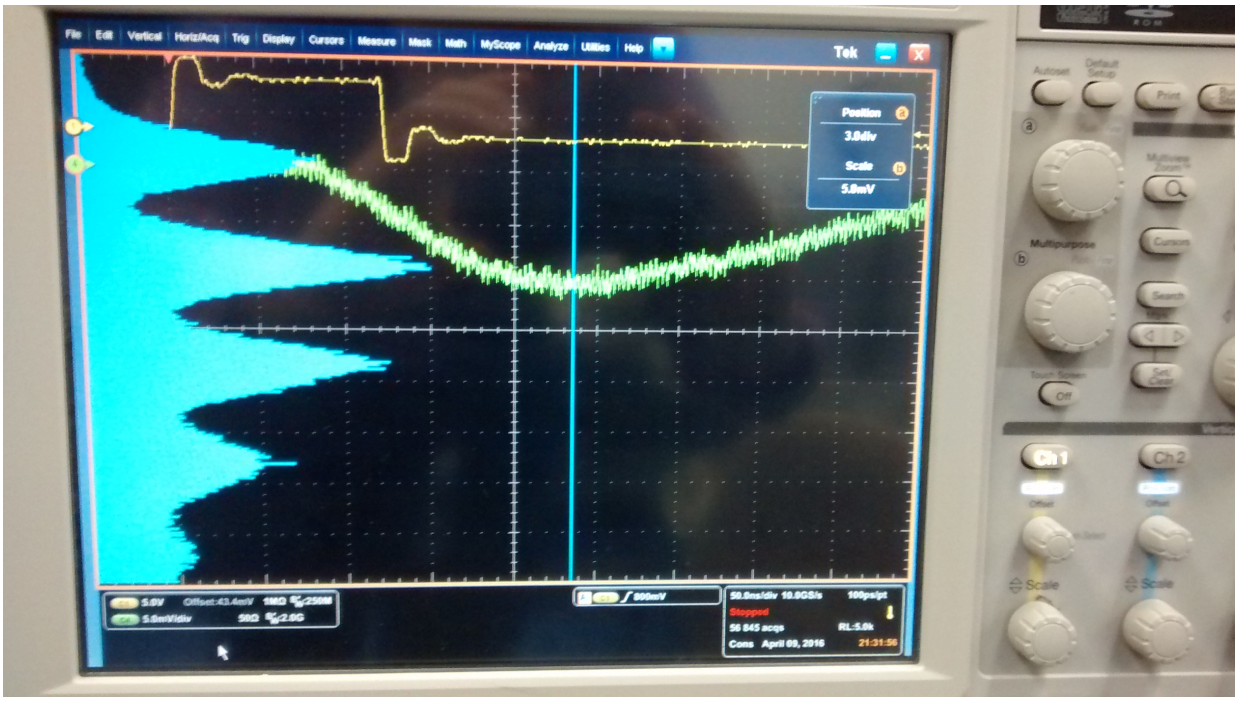

Figure 4.26: Typical SiPM shaped pulse output

the individual peaks) can be measured from the histogram. The gain can be calculated from the data using Equation 4.1. Δ_{PP} is the spacing between two chosen peaks, which will have units of mV, and n is the number of photons that the peak spacing corresponds to. For example, the spacing between the 3 p.e. peak and the 2 p.e. peak would correspond to a n value of 1. The $\frac{Q_{IN}}{V_{PEAK}}$ term is based on a test charge used to calibrate the amplifier.

$$M = \frac{\Delta_{PP}}{n} * \frac{Q_{IN}}{V_{PEAK}} \tag{4.1}$$

This is diagrammed in Figure 4.27, a closeup on the calibration charge system. Prior to the collection of a histogram, a voltage pulser is connected to the input of the amplifier in series with a capacitor. Through $Q = CV$, a 50 mV voltage step through a 2 pF capacitor led to an injection of approximately 625,000 electrons for each pulse, the system's Q_{IN}. The pulser is also used to trigger the oscilloscope, which measured the consistent pulse that is outputted. The height of this pulse is recorded as V_{PEAK}. This value is measured before each histogram to account for minor variations in amplifier gain due to factors such as room temperature.

Similarly, the measured ENC can be calculated for each individual peak as in Equation 4.2, where σ is the RMS width of the peak in mV. However, comparing the individual and series case of SiPMs cannot be approximated as a sensor that is simply changing capacitance. As shown in Section 3.4, the gain of the series configuration is reduced by the amount of SiPMs in series. This means that the test pulse that results from the same charge injection is n times higher than it should be in the case of n SiPMS in series, leading to the

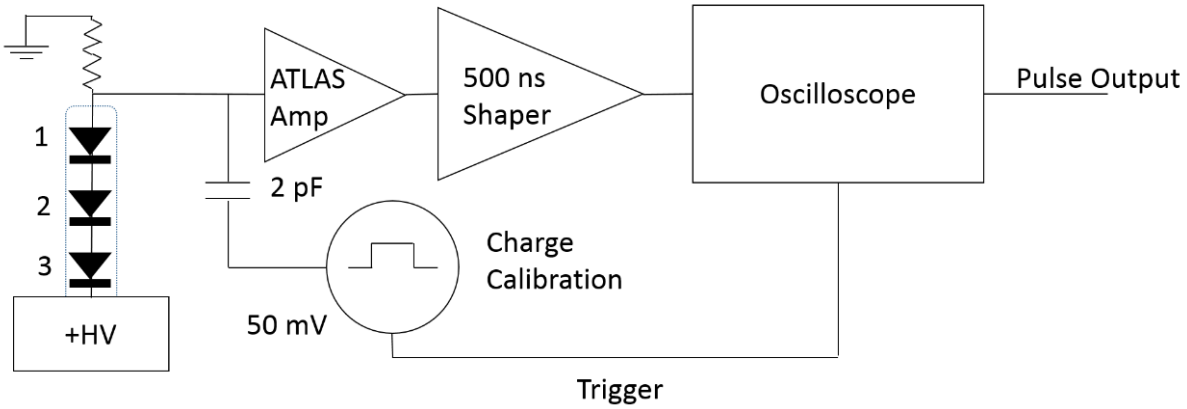

Figure 4.27: Test charge schematic

n term in the equation.

$$ENC = \sigma * \frac{nQ_{IN}}{V_{PEAK}} \tag{4.2}$$

Each SiPM or SiPM array is tested at a fixed voltage for approximately 25,000 signal acquisitions. For the individual quadrants, histograms are constructed at bias voltages for every 0.5 V, from approximately the breakdown voltage to the instability region. For the series connection, measurements are performed at every 1 V, due to the larger operating voltage range. The histogram data is exported from the oscilloscope and imported into MATLAB, where a data processing script has been written to analyze the peaks as above. Figure 4.28 shows the output from a typical histogram.

First, the script subtracts the wide gaussian noise characteristic of delayed afterpulsing from the histogram. In the top image of the figure, all data below the red curve is subtracted. The bottom image shows the resulting histogram. Then, the first three peaks (0 p.e., 1 p.e., and 2 p.e.) are iteratively isolated from the rest of the data as shown by the dotted lines. The data within the dotted lines are fitted to a gaussian, which gives the centroid and RMS width of the peak. Using the fitted centroids, the distance between the peaks can be found and multiplied by the charge calibration data that is measured for this specific histogram, as in Equation 4.1. This results in a final gain value for the SiPM configuration at this specific voltage. Similarly, the RMS width found by the gaussian fit is multiplied by the calibration constant to find the ENC for each peak. The full MATLAB script is included in Appendix B

4.3.3 Initial Results

With the testing conditions described above, the Hamamatsu MEG unit is initially tested. First, one quadrant of the unit is tested as an individual SiPM. Within the operating voltages, the gain is of the expected order of magnitude, $\approx 10^5$. As discussed in Section 3.3, the expected gain when three such SiPMs are connected in series would be $\frac{1}{3}$ the value of

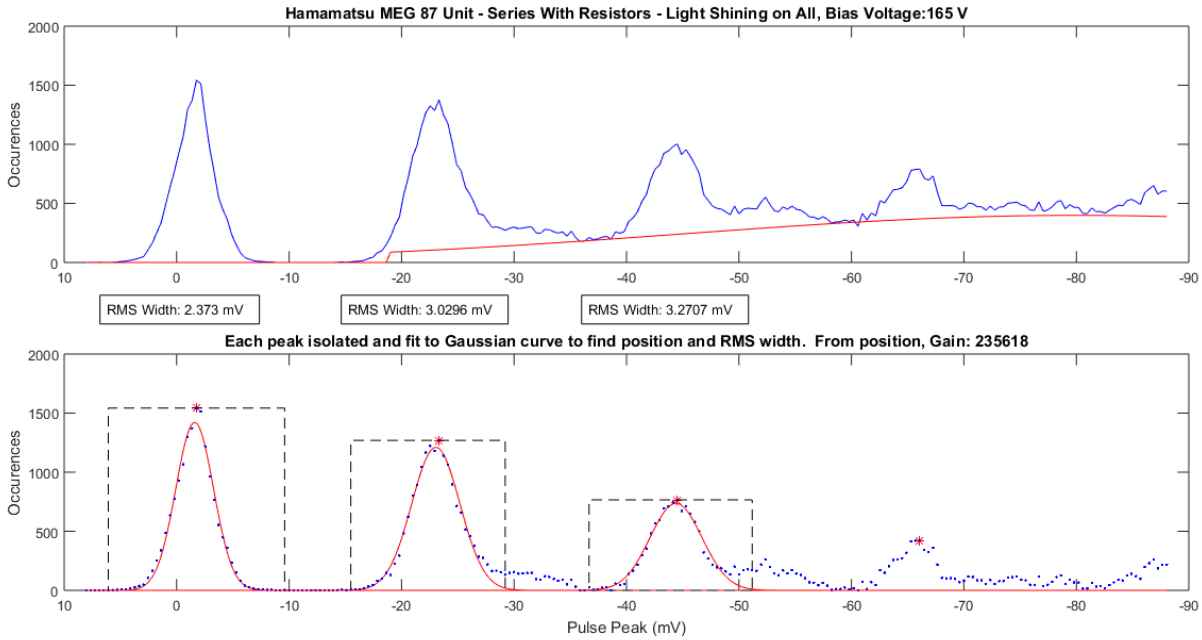

Figure 4.28: Example of pulsed light histogram analysis in MATLAB

the individual SiPM at the corresponding overvoltages. Three quadrants are connected in series, and histograms at the full range of voltages are taken with the light shining on all quadrants equally. The tests are repeated with the light shining on each quadrant in the array individually as well. These preliminary results are shown in Figure 4.29, where the gray line is the individual quadrant, the dotted line is the expected series gain values, and the other lines are series gains with various light configurations.

As can be seen, the cases in which light is shining on an individual quadrant resulted in a gain that is reduced more than expected, as opposed to the configuration where light is shining on all quadrants equally. Also, these reduced gain plots showed a distinct non-linearity that is not typical of a Gain/Bias Voltage relationship as described in Equation 2.8. To investigate this phenomenon, a Keithley 6517B High Resistance Meter with an input impedance of $>200T\Omega$ is connected across SiPMs in the array and the voltage drop across each of them is measured in-situ in the different light configurations. The effect is summarized in Figure 4.30.

It is noted that when light is shining only on one quadrant, the voltage drop across that quadrant decreased, and the voltage drops across the other quadrants increased to compensate. This led to a wide mismatch and resulted in the irregular gains seen. Through experimentation, it was realized that this effect is dependant on the rate of the light incident to the SiPMs. By utilizing a modified setup with an external pulser, as seen in Figure 4.31, it has been determined that the frequency of light pulses must be below 200 Hz for this effect to be negligible. The measurements are repeated, and all further data is taken with light shining at 50 Hz. This modification is appropriate for nEXO, as the event rate is expected to be even lower in the final experiment, however, if the series configuration were to be used

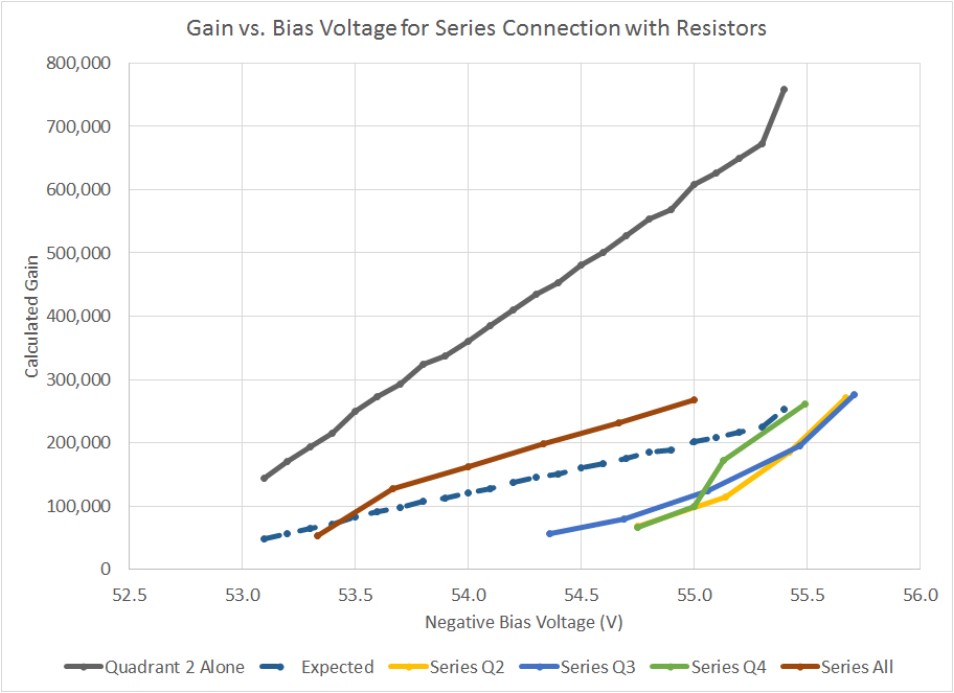

Figure 4.29: Initial gain vs. Bias results of Hamamatsu MEG unit with 10 kHz pulsing

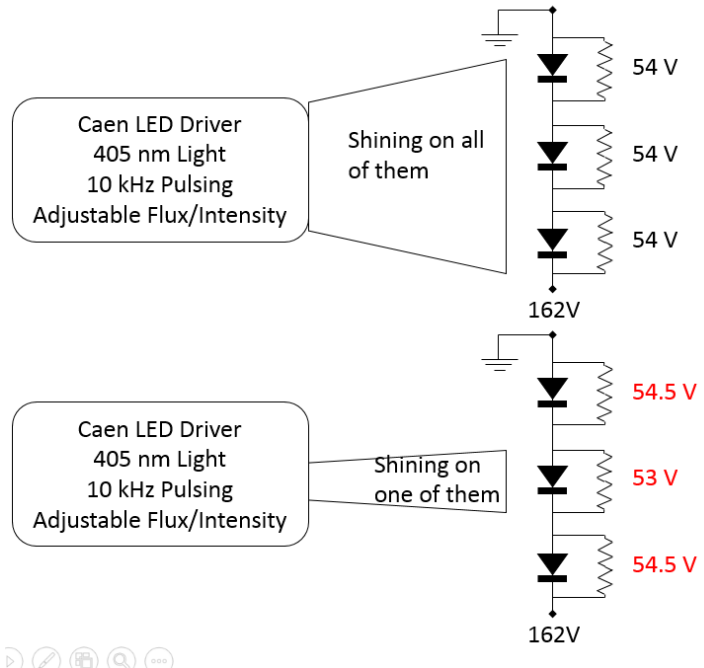

Figure 4.30: Diagram of the effect of light position on pulsed light measurements

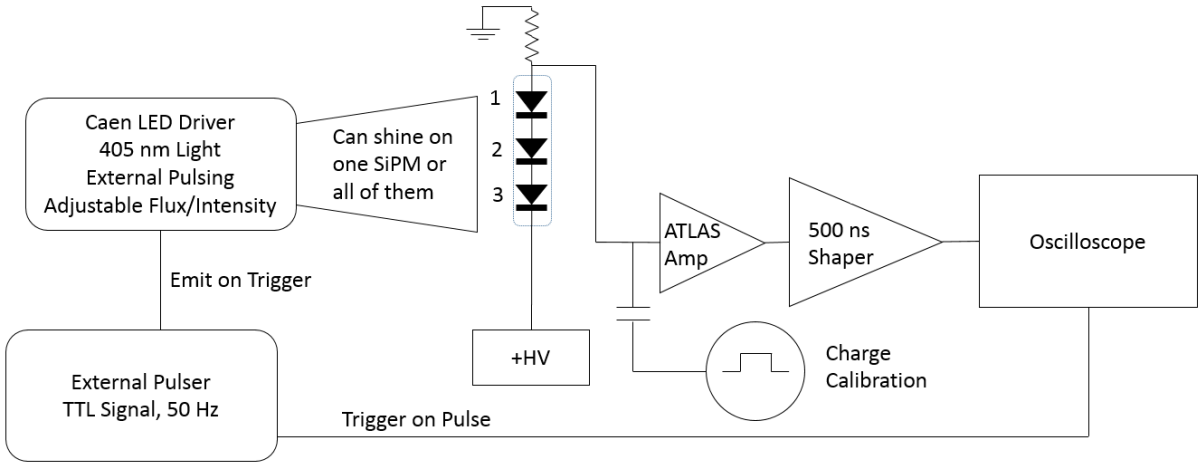

Figure 4.31: Updated schematic of test setup with external pulser driving the LED pulsing

in an application that had faster event rates and localized light, this would be an issue that would need to be dealt with.

The FBK NUV unit is also tested as a single SiPM, but histogram peaks could not be resolved with pulsed light, as the signal is excessively noisy. As seen in the unit's CV and IV curves, the behavior of the unit at 77K is outside the bounds of expected use for the SiPM. Combined with the reality that connecting multiple FBK SiPMs together in series or in parallel would be difficult, given the low quantity available and the lack of packaging, the testing of FBK units in series has been delayed until a new design from the manufacturer could be procured.

4.3.4 Final Results

4.3.4.1 Gain Analysis

With the LED Driver pulsing at 50 Hz, the Hamamatsu MEG Unit #87 is fully tested with its three individual quadrants, as well as with the series configuration. The full analyses of each configuration at each tested bias voltage are included in Appendix C. With each histogram, a final gain value is obtained. The plot of SiPM Gain as a function of Bias Voltage for the individual quadrants - 1, 2, and 3 - is seen in Figure 4.32. With the definition of Gain in Equation 2.8, it can be seen that by computing the slope and intercept of the Gain vs. Bias Voltage plots, the measured V_{BR} and C_J can be found. The inherent gain mismatch of the different quadrants can be calculated by comparing the gain values for a given bias voltage. In this case, it is around 8-9%, depending on the bais voltage.

While quadrants 1 and 2 are significantly better matched, it's quadrant 3 that contributes to the larger mismatch. Additional units would have to be tested to study if this is typical or not for these SiPMs. This mismatch can be seen to be due to the differences in both

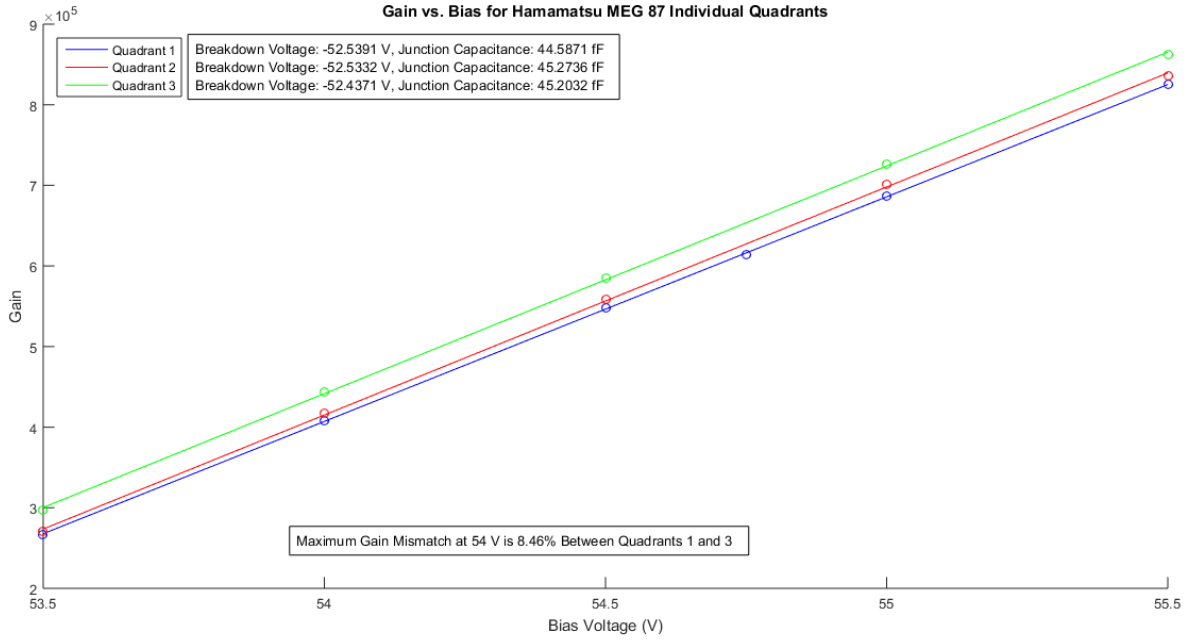

Figure 4.32: Gain vs. Bias voltage for individual quadrants on Hamamatsu MEG Unit #87

junction capacitance, C_J, which alters the slope of the plot, and V_{BR}, which alters the Y-intercept. Quadrants 1 and 2 can be seen to have a breakdown voltage within millivolts of each other, while Quadrant 3 has a V_{BR} that is ≈100 mV lower than the other two, explaining the consistently higher gain. One way to normalize this is to plot the gains as a function of overvoltage, $V_{OVq} = V_{BIAS} - V_{BRq}$, where V_{OVq} and V_{BRq} are the overvoltage and breakdown voltage for that specific quadrant. The "corrected" data for overvoltage can be seen in Figure 4.33.

This shows that when the differences in breakdown voltages are accounted for, which can be done by biasing a different quadrant with individually tuned voltages, the gain matching can improve. In this case, the gain mismatch of 1-2% represents the inherent differences due to manufacturing variabilities, such as slightly different junction capacitances. This it the benchmark for what ideal gain matching could be. The measured value for the average pixel's C_J is ≈45 fF, which is on the same order of magnitude of the 70 fF determined by the CV measurement, although the difference is likely due to the CV measurement including C_G, the grid capacitance.

The series connection is tested first with resistors. The resistors used are matched according to Table 4.1 at room temperature, although as can be seen, the resistance values are more unpredictable at cryogenic temperatures. These resistors are installed in parallel across the three SiPM quadrants and the Gain vs. Bias Voltage is measured again, with light shining both on each quadrant and on all of them. The results are shown in Figure 4.34. When light is directed at one quadrant, it is assumed that no light is incident on the others, which is confirmed to be accurate by measuring a quadrant in the individual configuration with light shining on another. This produces a Gain vs. Bias Voltage relationship indicative

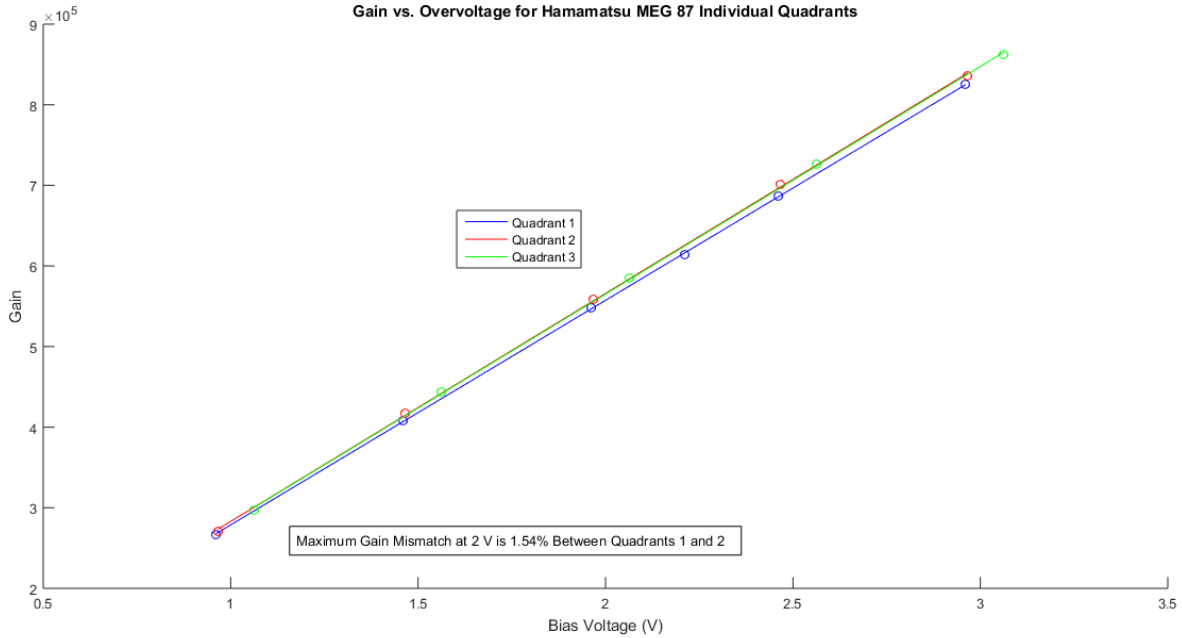

Figure 4.33: Gain vs. Overvoltage for individual quadrants on Hamamatsu MEG Unit #87

Resistor	**1**	**2**	**3**	**Max Difference**
Room Temperature	$995M\Omega$	$994M\Omega$	$992M\Omega$	0.30%
Liquid Nitrogen	$1070M\Omega$	$1038M\Omega$	$1053M\Omega$	1.61%
Percent Change	7.01%	4.24%	5.79%	

Table 4.1: Analysis of one firing pixel in an SiPM array

of what would happen if a photon is incident on one particular quadrant, as opposed to a steady flux incident on multiple quadrants in the array. Given the low expected event rate of the nEXO experiment, the gain mismatch with light incident on only one array is important to characterize.

As seen in the plot, the magnitude of the gain is reduced, as expected, and the gain matching has actually improved to $\simeq 4.5\%$. Interestingly enough, Quadrant 3, which previously had the consistently higher gain, is now well matched with Quadrant 2, leaving Quadrant 1 as the outlier which increases the gain mismatch. The reason for this can be found through a measurement of the bias across each quadrant for a given total array bias voltage, as seen in Figure 4.35. A high impedance voltmeter was used to measure the voltage drop across each quadrant. The results show that Quadrant 3, which previously had a consistently higher gain when measured individually, had a biasing resistor that gave it a

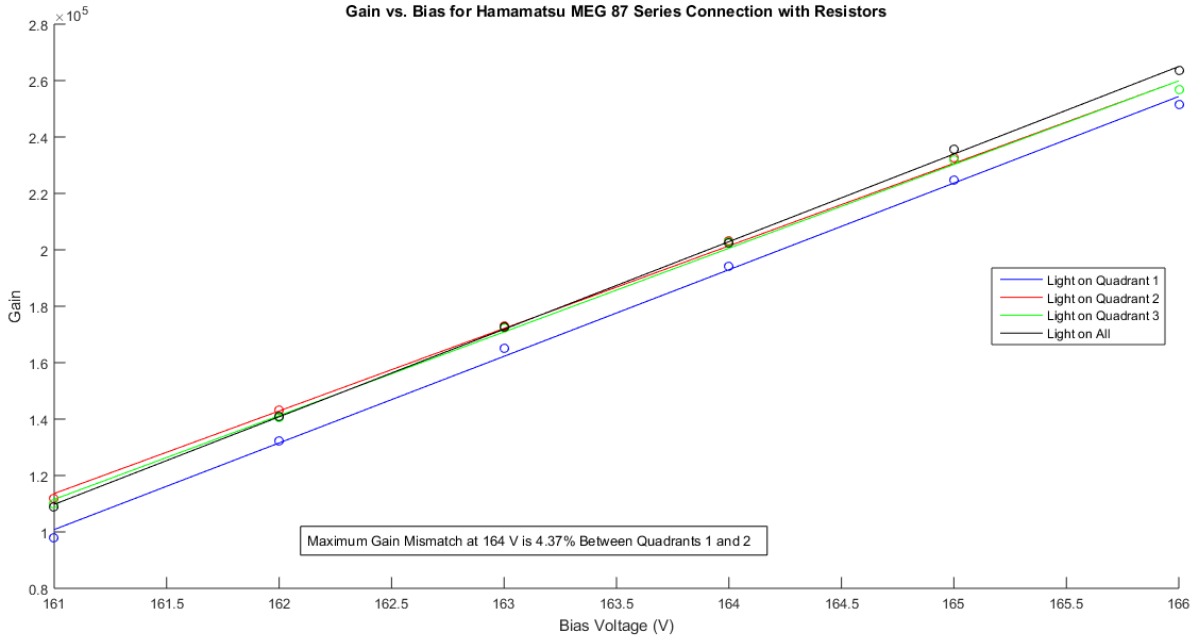

Figure 4.34: Gain vs. Bias voltage for series configuration on Hamamatsu MEG Unit #87

lower voltage drop than Quadrant 2, which would have the effect of matching their gains more closely. Quadrant 1, which has roughly the same gain as Quadrant 2 when measured individually, had a biasing resistor that applied a lower voltage across it, leading to the consistently lower gain seen in Figure 4.34.

This shows that in principle, the mismatch in resistors could be used to compensate for the inherent mismatches in the series SiPM array self-biasing, and actually improve the total gain mismatch to be closer to the ideal value. For nEXO however, individual resistor matching to specific SiPMs is not being considered, due to the logistical difficulty of implementing this on the large number of SiPMs expected to cover the 4 m^2 of light sensistive area. As a comparison, the series connection is also tested with no resistors. However, it is difficult to resolve the peaks from the data, as the gain appeared to be excessively noisy, as seen in Figure 4.36. The confirm this, the individual quadrant voltage drops are measured for the series configuration with no resistors, seen in Figure 4.37. The voltage drops are significantly mismatched, as well as unstable, as seen by the error bars. For the Hamamatsu MEG units, it appears that the differences in leakage currents lead to unpredictable voltage drops when connected in series without resistors.

As a comparison, the magnitude of the gains for the SiPM quadrants in both single and series configurations are shown in Figure 4.38. The gain plot of Quadrant 1 is used as a benchmark, with the theoretical voltage reduction of $\frac{1}{3}$ marked as a dotted line. The series gain is represented by the configuration with light shining on all quadrants, with the bias voltage divided by 3. As can be seen, the resulting series gain matches the theoretical predition within 4%.

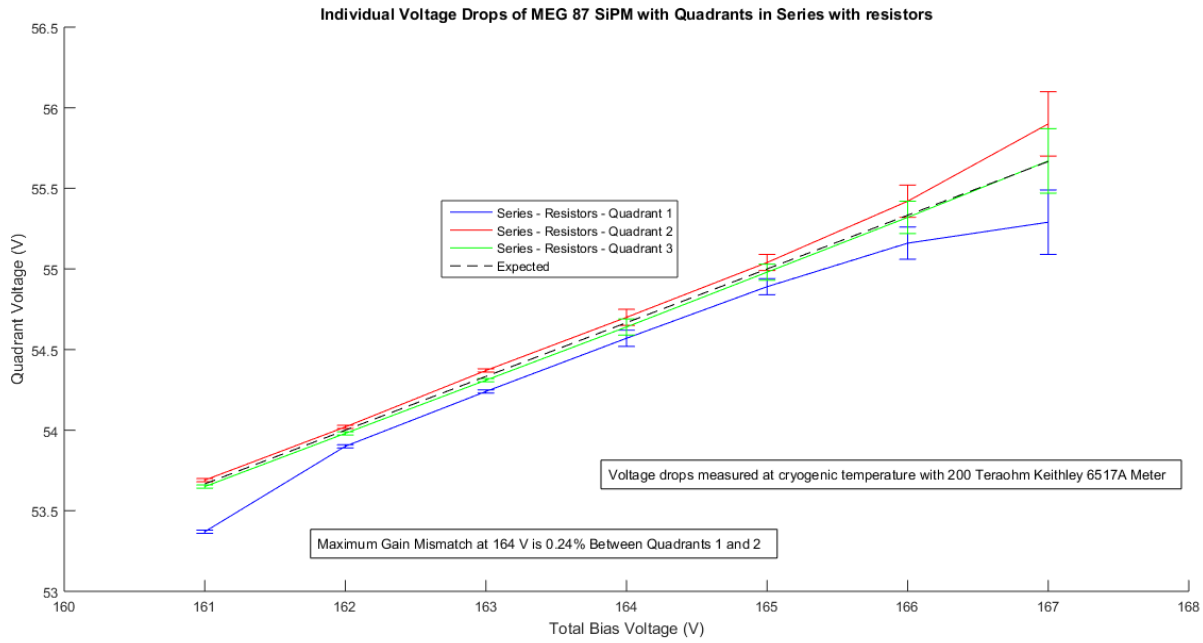

Figure 4.35: Quadrant bias voltage vs. Array bias voltage for series configuration with resistors on Hamamatsu MEG Unit #87

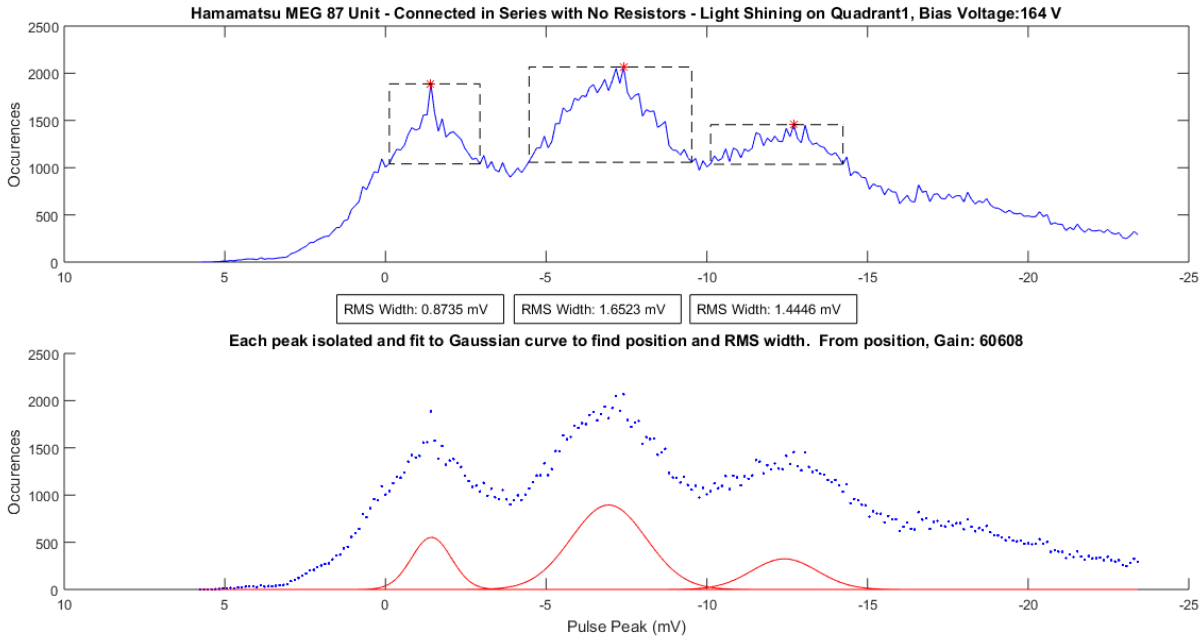

Figure 4.36: Noisy histogram for series connection with no resistors on Hamamatsu MEG Unit #87

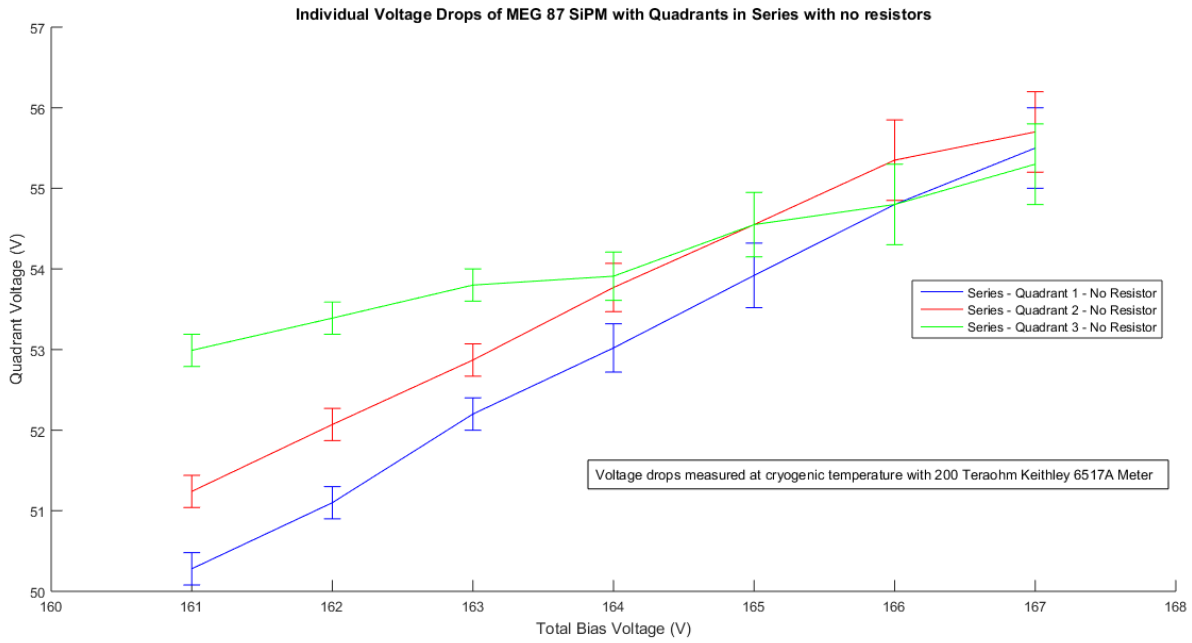

Figure 4.37: Quadrant bias voltage vs. Array bias voltage for series configuration with no resistors on Hamamatsu MEG Unit #87

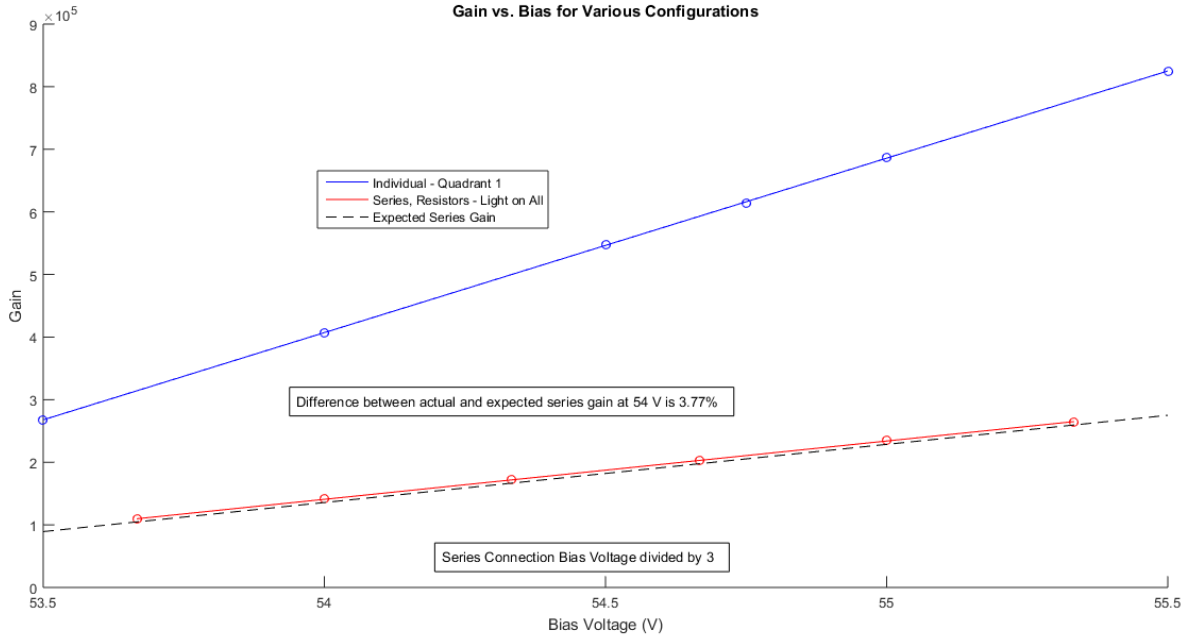

Figure 4.38: Gain vs. Normalized bias voltage for individual and series configurations on Hamamatsu MEG Unit #87

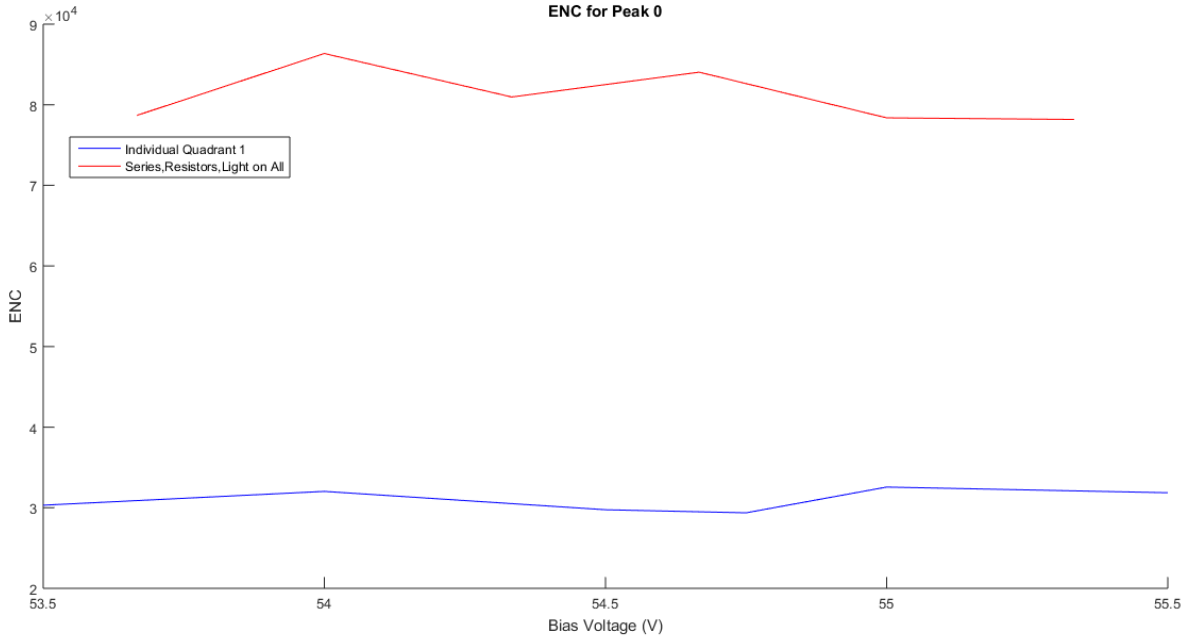

Figure 4.39: Pulsed light histogram for Hamamatsu MEG Unit #87 Quadrant 1, biased at 54.75 V

4.3.4.2 Noise Analysis

As explained in Section 4.3.2, the ENC for each peak can be calculated using Equation 4.2. Using the described method, the ENC can be compared betweeen two configurations, as in Figure 4.39, which shows the 0 p.e. peak. As can be seen, the ENC for the series connection is unexpectedly higher compared to the individual quadrant. This can be confirmed visually by comparing Figure 4.40, a typical histogram results from an individual quadrant and Figure 4.41, a typical histogram result from the series configuration. While the magnitude of the peak width is less in the series case, when compared to the reduced peak spacing, the noise behavior is actually worse.

This can be explained by a careful analysis of the amplifier. The amplifier used, as described in Section 4.3.1, is designed for a sensor with a much faster event rate, and had additional considerations, such as the need for a feedback loop to stabilize the input impedance. The unique demands of the ATLAS experiment led to a design with a parallel noise spectral density of $6.8\frac{pA}{\sqrt{Hz}}$ and a series noise spectral density, $0.35\frac{nV}{\sqrt{Hz}}$, which are well matched, considering the parameters of the experiment. For example, for the peaking time used in the ATLAS experiment, 20 ns, and the shaping type, a bipolar shaper that gives $A_S \approx 4$ and $A_P \approx \frac{4}{3}$, the ENC contributions are as follow:

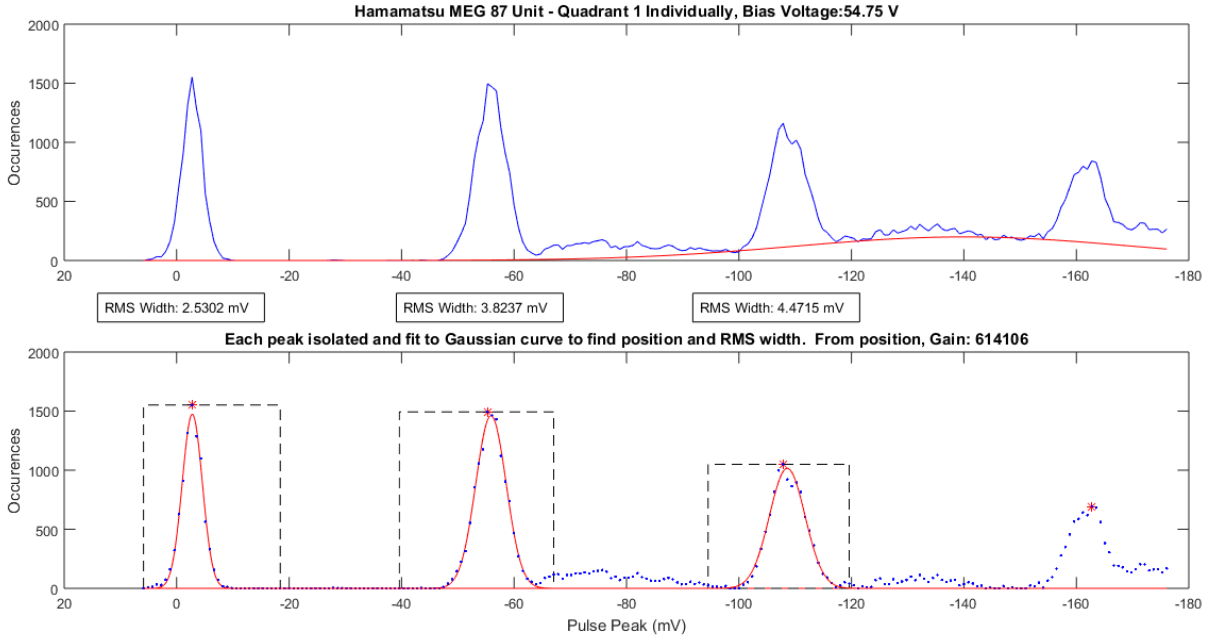

Figure 4.40: Pulsed light histogram for Hamamatsu MEG Unit #87 Quadrant 1, biased at 54.75 V

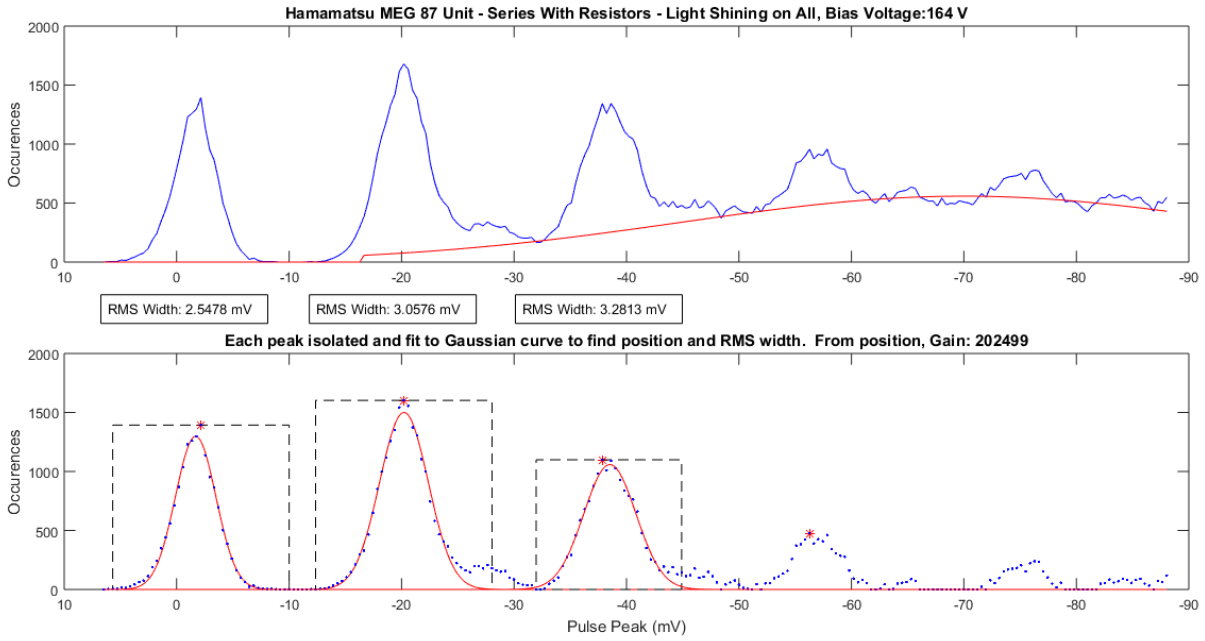

Figure 4.41: Pulsed light histogram for Hamamatsu MEG Unit #87 series SiPM configuration with resistors, biased at 164V

$$
\begin{aligned}
ENC &= \frac{1}{q}\sqrt{{e_n}^2\ (C_D + C_{IN})^2\ \frac{A_S}{t_p} + {i_n}^2\ t_p\ A_P} \\
&= \frac{1}{q}\sqrt{(0.35\frac{nV}{\sqrt{Hz}})^2\ (1nF)^2\ \frac{4}{20ns} + \frac{4}{3}\ (6.8\frac{pA}{\sqrt{Hz}})^2\ 20ns} \\
&= \frac{1}{q}\sqrt{2.45 \times 10^{-29}\,\mathrm{C}^2 + 1.23 \times 10^{-30}\,\mathrm{C}^2}
\end{aligned}
$$

It can be seen that with a peaking time of 20 ns, the contributions of series and parallel noise in square Coulombs are fairly well matched, and thus result in close to a minimum ENC. For the peaking time used in the SiPM measurements, 400 ns, and the semigaussian unipolar shaper that gives $A_S \approx 1.85$ and $A_P \approx 1.85$ instead we have:

$$
\begin{aligned}
ENC &= \frac{1}{q}\sqrt{{e_n}^2\ (C_D + C_{IN})^2\ \frac{A_S}{t_p} + {i_n}^2\ t_p\ A_P} \\
&= \frac{1}{q}\sqrt{(0.35\frac{nV}{\sqrt{Hz}})^2\ (1nF)^2\ \frac{1.85}{400ns} + 1.85 *\ (6.8\frac{pA}{\sqrt{Hz}})^2\ 400ns} \\
&= \frac{1}{q}\sqrt{5.67 \times 10^{-31}\,\mathrm{C}^2 + 3.42 \times 10^{-29}\,\mathrm{C}^2}
\end{aligned}
$$

In this case, the parallel noise contribution is two orders of magnitude greater than the series noise. This is critical to the noise performance of the series connection, as the expression for ENC can be normalized to the "Equivalent Noise Photon", which takes into account the gain of the sensor, as in Equation 4.3, assuming C_{IN} is insignificant compared to C_D and where G is the sensor configuration's gain.

$$
ENP = \frac{1}{q}\sqrt{\frac{1}{G^2}\ {e_n}^2\ (C_D)^2\ \frac{A_S}{t_p} + \frac{1}{G^2}\ {i_n}^2\ t_p\ A_P} \tag{4.3}
$$

In the case of the series connection of three SiPMs, the ENP is thus:

$$
\begin{aligned}
ENP &= \frac{1}{q}\sqrt{\left(\frac{1}{\frac{G}{3}}\right)^2 {e_n}^2 \left(\frac{C_D}{3}\right)^2 \frac{A_S}{t_p} + \left(\frac{1}{\frac{G}{3}}\right)^2 {i_n}^2 \, t_p \, A_P} \\
&= \frac{1}{q}\sqrt{\frac{9}{G^2} \, {e_n}^2 \left(\frac{{C_D}^2}{9}\right) \frac{A_S}{t_p} + \frac{9}{G^2} \, {i_n}^2 \, t_p \, A_P} \\
&= \frac{1}{q}\sqrt{\frac{\cancel{9}}{G^2} \, {e_n}^2 \left(\frac{{C_D}^2}{\cancel{9}}\right) \frac{A_S}{t_p} + \frac{9}{G^2} \, {i_n}^2 \, t_p \, A_P} \\
&= \frac{1}{G} \, \frac{1}{q}\sqrt{{e_n}^2 \left({C_D}^2\right) \frac{A_S}{t_p} + 9 \, {i_n}^2 \, t_p \, A_P}
\end{aligned}
$$

It can be seen that the reduction in sensor capacitance helps reduce the series noise component as compared to the parallel connection, which would have increased the detector capacitance by $n * C_D$, as the G term remains the same. However, the tradeoff of this is that the parallel noise contribution is increased by n^2. This can be mitigated by using an amplifier with minimal parallel noise, so that the series connection improves the total noise. However, with the available amplifier and shaper that were used, the parallel noise dominated the system, which means that the series connection led to further parallel noise contribution over the total noise response of the amplifier. However even in this non-optimized configuration, each photo-electron peak is still clearly resolved as seen in Figure 4.41.

4.4 Conclusions

The pulsed light test measurements, which are the most indicative of the behavior of SiPMs being used in the final nEXO experiment, showed that the series connection of SiPMs can be achieved at cryogenic temperature. Further investigation showed that for the Hamamatsu MEG unit tested, the leakage currents varied too much to provide an equal voltage drop for each SiPM in the series configuration. Resistors were then used to equalize the voltage drops, and worked well for gain matching. With regards to noise, due to availability, the amplifier and shaping time used were not indicative of an amplifier tuned for use with this SiPM. Therefore, the noise response of the SiPM array in series did not show a better noise resolution.

4.5 Future Work

Moving forward, an amplifier optimized for SiPM readout will be designed and assembled for further testing. When the pulsed light measurements are repeated with this amplifier,

experimental data is expected to show the series configuration ENC that is anticipated from theoretical predictions. Additional SiPMs from various manufacturers will also be procured in order to confirm the dark current and gain mismatches seen in the Hamamatsu MEG units. Also, improved fixturing for an increased number of SiPMs will be designed in order to measure the properties of arrays such as those seen in Figure 3.14.

Bibliography

About EXO-200 (2015). URL: https://www-project.slac.stanford.edu/exo/about.html.

An Introduction to the Silicon Photomultiplier. URL: http://www.sensl.com/downloads/ds/TN%20-%20Intro%20to%20SPM%20Tech.pdf.

Avignone, F., S. Elliot, and J. Engel (2008). "Double beta deca, Majorana neutrinos, and neutrino mass". In: *Review of Modern Physics* 80, pp. 481–516. URL: https://user.physics.unc.edu/~engelj/papers/aee.pdf.

Buzhan, P. et al. (2001). "An Advanced Study of Silicon Photomultiplier". In: *ICFA Instrumentation Bulletin* 23, pp. 28–41. URL: http://www.slac.stanford.edu/pubs/icfa/fall01/paper3/paper3.pdf.

Buzhan, P. et al. (2009). "The Cross-talk Problem in SiPMs and Their Use as Light Sensors for Imaging Atmospheric Cherenkov Telescopes". In: *Nuclear Instruments and Methods in Physics Research* A 610, pp. 131–134. URL: http://www.sciencedirect.com/science/article/pii/S0168900209010456.

Collazuol, G. *SiPM Behavior at Low Temperatures*. Tech. rep. URL: http://collazug.home.cern.ch/collazug/iprd10_sipm_low_T.pdf.

— (2012). *The SiPM Physics and Technology - a Review*. Tech. rep. URL: https://indico.cern.ch/event/164917/contribution/72/attachments/198512/278663/PhotoDet12_-_collazuol_-_v3.pdf.

Corsi, F. et al. (2006). "Electrical Characterization of Silicon Photo-Multiplier Detectors for Optimal Front-End Design". In: *2006 IEEE Nuclear Science Symposium Conference Record*. URL: http://ieeexplore.ieee.org/stamp/stamp.jsp?arnumber=4179230.

De Geronimo, Gianluigi (2014). "Advanced Design of Low Noise, Low Power Analog Circuits". University Lecture.

Gratta, G. (2014). *EXO-200 and nEXO*. Tech. rep. Stanford University. URL: https://agenda.infn.it/getFile.py/access?resId=0&materialId=slides&confId=7584.

Haitz, Roland H. (1964). "Model for the Electrical Behavior of a Microplasma". In: *Journal of Applied Physics* 35. URL: http://scitation.aip.org/content/aip/journal/jap/35/5/10.1063/1.1713636.

Johnson, Tessa (2013). *How Does nEXO Work?* URL: https://nexo.llnl.gov/content/assets/docs/HowDoesnEXOWork_Final_Print.pdf.

Lauscher, Markus et al. *Silicon Photomultiplier (SiPM) Characterization for Fluorescence Light Detection*. Tech. rep. URL: http://www1b.physik.rwth-aachen.de/~kolleg/fileadmin/data/gk/de/badhonnef/2011/20110908_lauscher.pdf.

Marano, D. et al. (2014). "Silicon Photomultipliers Electrical Model Extensive Analytical Analysis". In: *IEEE Transactions on Nuclear Science* 61. URL: http://ieeexplore.ieee.org/xpls/abs_all.jsp?arnumber=6661445.

Otte, N. *Silicon Photomultipliers a new device for frontier detectors in HEP, astroparticle physics, nuclear medical and industrial applications*. Tech. rep. Max Planck Institute for Physics. URL: http://www.slac.stanford.edu/econf/C0604032/talks/snic_otte.pdf.

— *The Silicon Photomultiplier - A new device for High Energy Physics, Astroparticle Physics, Industrial and Medical Applications*. Tech. rep. Max Planck Institute for Physics. URL: http://www.slac.stanford.edu/econf/C0604032/papers/0018.pdf.

Para, Adam (2009). "Characterization of MPPC/SiPM/GMAPDs". URL: http://www-ppd.fnal.gov/DivOffice/internal_rd/Reviews_files/SIPM_2008/Characterization_of_MPPC.pdf.

— (2015). *Afterpulsing in Silicon Photomultipliers: Impact on the Photodetectors Characterization*. Tech. rep. Fermi National Accelerator Laboratory. URL: http://arxiv.org/abs/1503.01525.

Piatek, Slawomir S. (2014a). *Measuring the Electrical and Optical Properties of an MPPC*. URL: http://www.hamamatsu.com/jp/en/community/silicon_photomultipliers/tutorials/measuring_mppc/index.html.

— (2014b). *Physics and Operation of an MPPC*. URL: http://www.hamamatsu.com/jp/en/community/silicon_photomultipliers/tutorials/physics_of_mppc/index.html.

Rescia, S. et al. (2016). "nEXO SiPMs Series/Parallel Connection".

Rescia, Sergio. "ATLAS Calorimeter Documentation".

Seifert, Stefan et al. (2009). "Simulation of Silicon Photomultiplier Signals". In: *IEEE Transactions on Nuclear Science* 56. URL: http://ieeexplore.ieee.org/xpls/abs_all.jsp?arnumber=5341428.

SP5650 Sensor Holder for SP5600 SiPM Kit Data Sheet (2011). DS2628. Rev. n.0. Caen. URL: http://www.caen.it/jsp/Template2/CaenProd.jsp?parent=10&idmod=653.

Wangerin, Kristen A. et al. *Passive Electrical Model of Silicon Photomultipliers*. Tech. rep. URL: http://homepages.rpi.edu/~danony/Papers/2008/PassiveElectricalModelofSiliconPhotomultipliers.pdf.

Westerdale, Shawn (2010). *Neutrino Mass Problem: Masses and Oscillations*. URL: http://web.mit.edu/shawest/Public/8.06/termPaperDraft.pdf.

Willis, W.J. and Veljko Radeka (1974). "Liquid-Argon Ionization Chambers as Total-Absorption Detectors". In: *Nuclear Instruments and Methods* 120, pp. 221–236. URL: http://www.sciencedirect.com/science/article/pii/0029554X74900391.

Appendix A

Hamamatsu MEG 87 Unit DC Analysis Results

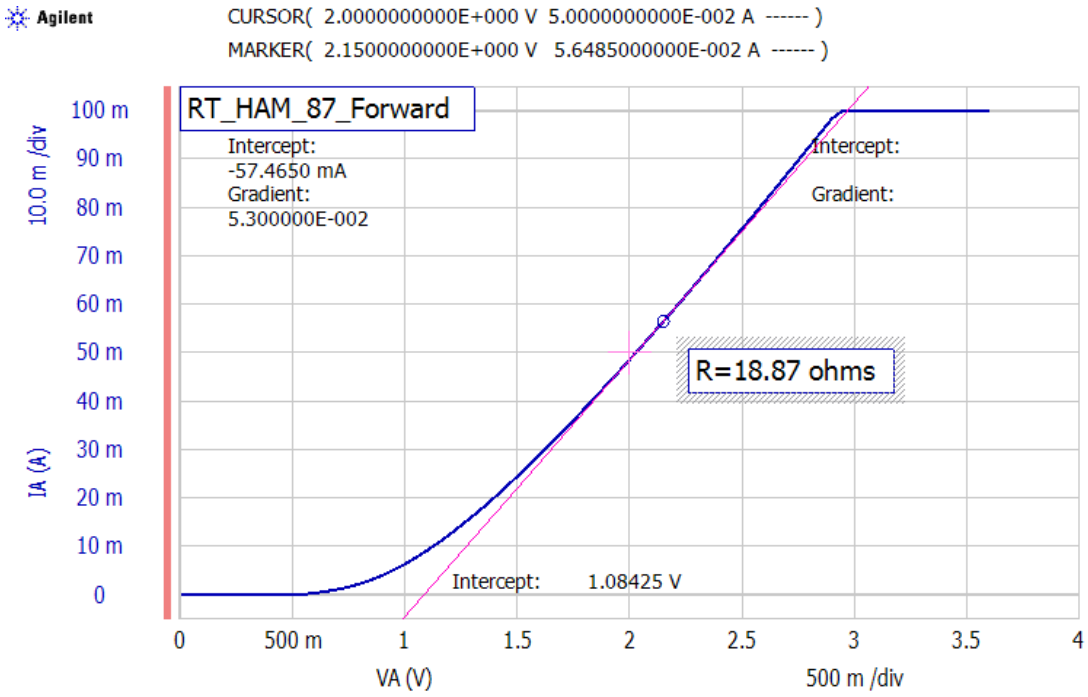

Figure A.1: Hamamatsu MEG Unit 87, Quadrant 1, Forward IV Curve - Room Temperature

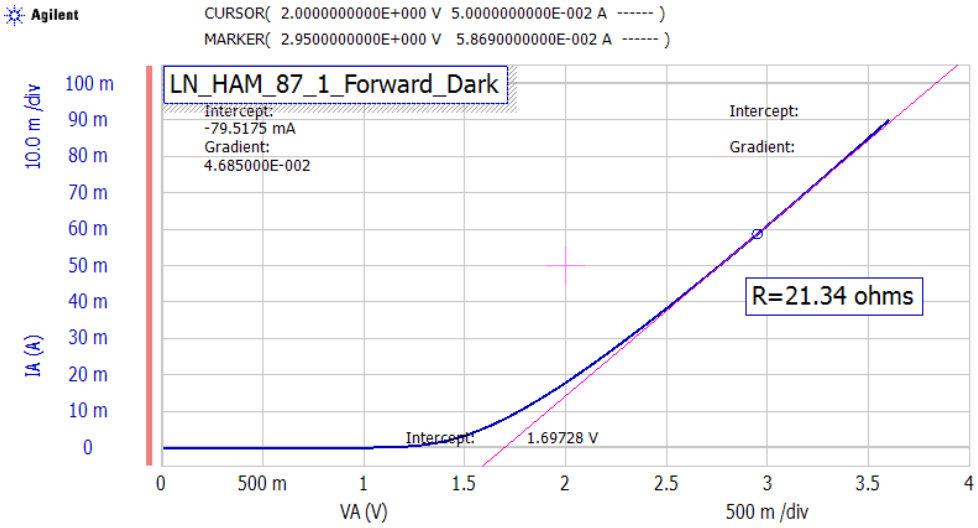

Figure A.2: Hamamatsu MEG Unit 87, Quadrant 1, Forward IV Curve - Liquid Nitrogen

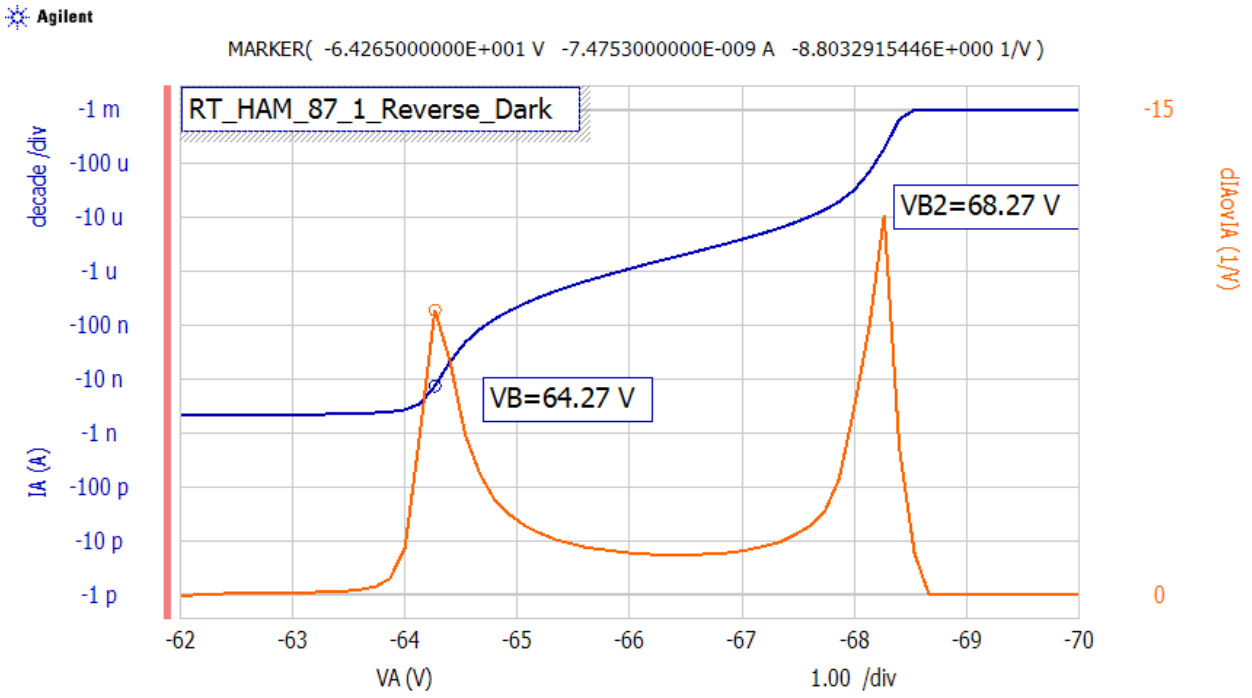

Figure A.3: Hamamatsu MEG Unit 87, Quadrant 1, Reverse IV Curve - Room Temperature
Blue Line - Current (A) Orange - Normalized Derivative of Current

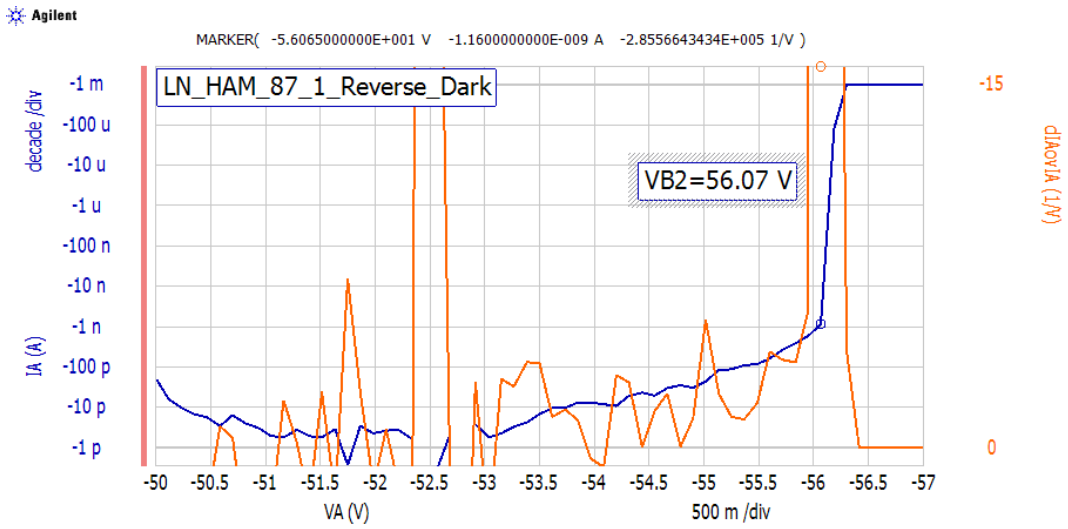

Figure A.4: Hamamatsu MEG Unit 87, Quadrant 1, Reverse IV Curve - Liquid Nitrogen, Dark
Blue Line - Current (A) Orange - Normalized Derivative of Current

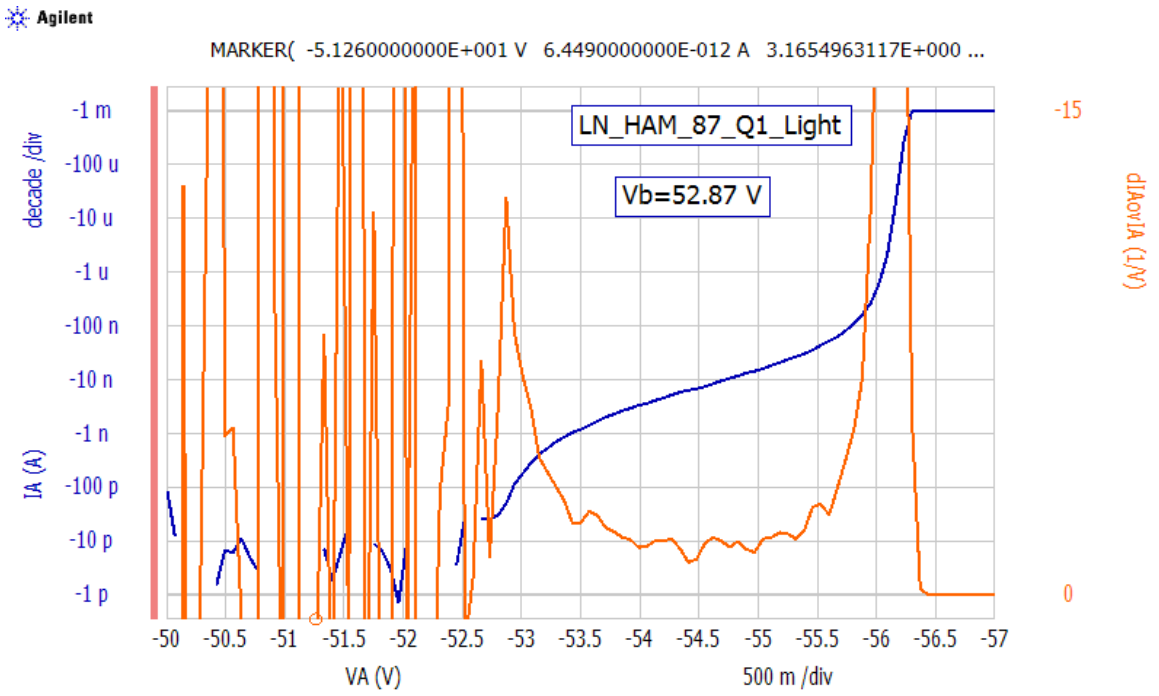

Figure A.5: Hamamatsu MEG Unit 87, Quadrant 1, Reverse IV Curve - Liquid Nitrogen, Some Light
Blue Line - Current (A) Orange - Normalized Derivative of Current

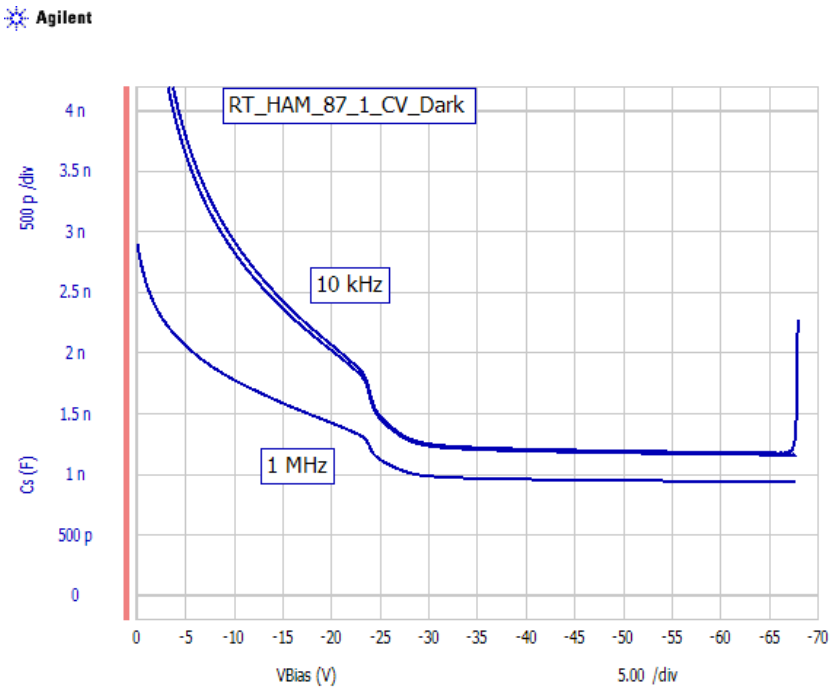

Figure A.6: Hamamatsu MEG Unit 87, Quadrant 1, Reverse CV Curve - Room Temperature

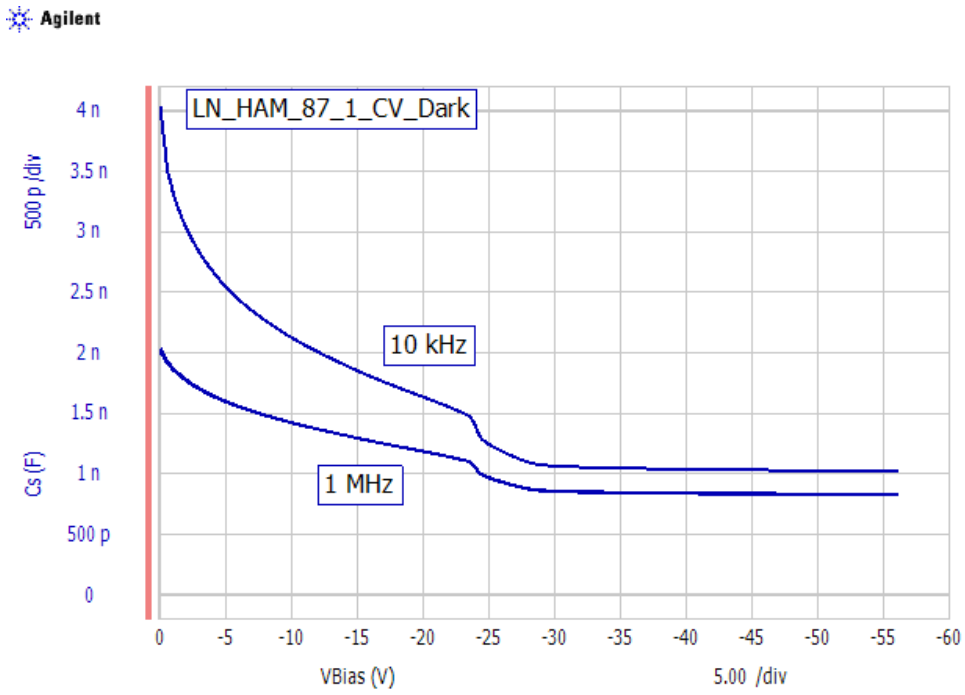

Figure A.7: Hamamatsu MEG Unit 87, Quadrant 1, Reverse CV Curve - Liquid Nitrogen

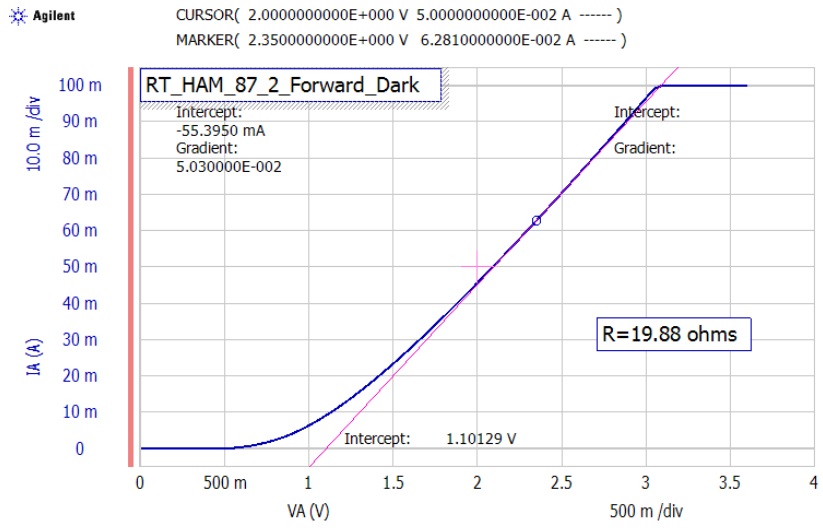

Figure A.8: Hamamatsu MEG Unit 87, Quadrant 2, Forward IV Curve - Room Temperature

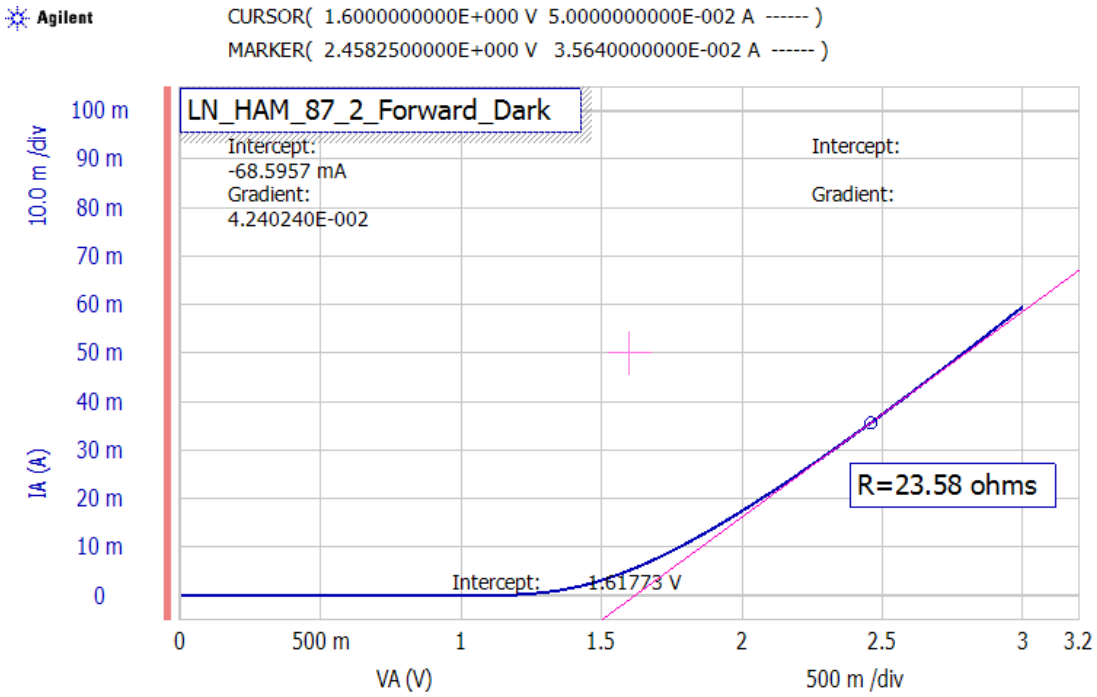

Figure A.9: Hamamatsu MEG Unit 87, Quadrant 2, Forward IV Curve - Liquid Nitrogen

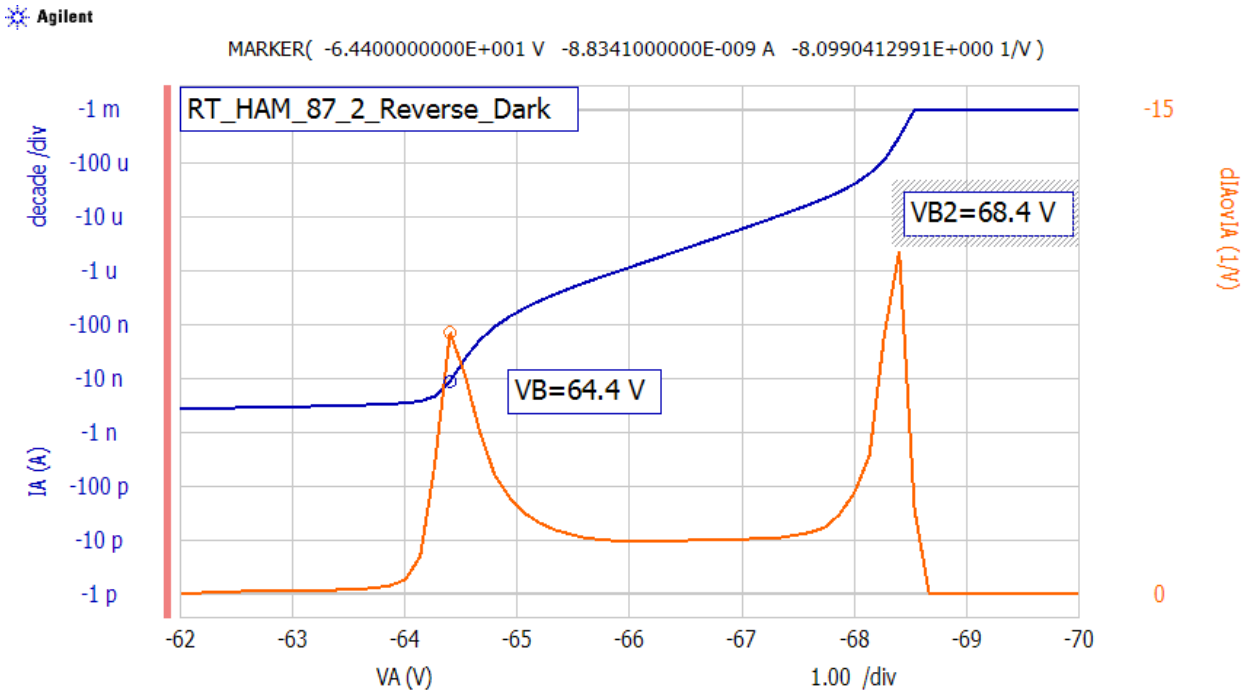

Figure A.10: Hamamatsu MEG Unit 87, Quadrant 2, Reverse IV Curve - Room Temperature
Blue Line - Current (A) Orange - Normalized Derivative of Current

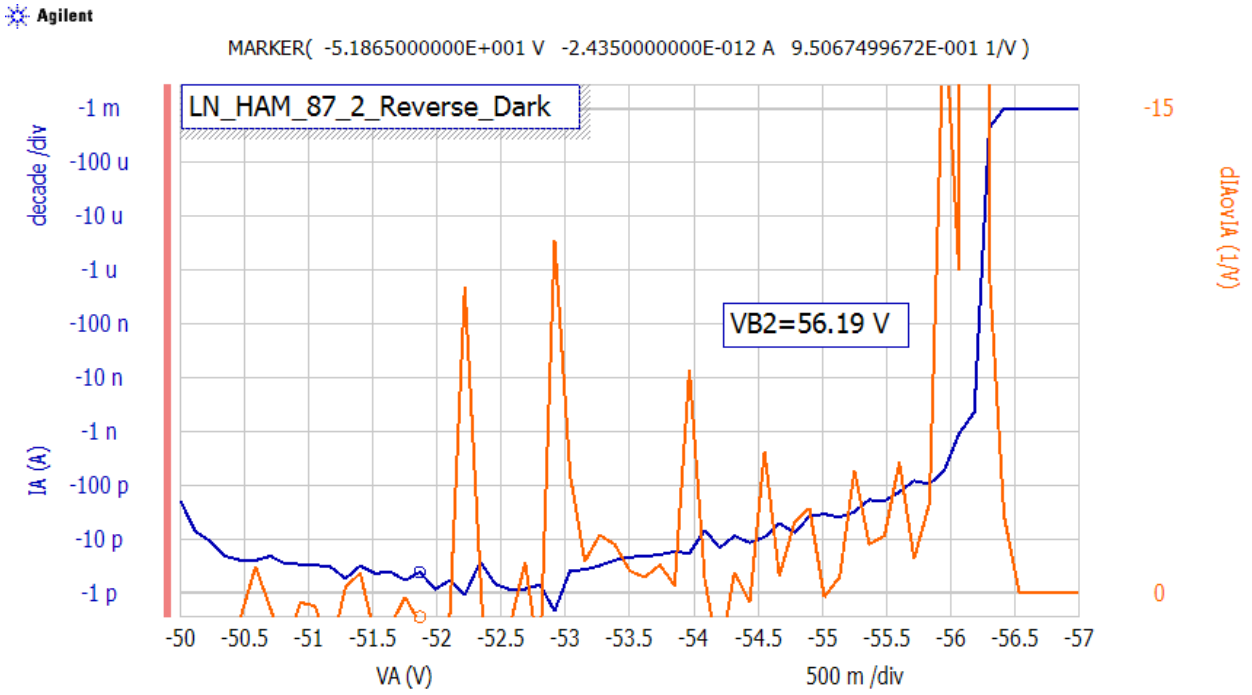

Figure A.11: Hamamatsu MEG Unit 87, Quadrant 2, Reverse IV Curve - Liquid Nitrogen, Dark

Blue Line - Current (A) Orange - Normalized Derivative of Current

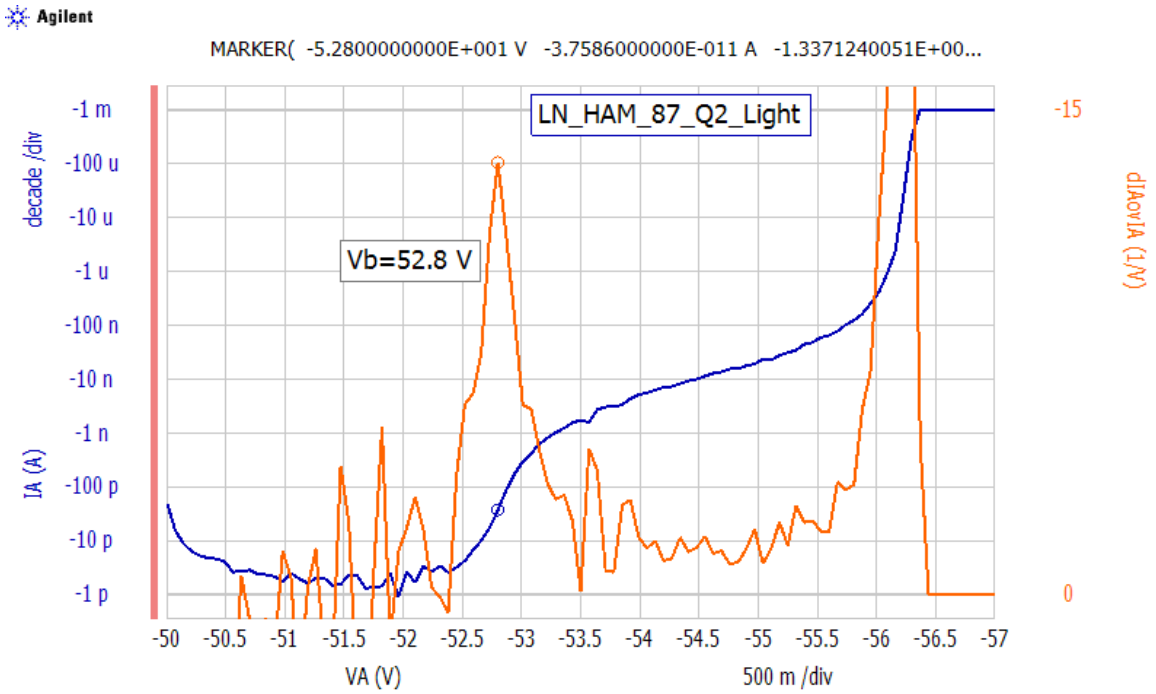

Figure A.12: Hamamatsu MEG Unit 87, Quadrant 2, Reverse IV Curve - Liquid Nitrogen, Some Light

Blue Line - Current (A) Orange - Normalized Derivative of Current

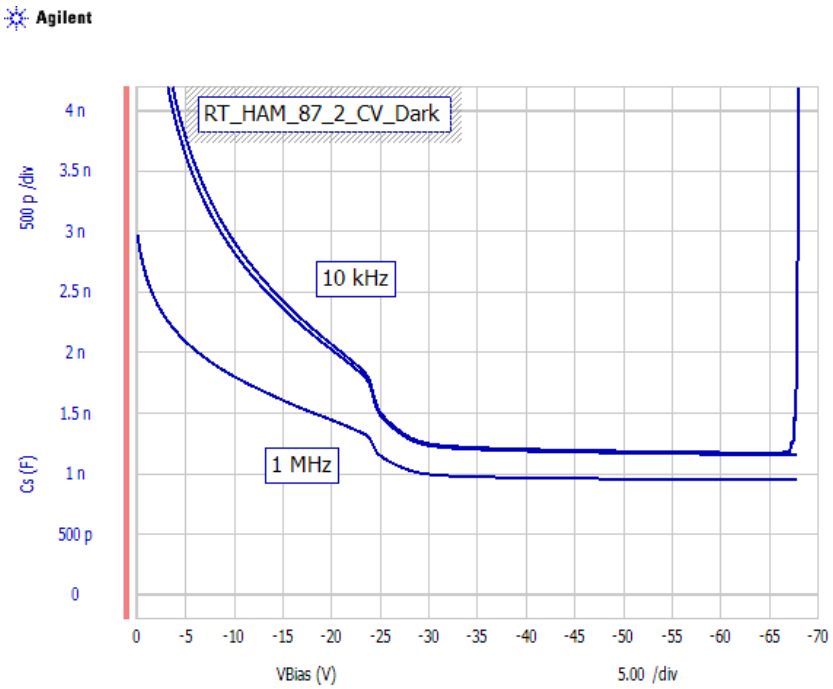

Figure A.13: Hamamatsu MEG Unit 87, Quadrant 2, Reverse CV Curve - Room Temperature

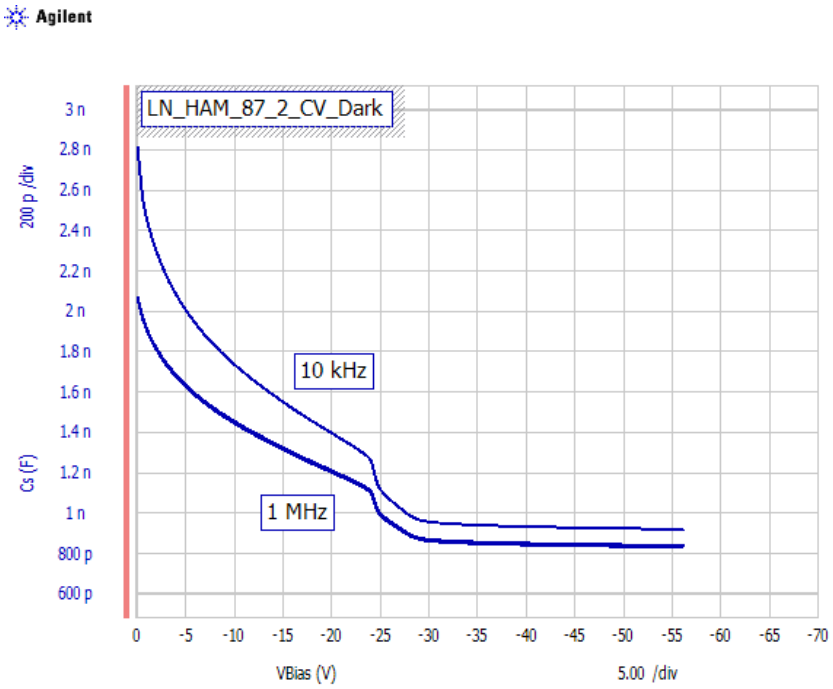

Figure A.14: Hamamatsu MEG Unit 87, Quadrant 2, Reverse CV Curve - Liquid Nitrogen

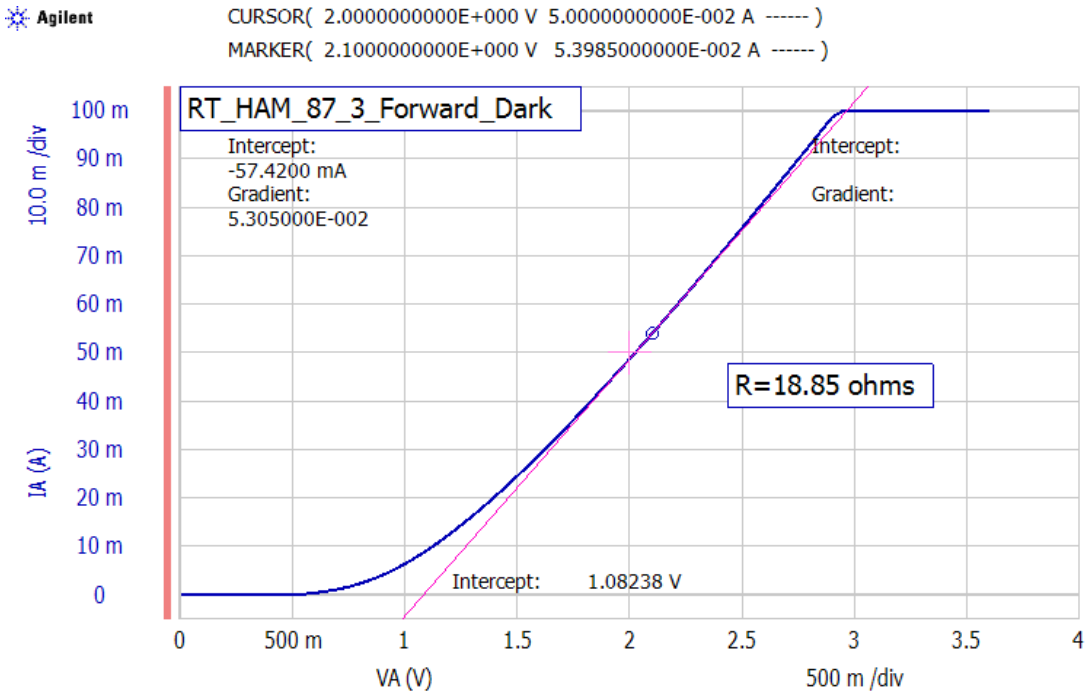

Figure A.15: Hamamatsu MEG Unit 87, Quadrant 3, Forward IV Curve - Room Temperature

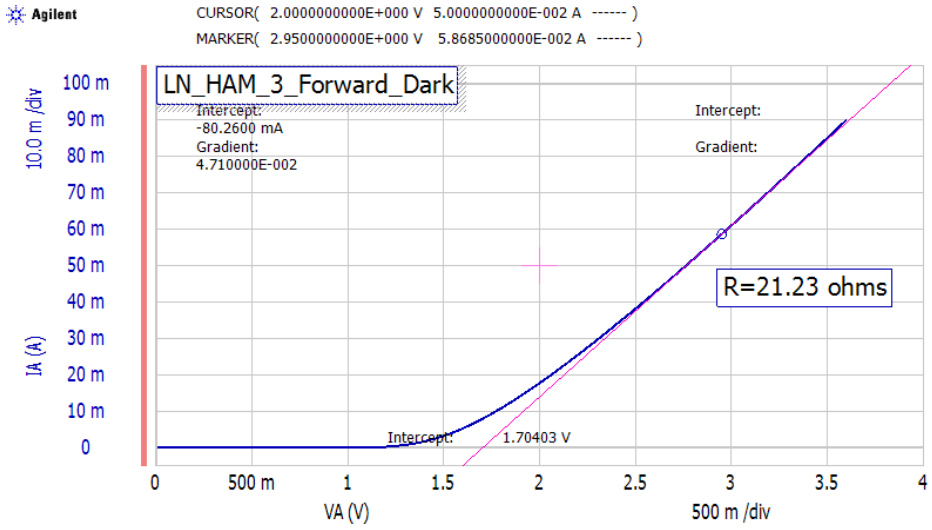

Figure A.16: Hamamatsu MEG Unit 87, Quadrant 3, Forward IV Curve - Liquid Nitrogen

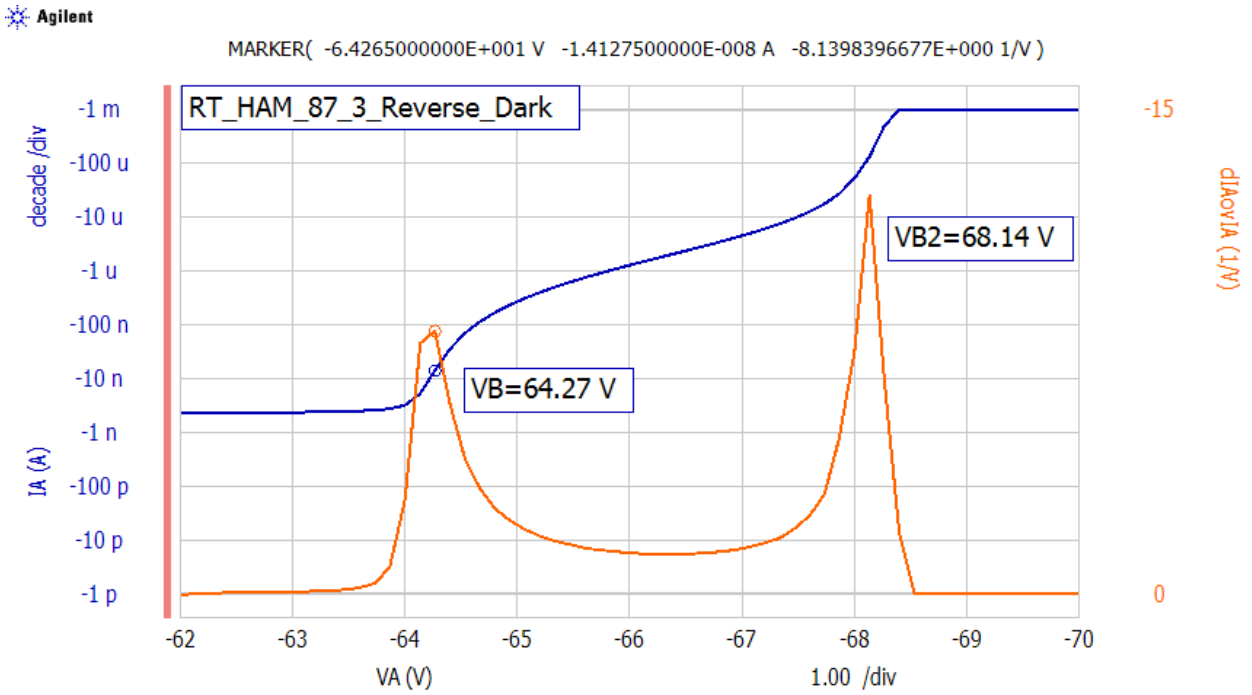

Figure A.17: Hamamatsu MEG Unit 87, Quadrant 3, Reverse IV Curve - Room Temperature
Blue Line - Current (A) Orange - Normalized Derivative of Current

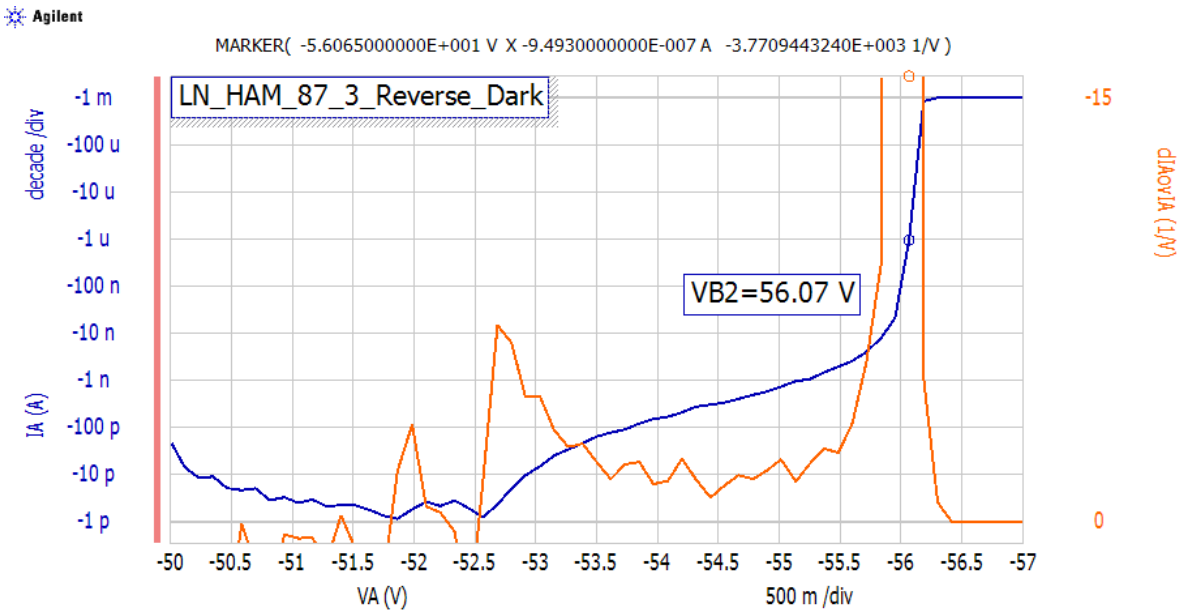

Figure A.18: Hamamatsu MEG Unit 87, Quadrant 3, Reverse IV Curve - Liquid Nitrogen, Dark
Blue Line - Current (A) Orange - Normalized Derivative of Current

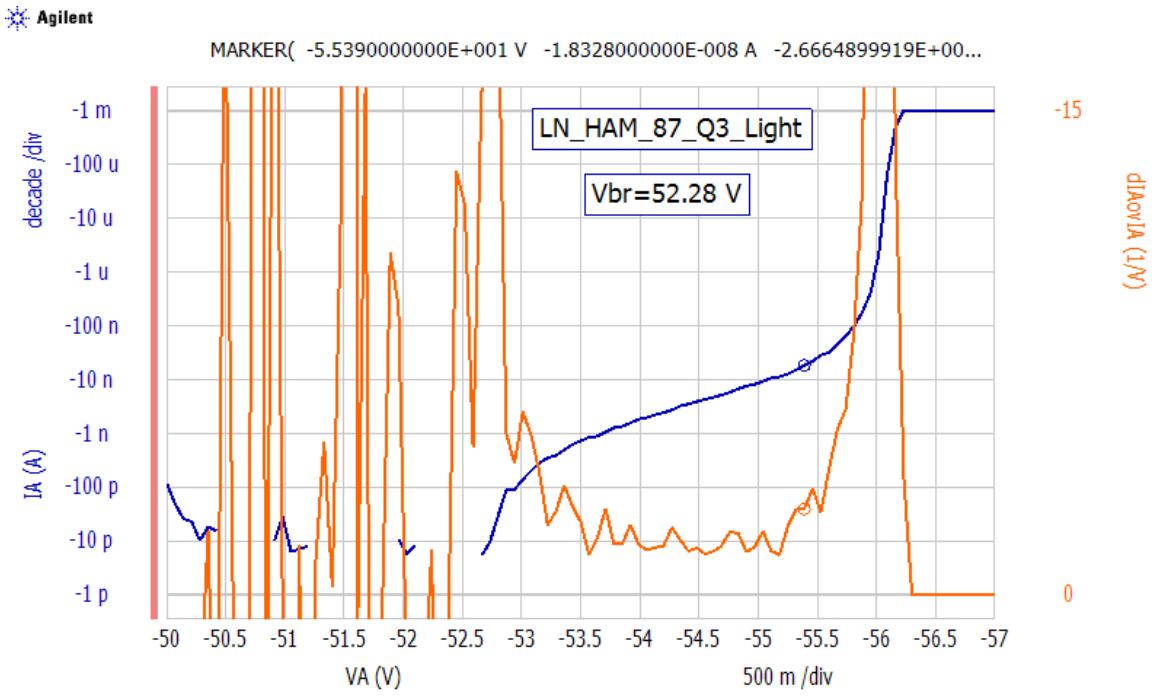

Figure A.19: Hamamatsu MEG Unit 87, Quadrant 3, Reverse IV Curve - Liquid Nitrogen, Some Light

Blue Line - Current (A) Orange - Normalized Derivative of Current

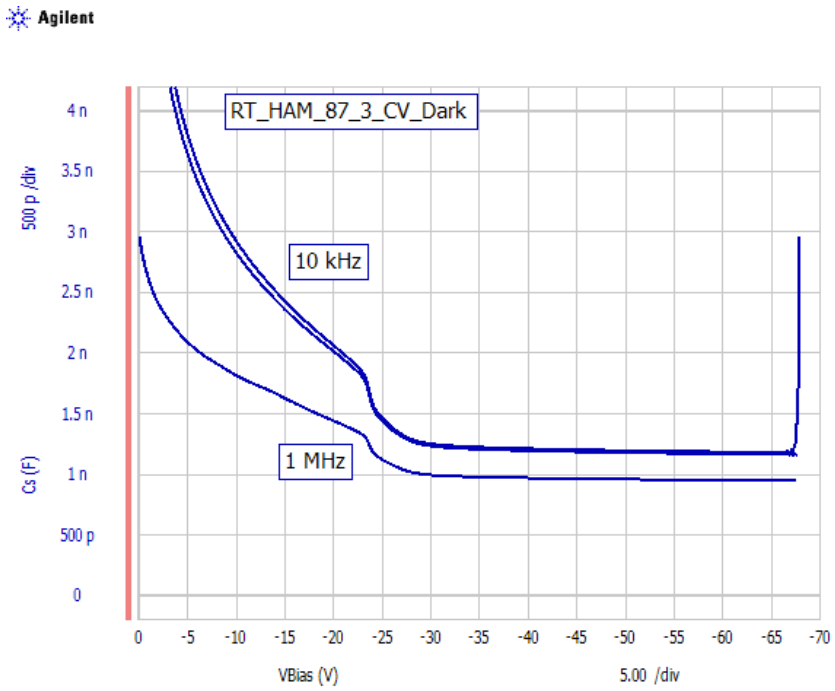

Figure A.20: Hamamatsu MEG Unit 87, Quadrant 3, Reverse CV Curve - Room Temperature

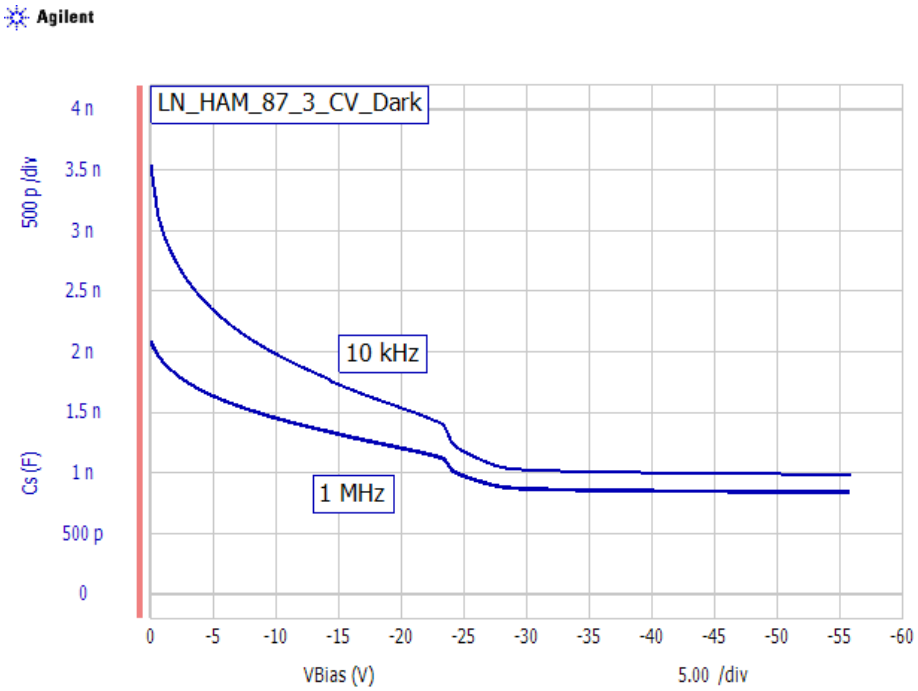

Figure A.21: Hamamatsu MEG Unit 87, Quadrant 3, Reverse CV Curve - Liquid Nitrogen

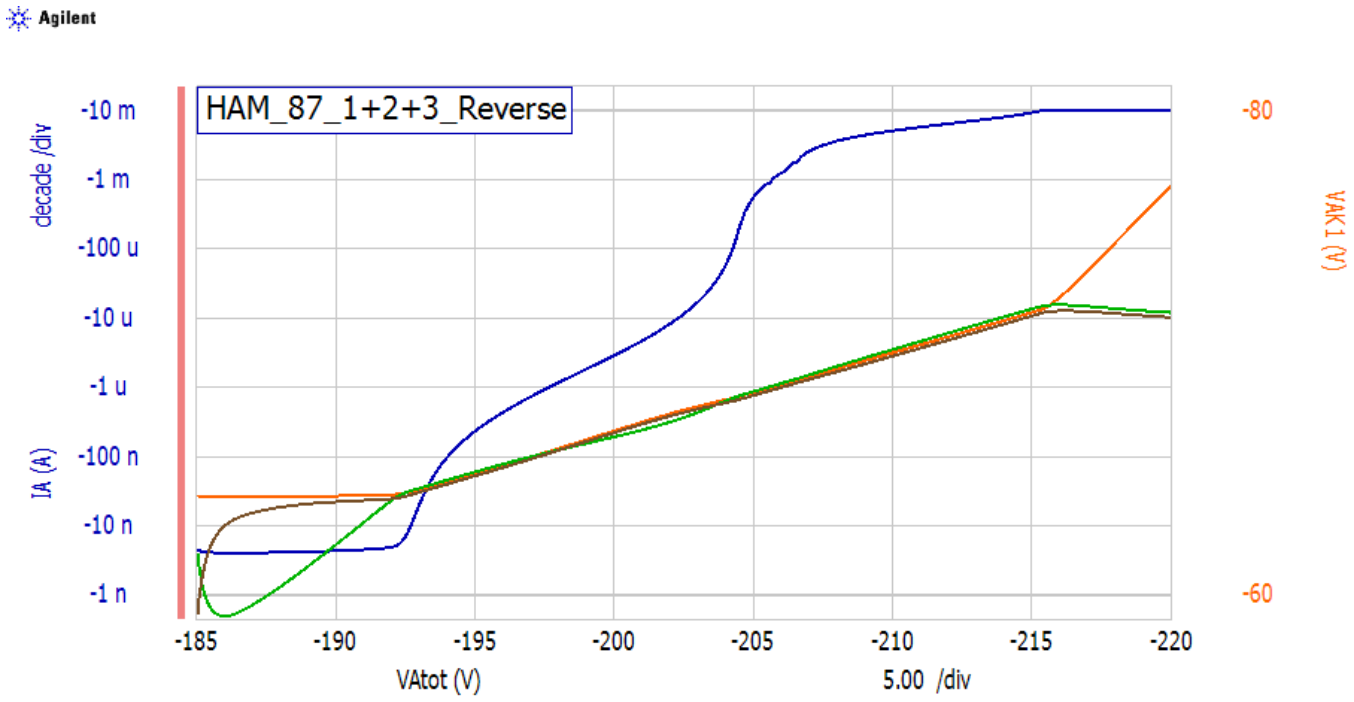

Figure A.22: Hamamatsu MEG Unit 87, Series IV Curve - Room Temperature

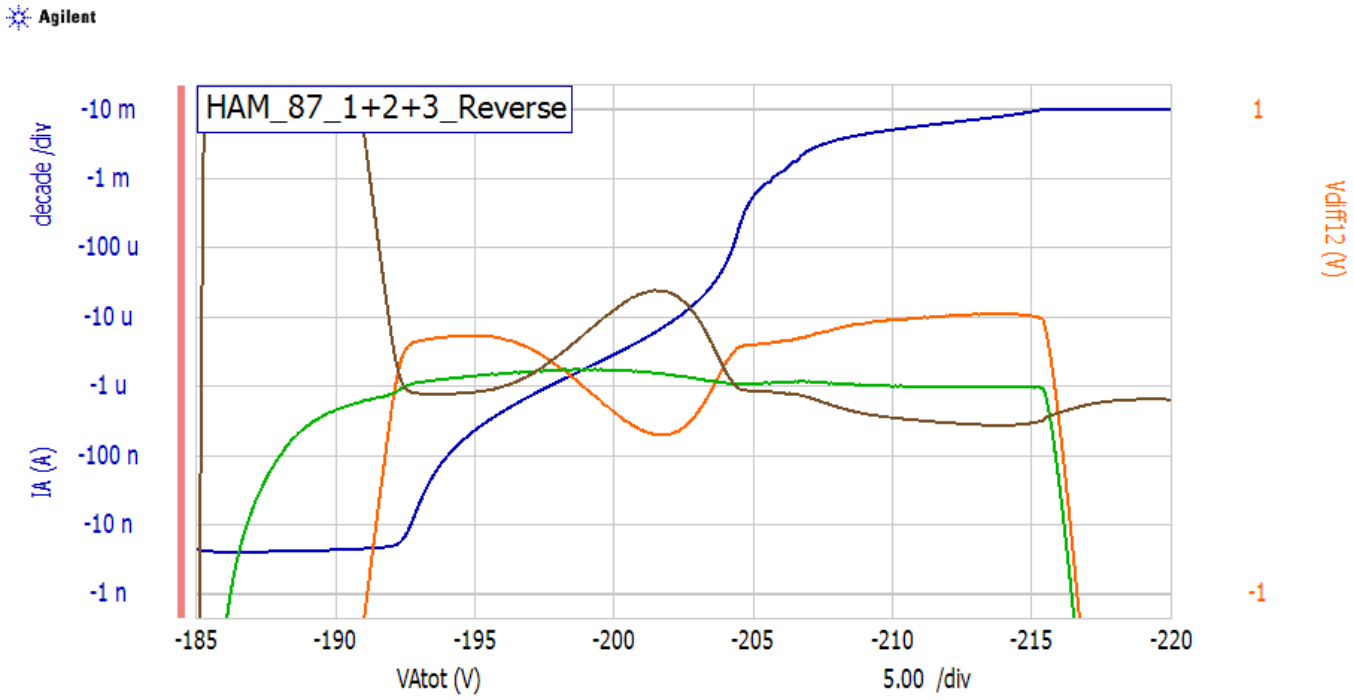

Figure A.23: Hamamatsu MEG Unit 87, Series IV Curve - Room Temperature

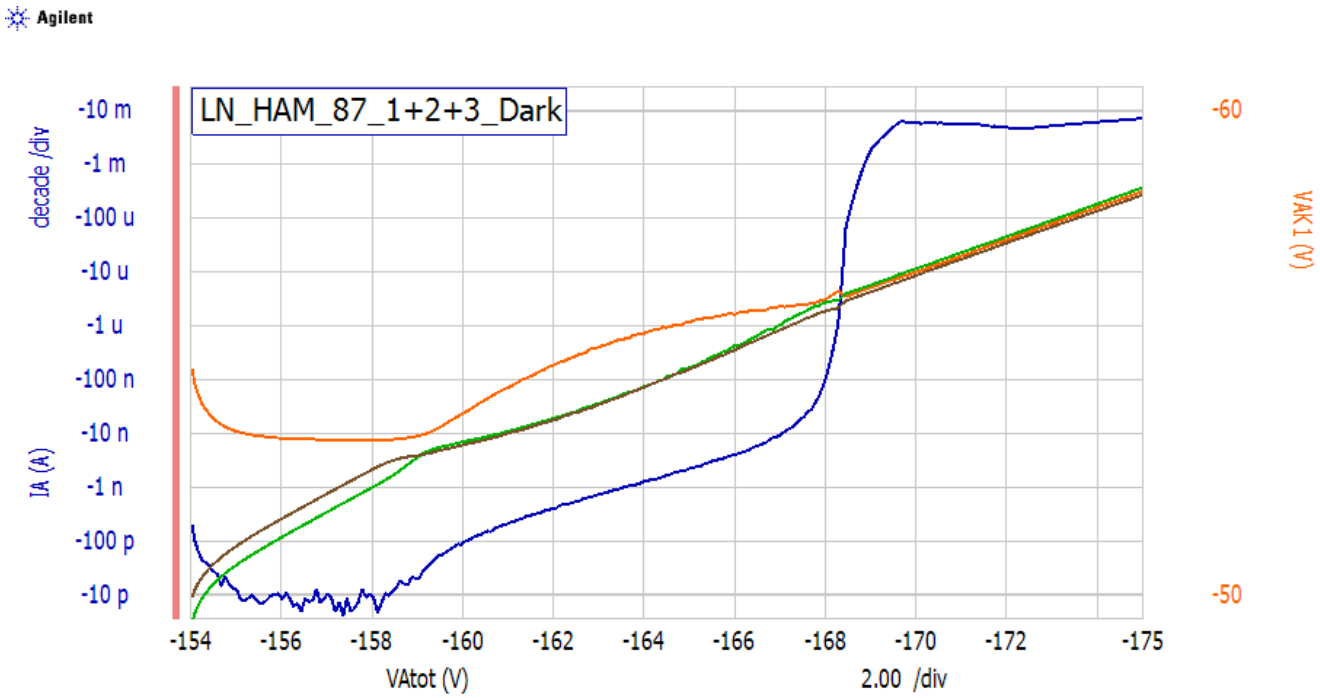

Figure A.24: Hamamatsu MEG Unit 87, Series IV Curve - Liquid Nitrogen

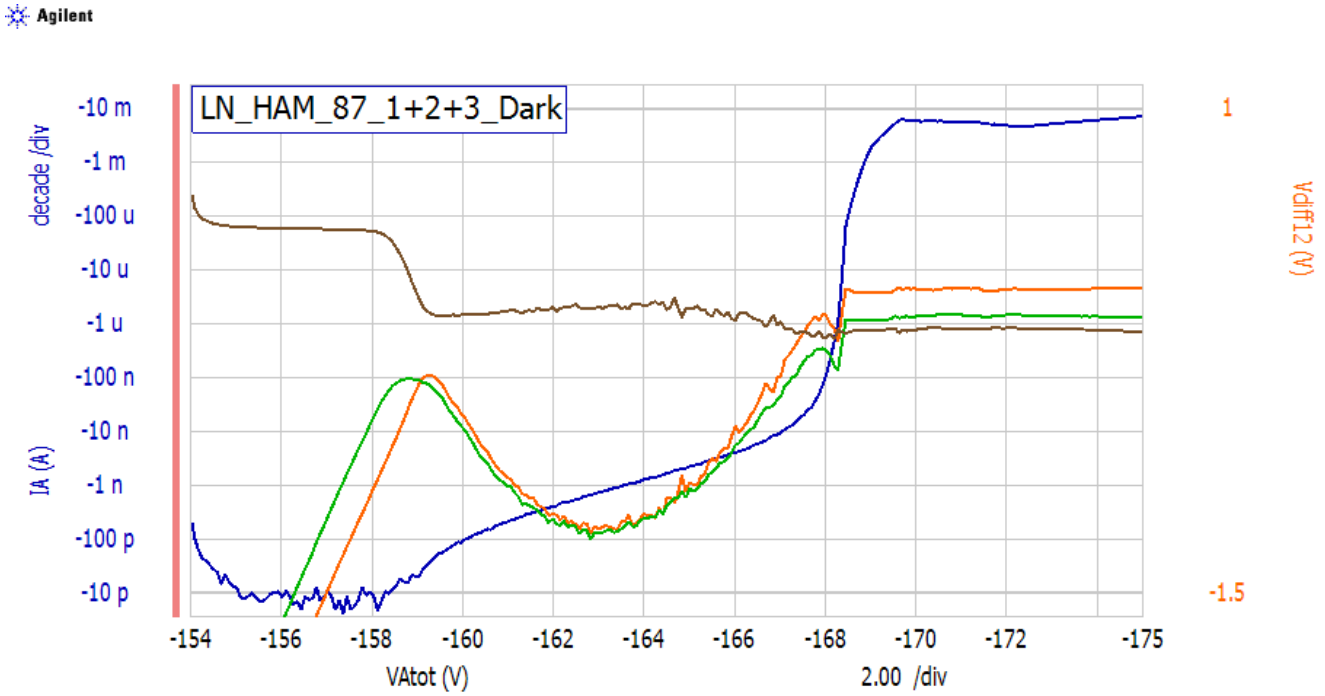

Figure A.25: Hamamatsu MEG Unit 87, Series IV Curve - Liquid Nitrogen

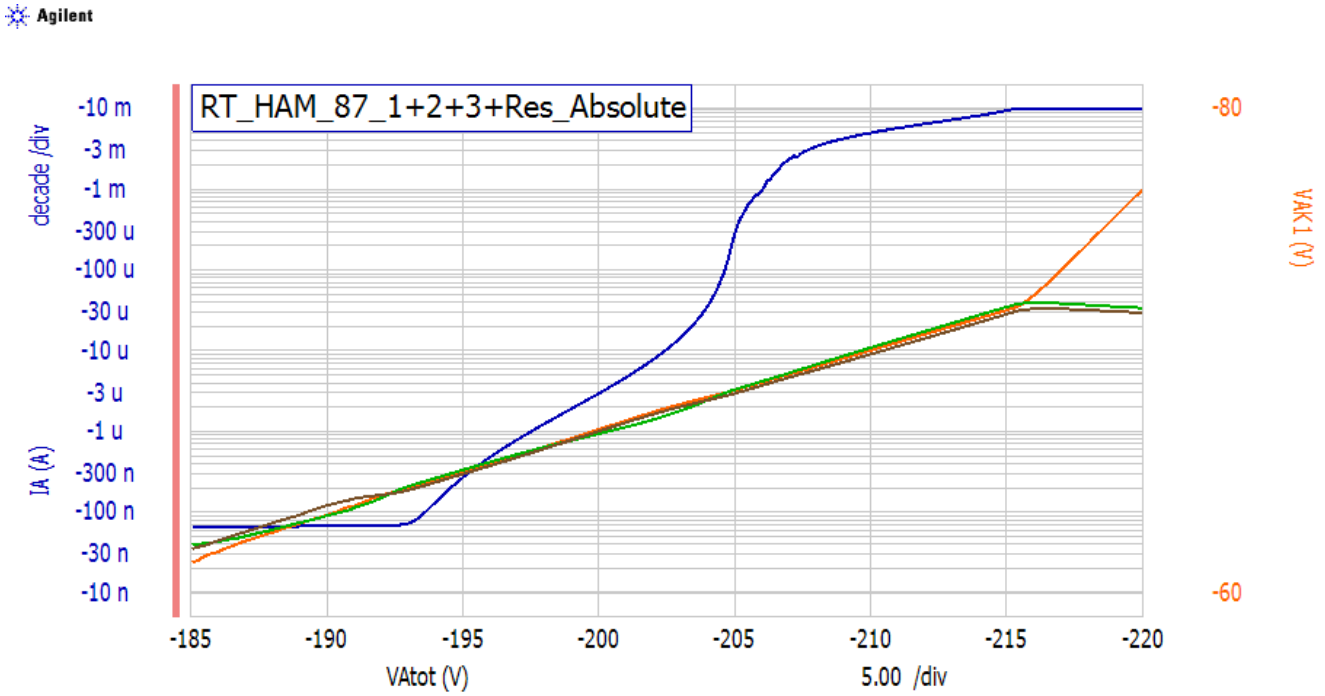

Figure A.26: Hamamatsu MEG Unit 87, Series IV Curve - Room Temperature with Resistors

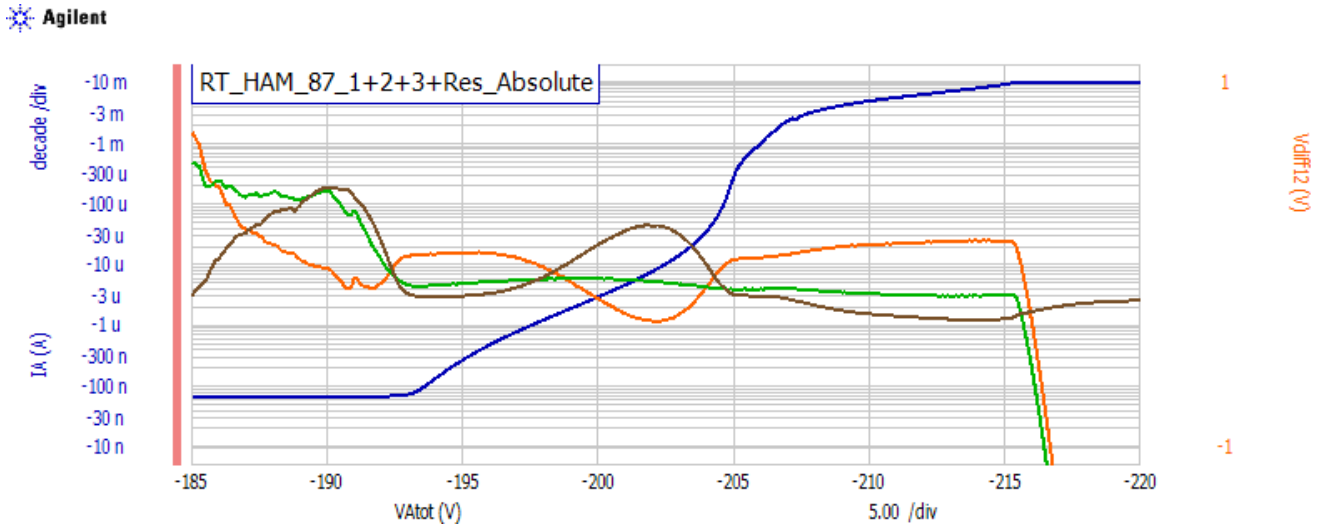

Figure A.27: Hamamatsu MEG Unit 87, Series IV Curve - Room Temperature with Resistors

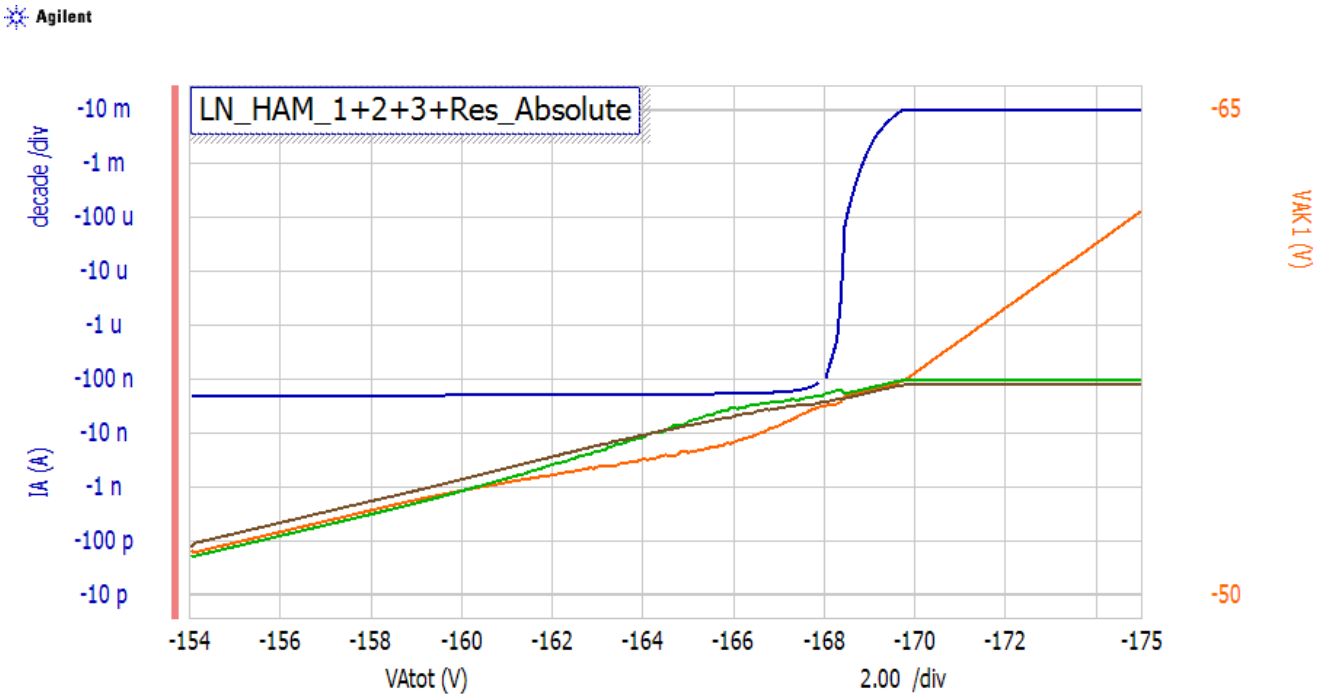

Figure A.28: Hamamatsu MEG Unit 87, Series IV Curve - Liquid Nitrogen with Resistors

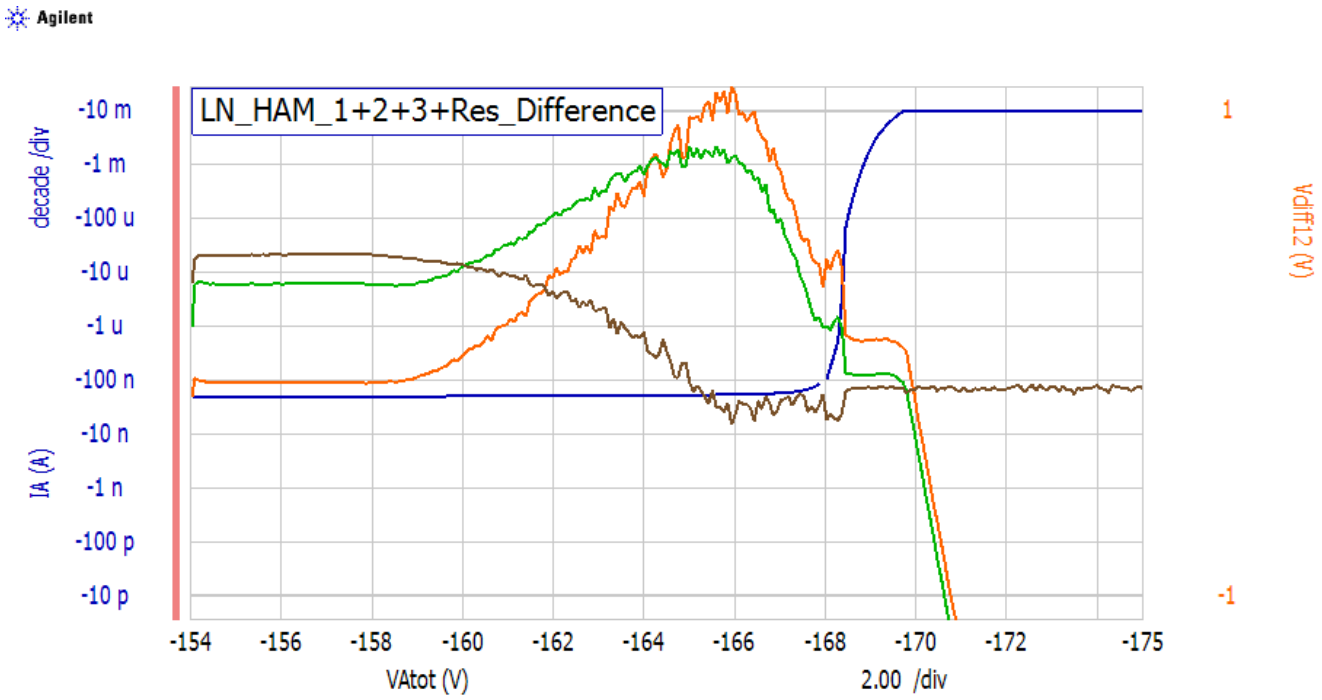

Figure A.29: Hamamatsu MEG Unit 87, Series IV Curve - Liquid Nitrogen with Resistors

Appendix B

MATLAB Code Used for Pulsed Light Analysis

```
%%This script will import data from several trials of the
%%Tektronix DPO Oscilloscope.  With some input parameters, it will process
%%the data
%%Version 2 - This will now isolate peaks and perform Gaussian fits on
%%them.  Every histogram must isolate the same number of peaks
%%Eric Raguzin
%%
%User can edit these parameters
clearvars -except final          %Clear everything except final data, so final data can be used in next step
plot_title='Hamamatsu MEG 87 Unit - Series Configuration - Light on All';    %Title of plot
quad={'SER'};     %Title of array for post-processing in next script
file_prefix='SER_';        %Input the prefix of all the data files
file_number_start=1;          %The start number of the file name
file_number_end=4;            %The end number of the file name
file_suffix='.txt';   %Change file suffix if need be
prominence_factor=.3;         %For peak analysis. Number must be between 0 and 1. 1 is strict definition of peak, 0 is loose definition of peak
%This array manually determines how many "false tails" to the end of the
%gaussian to skip.  If it's set to 1, it will stop at the first bump in the
```

```
%peak.  Increasing the number will cause it to continue further before
%defining the peak to isolate.  There must be one row for every histogram
%you plan on analyzing, and the array must be rectangular, so fill in zeros
%at the end if there's not enough peaks.  Now the isolation peak matrix
%will be a file in each directory named 'file_prefix' and then 'isolation'.
% Make it a matrix in the form of the other example ones.
%%
%Don't edit these parameters
q=1.6E-19;                  %Charge of electron for calculations
delimiterIn = '\t';         %Delimiter in imported data
headerlinesIn = 0;          %Where the actual data starts in the import

%%
%Generate File Names
filename_array=file_number_start:1:file_number_end;  %Will create an array of the amount of files to analyze with the correct numbers used in file name
filename_array_string=int2str(filename_array);  %Convert to strings to add to file names
filename_array_string(ismember(filename_array_string,' ')) = [];  %Removes all spaces that inadvertently were created
 for i=filename_array-(file_number_start-1)
     if i>10-(file_number_start)
         j={file_prefix,filename_array_string(10-(file_number_start-1)+2*(i-(10-(file_number_start-1))))
             ,filename_array_string(1+10-(file_number_start-1)+2*(i-(10-(file_number_start-1)))),file_suffix};   %Allows double digit numbers to be created
     else
     j={file_prefix,filename_array_string(i),file_suffix};   %Combines prefix, number and suffix strings.  For single digit numbers only.
     end
     filename{i}=strjoin(j,'');                              %Puts them all in an accessible array
     k={file_prefix,filename_array_string(i)};               %Create filenames without the suffix.  This will be used to name the data structure they're imported into.
```

```
44      filenameimport{i}=strjoin(k,'');                    %Puts
            them all in an accessible array
45  end
46  Isolation_skip_file=strjoin({file_prefix,'parameters',file_suffix
        },'');  %Creates the name of the file that should be in the
        directory
47  Isolation_skips=importdata(Isolation_skip_file);
                            %Imports that file, should be a straight
        matrix, no delimiter
48  %%
49  %Import and Process Data
50  data=struct;            %Create structure
51  [r,c]=size(Isolation_skips);    %Find the amount of peaks you're
        going to analyze
52  final.(quad{1}).final=cell(file_number_end-file_number_start,c+2);
        %Preallocate the final cell for post processing.  Make it the
        size of total histograms x total peaks.
53  for i=filename_array-(file_number_start-1)
54      data.(filenameimport{i}).data = importdata(filename{i},
            delimiterIn,headerlinesIn);  %Import data into field
55      data.(filenameimport{i}).biasv=data.(filenameimport{i}).data
            (1,3); %Bias voltage that it was at
56      data.(filenameimport{i}).scale=data.(filenameimport{i}).data
            (1,4);%What the vertical scale was on the scope, in mV/div
57      data.(filenameimport{i}).div=data.(filenameimport{i}).data
            (1,5);%The vertical position of the pulse signal in
            divisions.  The center division is zero, upwards is
            positive.
58      data.(filenameimport{i}).cal=data.(filenameimport{i}).data
            (1,6);%Gain of amplifier in electrons/mV
59      scale=data.(filenameimport{i}).scale;       %Easier to use
60      position=data.(filenameimport{i}).div;      %Easier to use
61      cal=625000/data.(filenameimport{i}).cal;    %Easier to use
62      %Do a bit of processing
63      increment=(scale*10)/256;                               %10
            divisions on the screen, 256 outputs, so gives mV/increment
64      scope_max=((5-position)*scale)-(2*increment);           %
            corresponding maximum mV reading depends on the scale and
            where the position was.  It's decreased by 2 readings
            because of clipping.
65      scope_min=(-(5+position)*scale)+(2*increment);          %
            Bottom two bins are not recorded
66      data.(filenameimport{i}).data(:,1)=linspace(scope_max,
            scope_min,252);   %What the X values are based on above
```

```
67      [row1] = find((data.(filenameimport{i}).data(:,2)),1,'first');
            %Find first nonzero result
68      [row2] = find(data.(filenameimport{i}).data(:,2),1,'last');
              %Find last nonzero result
69      [r,c]=size(data.(filenameimport{i}).data);
                                  %Total amount of rows
70
71      for j=row2:(r-1)        %From the last row with nonzero number
           to the end
72          data.(filenameimport{i}).data(end,:)=[];       %Delete all
               zeros
73      end
74      for j=1:(row1-2)         %From the beginning to the first
           nonzero number, leaving one zero
75          data.(filenameimport{i}).data(1,:)=[];       %Delete all
               zeros
76      end
77      x=data.(filenameimport{i}).data(:,1);        %Just to simplify
           calling x and y below
78      y=data.(filenameimport{i}).data(:,2);        %X is mV, Y is
           occurences
79      min_prominence=prominence_factor*max(y);     %Base the
           prominence factor off the user input and the maximum range
80
81      %Create a dummy array to use with findpeaks.  findpeaks only
           works with
82      %ascending X values, so I do this to get the array positions
           of the
83      %peaks and then transfer that to the real data.
84      z=linspace(1,length(data.(filenameimport{i}).data),length(data
           .(filenameimport{i}).data));
85
86      figure
87      hold on
88      subplot(2,1,1)
89      plot(x,y,'b')                          %Plots the data and the
           peaks
90      set(gca, 'XDir', 'reverse')                                %Needs to
           be reversed because we use negative bias
91      Voltage = num2str(data.(filenameimport{i}).biasv);
                               %Change Bias Voltage to string
92      top_title = strcat(plot_title,{', '},'Bias Voltage:',Voltage,{
           ' V'}); %Creates title
93      title(top_title)                                          %Print the
           plot title
```

```
94      ylabel('Occurences');                                   %Set the Y
           -axis.  No X-axis for spacing reasons.
95
96
97
98      scaler=Isolation_skips(i,7);
99      location=Isolation_skips(i,8);
100     mu=Isolation_skips(i,9);
101     starting=Isolation_skips(i,10);
102
103     x_gauss=x(starting:end);
104
105     gauss_diff=size(x)-size(x_gauss);
106
107     norm = scaler*normpdf(x_gauss,location,mu);
108     norm = [zeros(gauss_diff(1),1); norm];
109     hold on
110     subplot(2,1,1)
111     plot(x,norm,'r')                        %Plots the data and the
           peaks
112
113     y=y-norm;
114     y(y<0) = 0;
115
116      f = fit(x,y,'gauss3');
117     coeffvals = coeffvalues(f);                     %Find the
           parameters of the fit
118     subplot(2,1,2)
119     hold on                                         %There's gonna be
           a bunch of iterations
120     plot(f,x,y)
121     set(gca, 'XDir', 'reverse')                             %Needs to
           be reversed because we use negative bias
122
123
124     %Finding Peaks
125     [peaky,peakx]=findpeaks(y,z,'MinPeakProminence',min_prominence
           );          %Save data about peaks
126     for j=1:length(peakx)          %From the beginning to the first
           nonzero number
127       peakx(j)=x(peakx(j));    %change back into the main
             coordinate system
128     end
129     subplot(2,1,2)
130     plot(peakx,peaky,'r*')
```

```
131     set(gca, 'XDir', 'reverse')                    %Needs to
        be reversed because we use negative bias
132     %%Isolating Peaks
133
134
135     peaks_to_do=3;  %Each iteration goes to the next row of
        Isolation_skips. Counts the number of non-zero elements,
        and that's the amount of peaks to isolate. Quickly changed
         to 2 as emergency. Need a better way to determine this
136     for k=1:1:peaks_to_do                          %Go through the
        number of peaks set above
137         end_of_tail_x=find(x==peakx(k));           %Find the
            corresponding X value in the data of that peak
138         start_of_tail_x=end_of_tail_x;             %%Initialize this
            variable for later
139         j=0;                                       %Can't give value
            to variables in while declaration
140         size_of_x=size(x);
141
142         if (end_of_tail_x+Isolation_skips(i,2*k)>size_of_x(1))
143             end_of_tail_x=size_of_x(1);
144         else
145             end_of_tail_x=end_of_tail_x+Isolation_skips(i,2*k);
146         end
147
148         if (start_of_tail_x-Isolation_skips(i,2*k-1)<1)
149             start_of_tail_x = 1;
150         else
151             start_of_tail_x=start_of_tail_x-Isolation_skips(i,2*k
                -1);  %Keep going back by 1
152         end
153         %Plot a dotted rectangle around the peak you have isolated
154         subplot(2,1,2)
155         rectangle('Position',[x(end_of_tail_x) 0 x(start_of_tail_x
            )-x(end_of_tail_x) peaky(k)],'LineStyle','--')
156         x_temp(:,k)=x;                             %Copy the
            data over for this isolated peak
157         y_temp(:,k)=y;                             %This
            array will keep building with each peak
158
159         for j=1:start_of_tail_x-1                  %Make everything
            before the start of the gaussian 0
160             y_temp(j,k)=0;
161         end
```

```
162         [r]=size(x);                                %Find the end of the
                data (has been changed since previous size command
163         for j=end_of_tail_x+1:r                     %Make everything
               after the end of the gaussian 0
164             y_temp(j,k)=0;
165         end
166 %        for j=start_of_tail_x:end_of_tail_x     %Subtract out the
        "junk" from everything in between
167 %           y_temp(j,k)=y_temp(j,k)-end_of_tail_y;
168 %        end
169
170         f = fit(x_temp(:,k),y_temp(:,k),'gauss1');  %Fit the given
                peak that we just isolated
171         coeffvals = coeffvalues(f);                 %Find the
               parameters of the fit
172         data.(filenameimport{i}).position{k}=coeffvals(1,2);    %
               Save the X position
173         data.(filenameimport{i}).RMS{k}=coeffvals(1,3);         %
               Save the RMS width
174         final.(quad{1}).final{i,k+6}=data.(filenameimport{i}).RMS{
               k};          %Save the RMS width in mv
175         final.(quad{1}).final{i,k+2}=coeffvals(1,3)*(625000/data.(
               filenameimport{i}).cal);          %Save the RMS width
               converted to ENC to be plotted with other data
176         subplot(2,1,2)
177         hold on                                     %There's gonna
                be a bunch of iterations
178         plot(f,x,y)                                 %Plot the
               Gaussian fit
179         %plot(x_temp(:,k),y_temp(:,k),'y')%If desired, plot the
               shiftedpeak
180         set(gca, 'XDir', 'reverse')                 %Again,
               reverse this one
181     end
182
183     %Now that we have the array of all of our positions, this line
            takes
184     %that saved "cell", converts it into an array, then finds the
185     %difference between each corresponding peak, then averages
           those
186     %differences and makes it a positive number.  That is the
           average
187     %distance between peaks
188     peak_spacing=abs(mean(diff(cell2mat(data.(filenameimport{i}).
           position))));
```

```
189     final.(quad{1}).final{i,6}=peak_spacing;
190     %Overall gain is (average peak width)/(charge of electron*
            preamplifier gain)
191     gain=round(peak_spacing*cal,0);                    %Rounds to
            nearest integer
192
193     %This next bit determines where the annotation boxes that tell
             the RMS
194     %Width of all the peaks goes.  The issue is that the
            annotation box
195     %positions are determined by a different coordinate system
            than the
196     %data, so this code lets them work together
197
198     axPos = get(gca,'Position');    %Gets the absolute positions
            of the plotted data portion of the plot
199     xMinMax = xlim;                 %Gives the minimum and maximum
             values of that plotted area in terms of the data
200     yMinMax = ylim;
201     gaussian_positions=cell2mat(data.(filenameimport{i}).position)
            ;     %Turns that saved cell of peak positions into a
            usable array
202     yAnnotation = axPos(2) + ((1.25*yMinMax(2) - yMinMax(1))/(
            yMinMax(2)-yMinMax(1))) * axPos(4);   %Y Location of
            annotations is always the same, 25% above the top of the
            bottom plot.  Just converts into plot coordinates
203     for k=1:1:peaks_to_do           %Every X value needs to be
            calculated on it's own
204         xAnnotation(1,k) = 0.5*axPos(1) + ((gaussian_positions(k)
                - xMinMax(2))/(xMinMax(1)-xMinMax(2))) * axPos(3);    %
                Starting X-value is determined by peak positions, but
                that's the left corner of the annotation.  By trial and
                 error I found that the 0.5 multiplier works best.
205         dim(k,:) = [xAnnotation(1,k) yAnnotation .2 0];
                                %Size of info box
206         str = strcat('RMS Width:',{' '},num2str(data.(
                filenameimport{i}).RMS{k}),{' '},'mV');   %Text for
                info box with extrapolated data.
207         annotation('textbox',dim(k,:),'String',str,'FitBoxToText',
                'on');     %Add info box where we want, saying what we
                want
208     end
209
210     bottom_title = strcat('Each peak isolated and fit to Gaussian
            curve to find position and RMS width.  From position, Gain:
```

```
        ',{' '},num2str(gain));   %Title for bottom plot.
211     title(bottom_title);
212     xlabel('Pulse Peak (mV)');      %Label bottom plot
213     ylabel('Occurences');
214
215     legend('off');                  %Plotting multiple gaussian
           fits leads to annoying legends
216     hold off;                       %Let the next iteration start
           a new plot
217
218
219     %Result stored in a structure field that will keep all the
           results for Gain vs. Bias V plot.
220     final.(quad{1}).final{i,2}=gain;
221     %Gain is in the Y axis column
222     final.(quad{1}).final{i,1}=data.(filenameimport{i}).biasv;
223     %Bias voltage is in the X axis column
224
225     clear x_temp                    %If these variables are
           different sizes the next time, this needs to be done
226     clear y_temp                    %Or else there's trouble
227 end
```

Appendix C

Hamamatsu MEG 87 Unit Pulsed Light Analysis Results

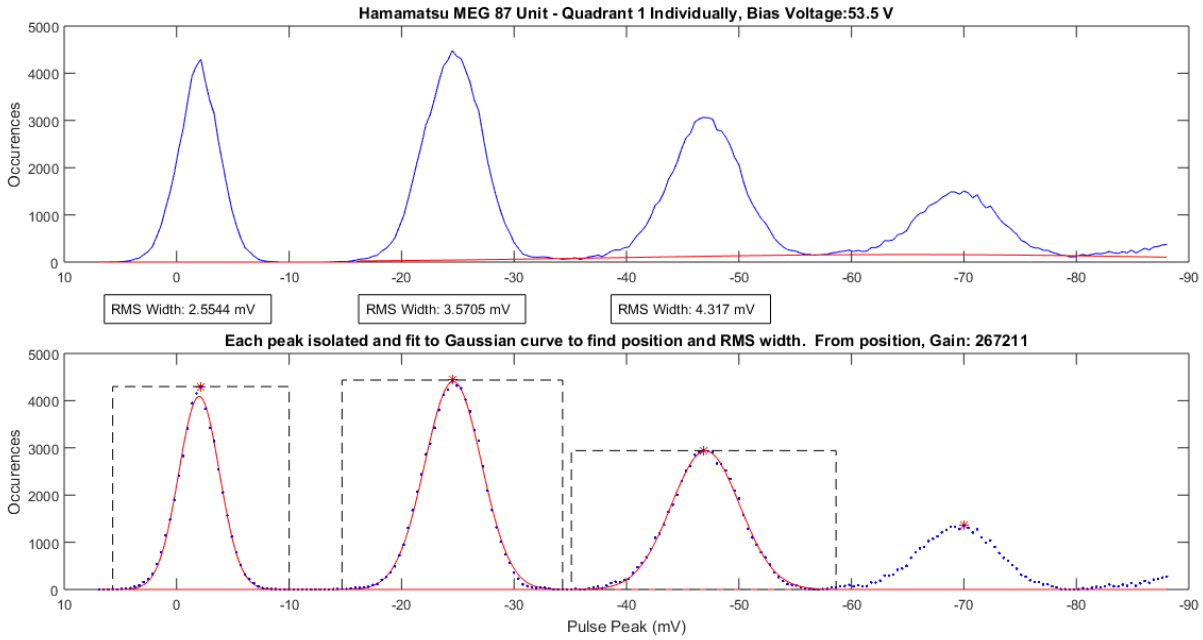

Figure C.1: Hamamatsu MEG Unit 87, Quadrant 1 Pulsed Light Histogram Analysis- 53.5 V

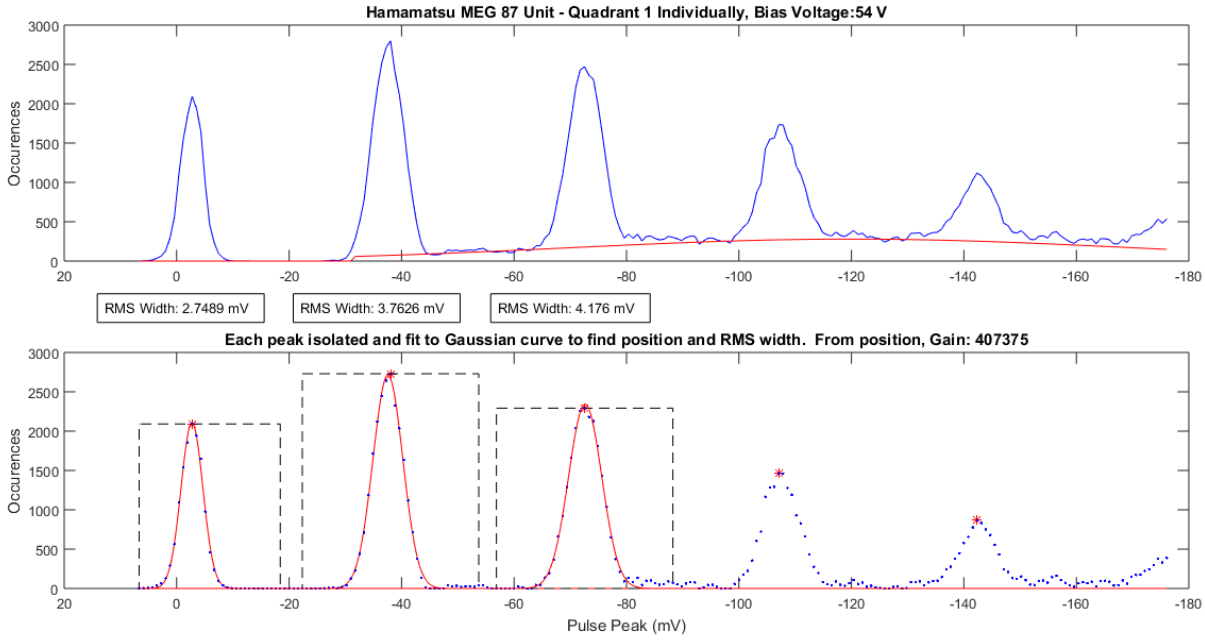

Figure C.2: Hamamatsu MEG Unit 87, Quadrant 1 Pulsed Light Histogram Analysis- 54 V

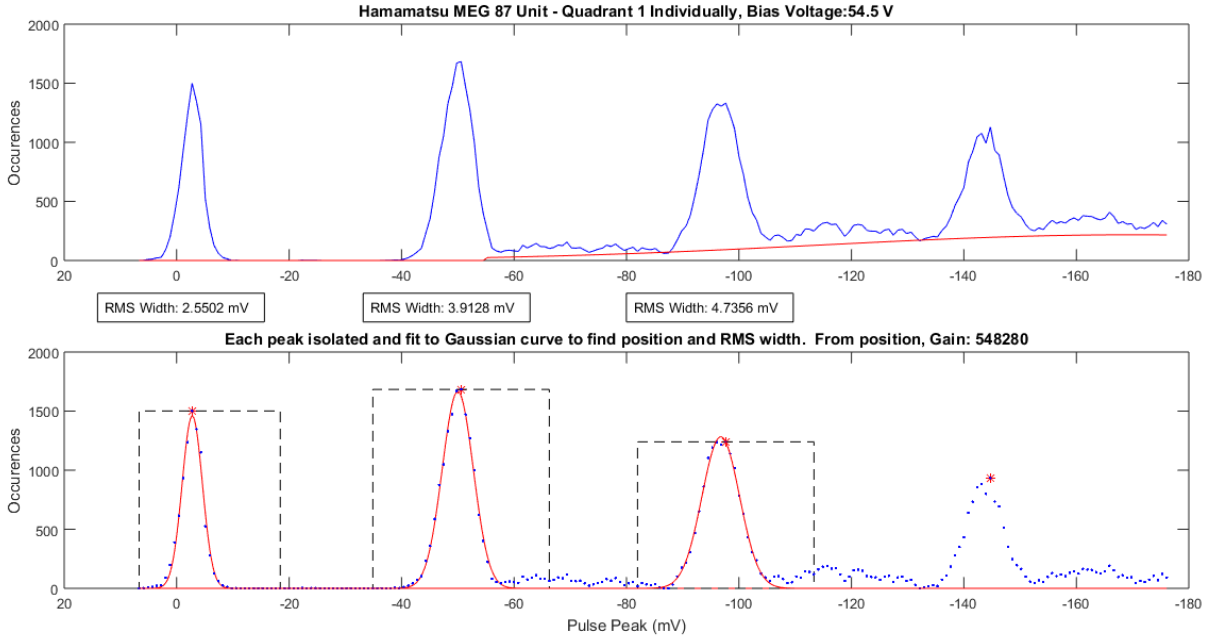

Figure C.3: Hamamatsu MEG Unit 87, Quadrant 1 Pulsed Light Histogram Analysis- 54.5 V

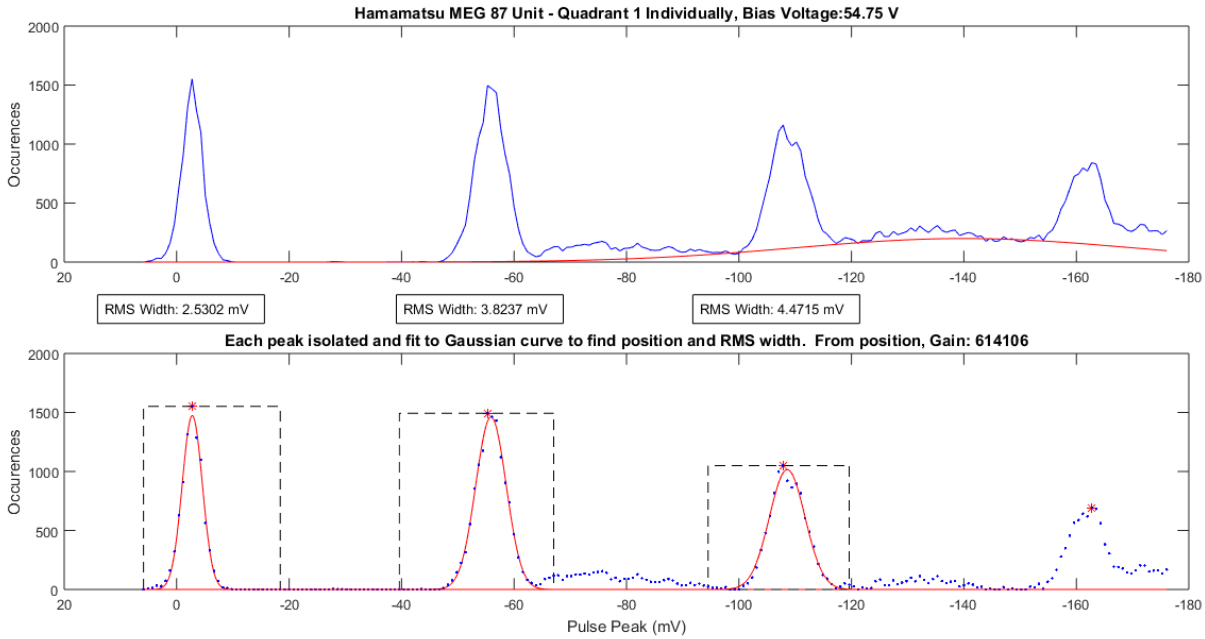

Figure C.4: Hamamatsu MEG Unit 87, Quadrant 1 Pulsed Light Histogram Analysis- 54.75 V

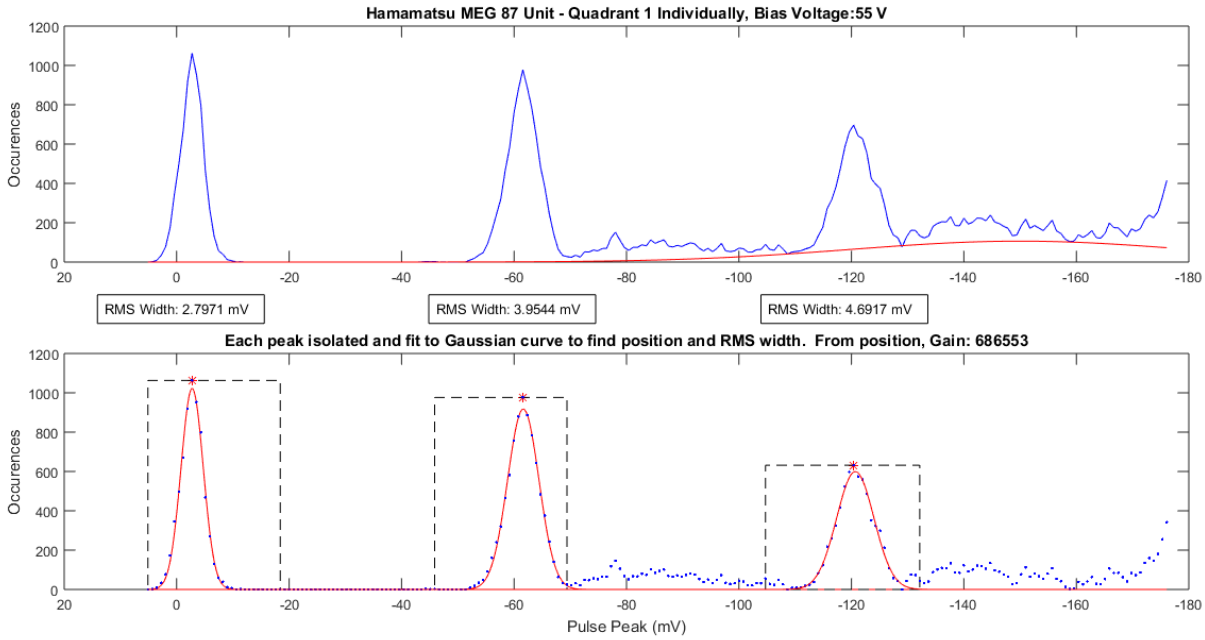

Figure C.5: Hamamatsu MEG Unit 87, Quadrant 1 Pulsed Light Histogram Analysis- 55 V

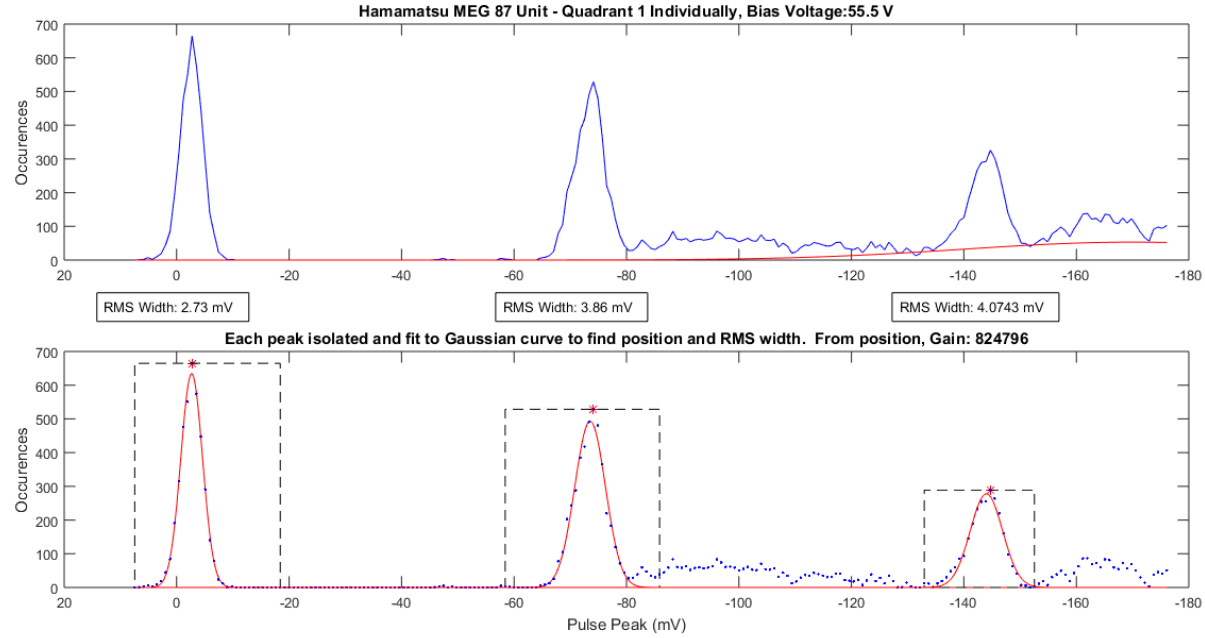

Figure C.6: Hamamatsu MEG Unit 87, Quadrant 1 Pulsed Light Histogram Analysis- 55.5 V

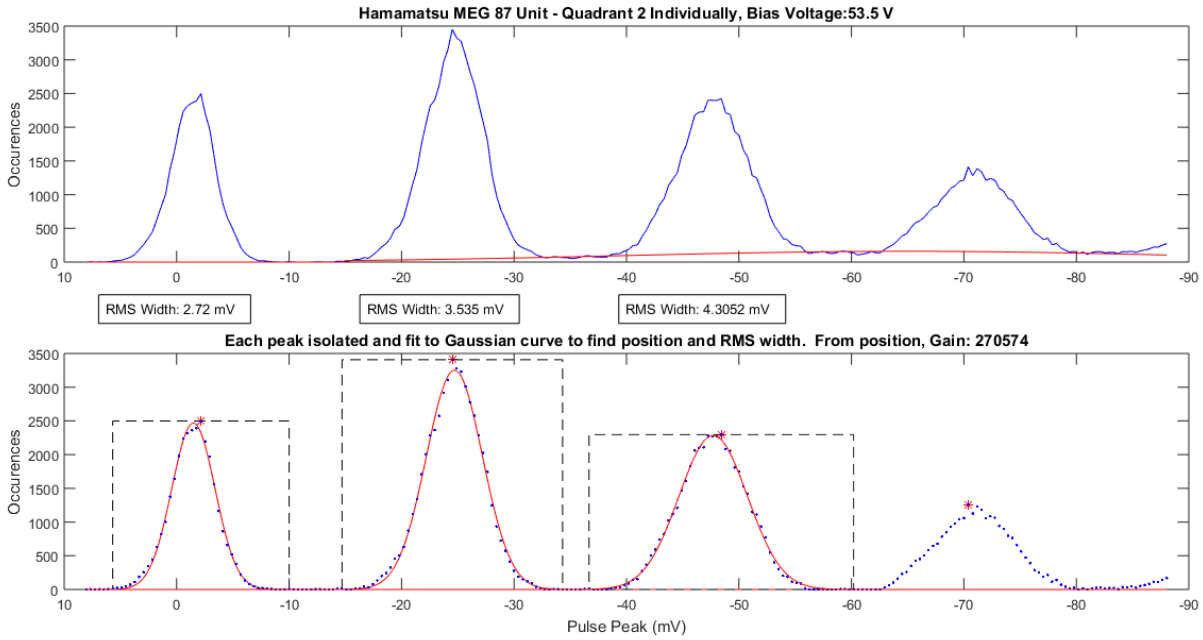

Figure C.7: Hamamatsu MEG Unit 87, Quadrant 2 Pulsed Light Histogram Analysis- 53.5 V

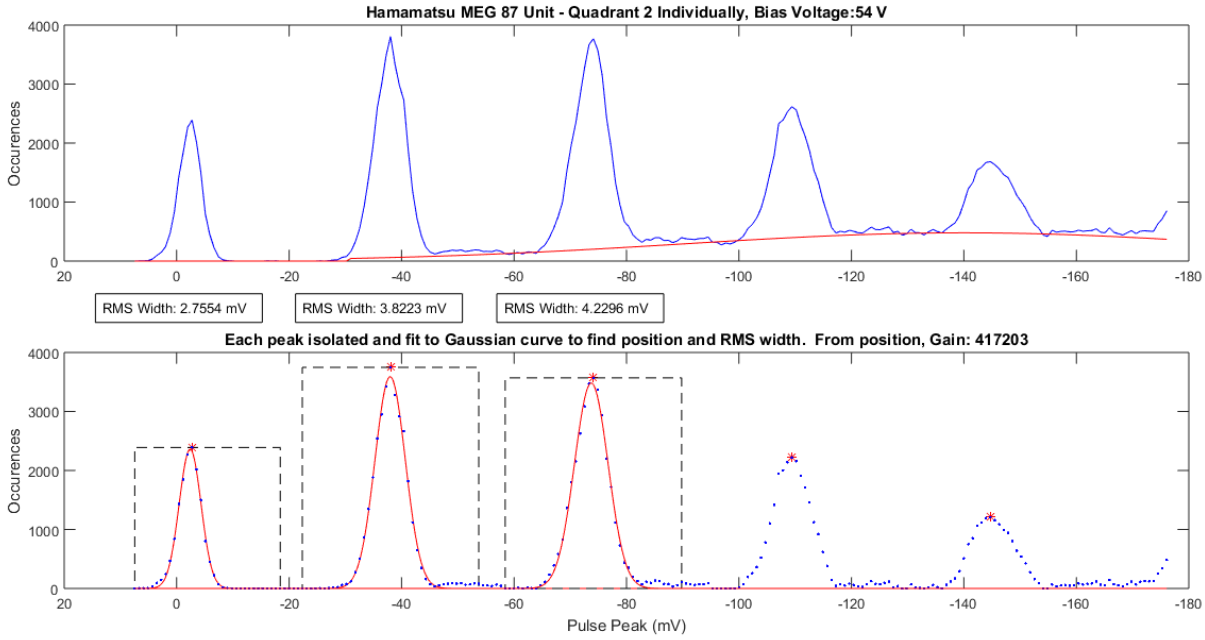

Figure C.8: Hamamatsu MEG Unit 87, Quadrant 2 Pulsed Light Histogram Analysis- 54 V

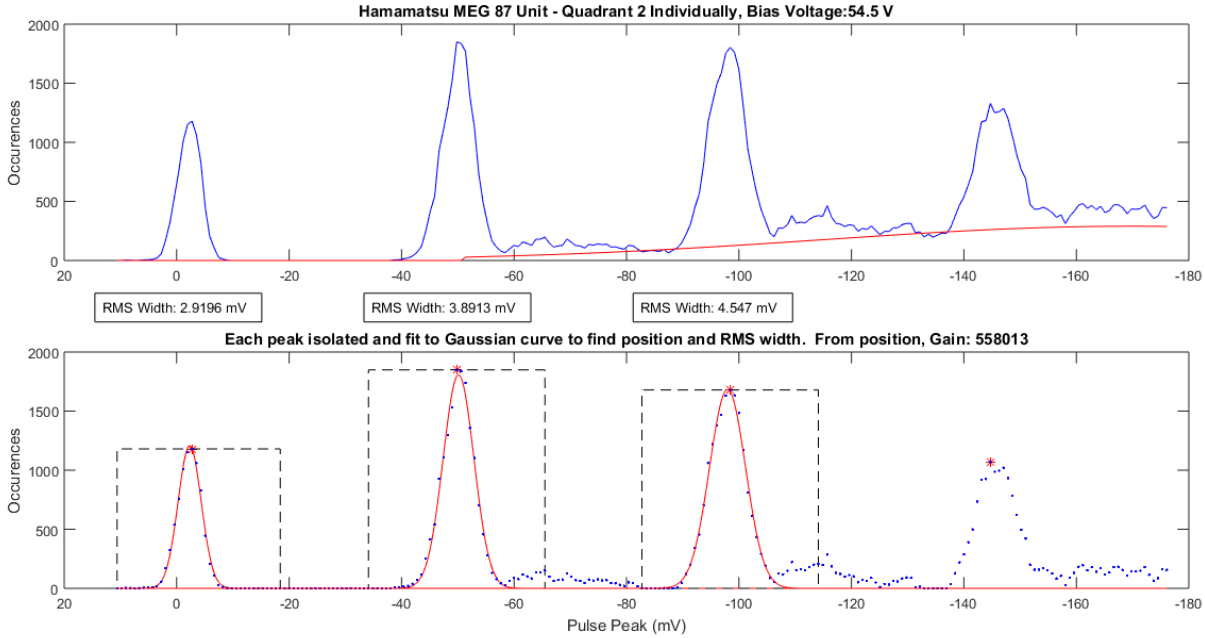

Figure C.9: Hamamatsu MEG Unit 87, Quadrant 2 Pulsed Light Histogram Analysis- 54.5 V

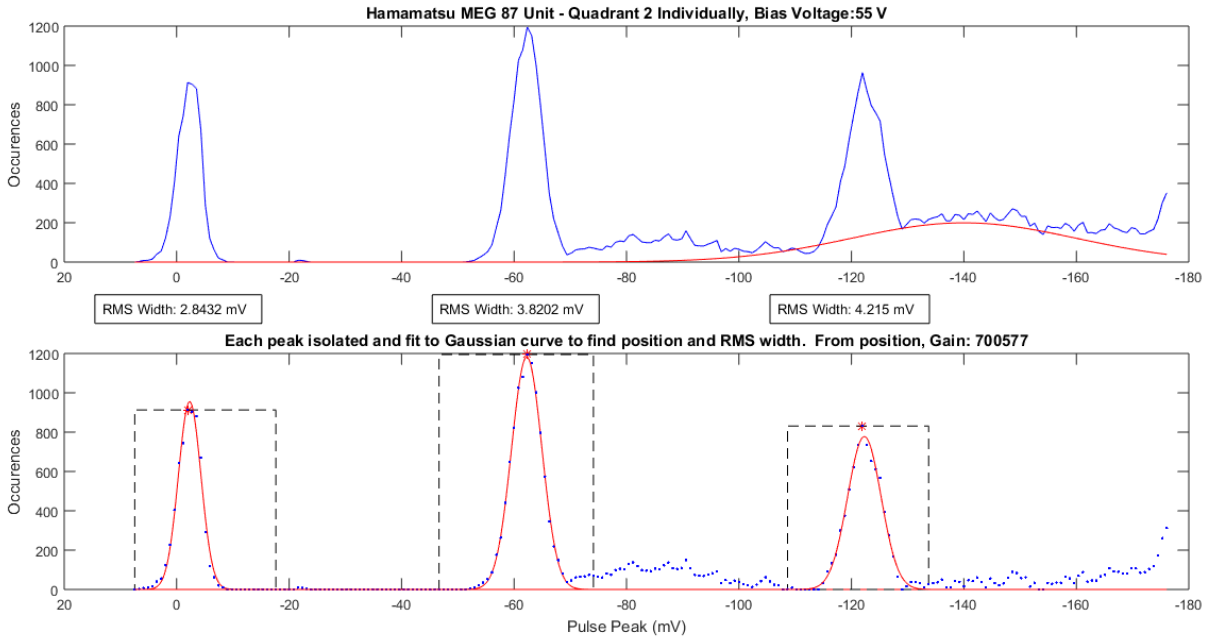

Figure C.10: Hamamatsu MEG Unit 87, Quadrant 2 Pulsed Light Histogram Analysis- 55 V

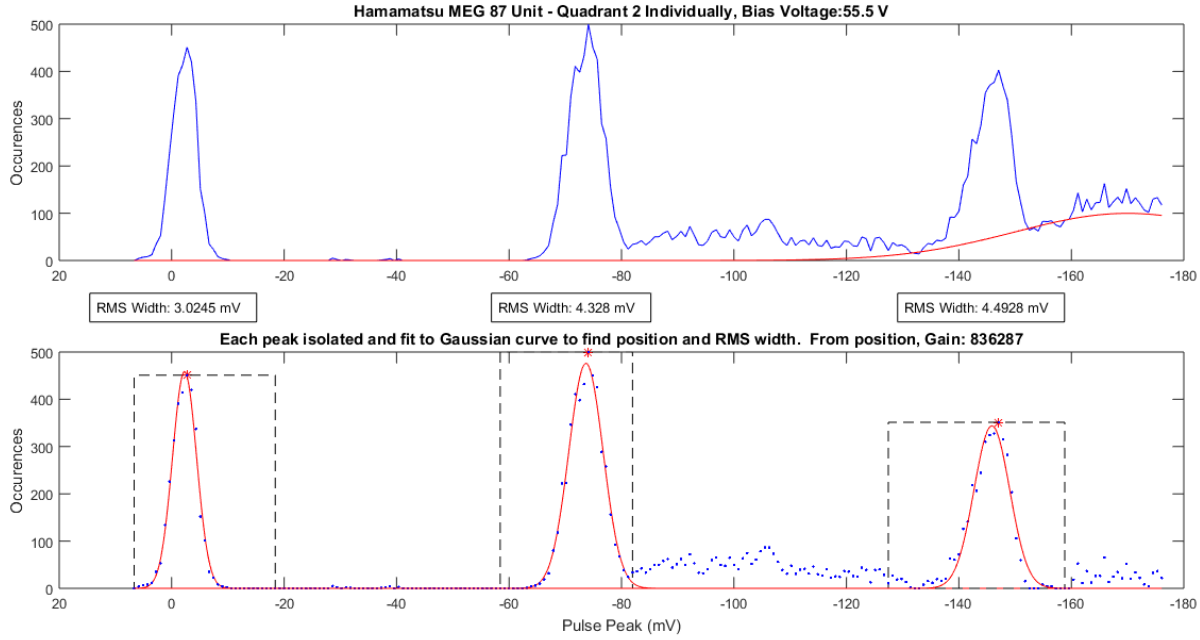

Figure C.11: Hamamatsu MEG Unit 87, Quadrant 2 Pulsed Light Histogram Analysis-55.5 V

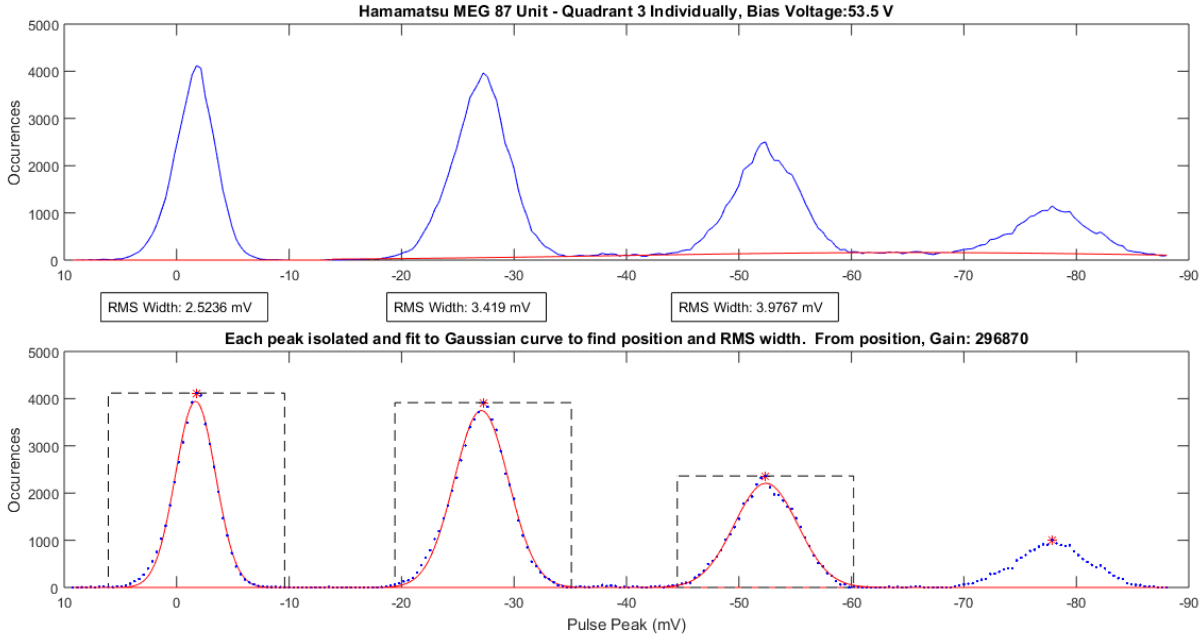

Figure C.12: Hamamatsu MEG Unit 87, Quadrant 3 Pulsed Light Histogram Analysis-53.5 V

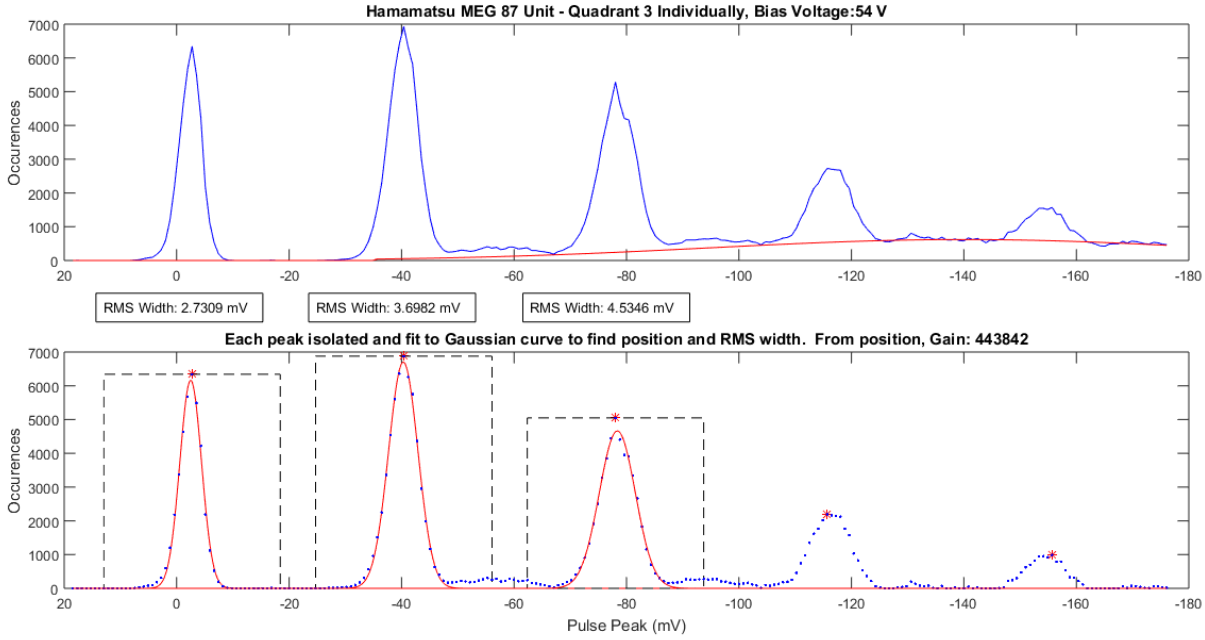

Figure C.13: Hamamatsu MEG Unit 87, Quadrant 3 Pulsed Light Histogram Analysis- 54 V

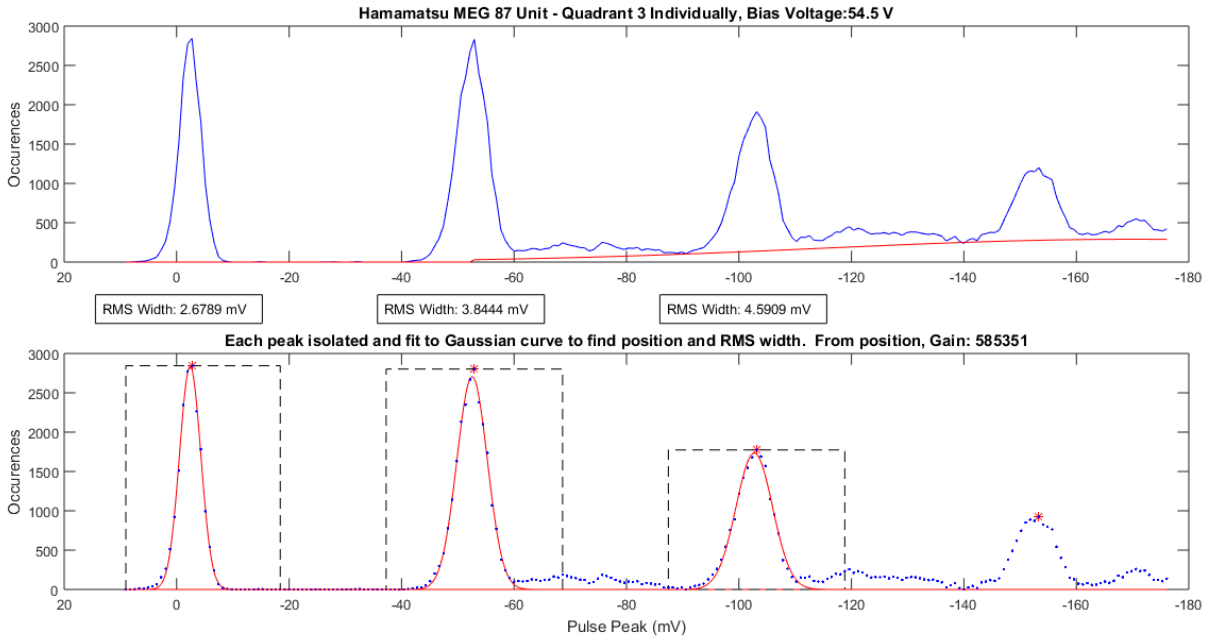

Figure C.14: Hamamatsu MEG Unit 87, Quadrant 3 Pulsed Light Histogram Analysis- 54.5 V

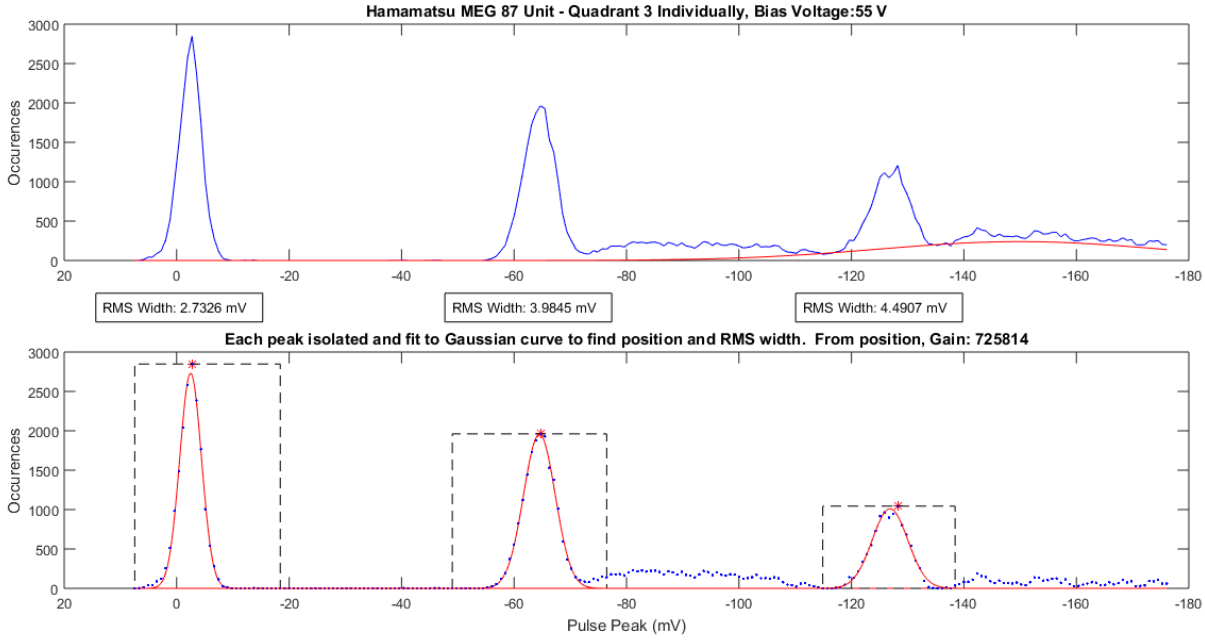

Figure C.15: Hamamatsu MEG Unit 87, Quadrant 3 Pulsed Light Histogram Analysis- 55 V

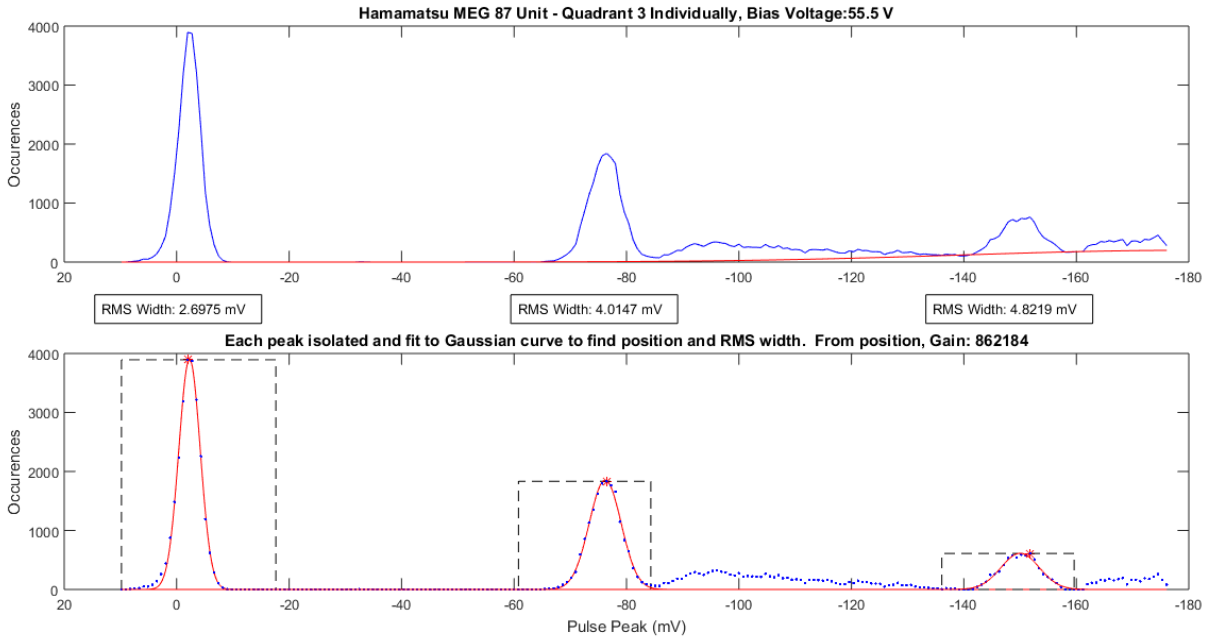

Figure C.16: Hamamatsu MEG Unit 87, Quadrant 3 Pulsed Light Histogram Analysis- 55.5 V

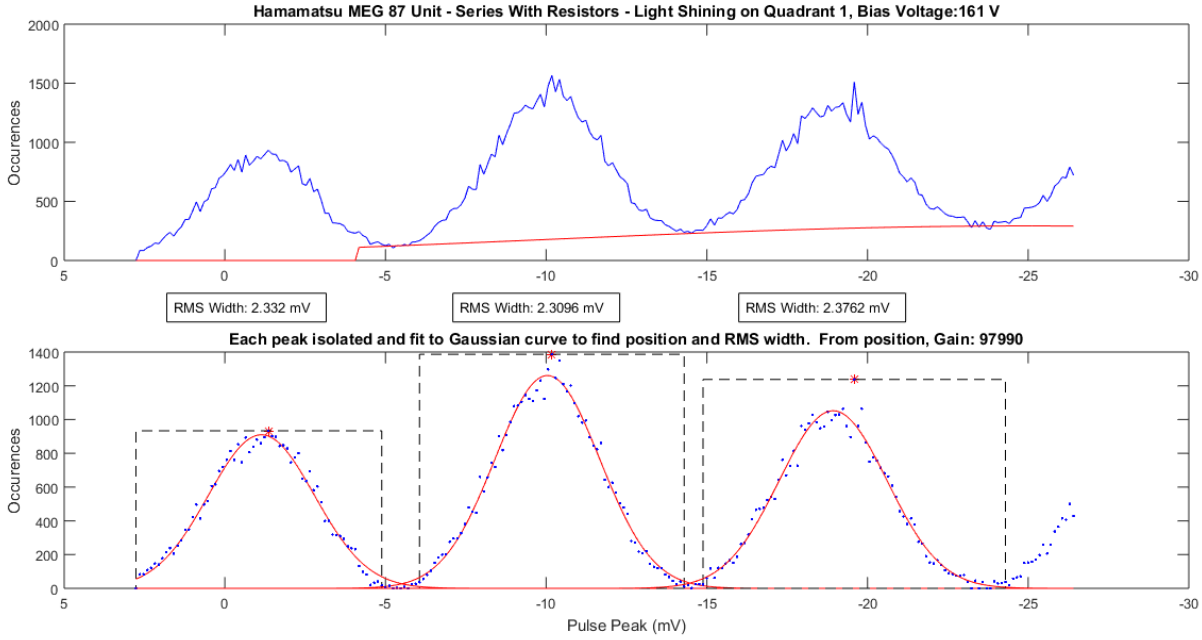

Figure C.17: Hamamatsu MEG Unit 87, Pulsed Light Histogram Analysis for Series Configuration with Light Shining on Quadrant 1- 161 V

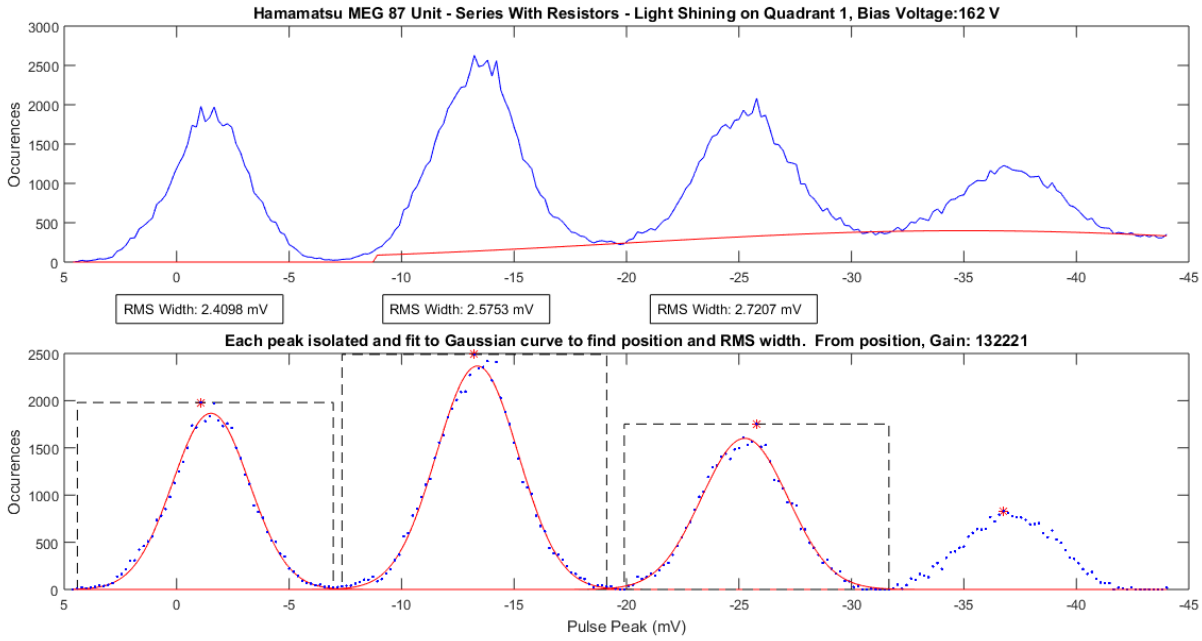

Figure C.18: Hamamatsu MEG Unit 87, Pulsed Light Histogram Analysis for Series Configuration with Light Shining on Quadrant 1- 162 V

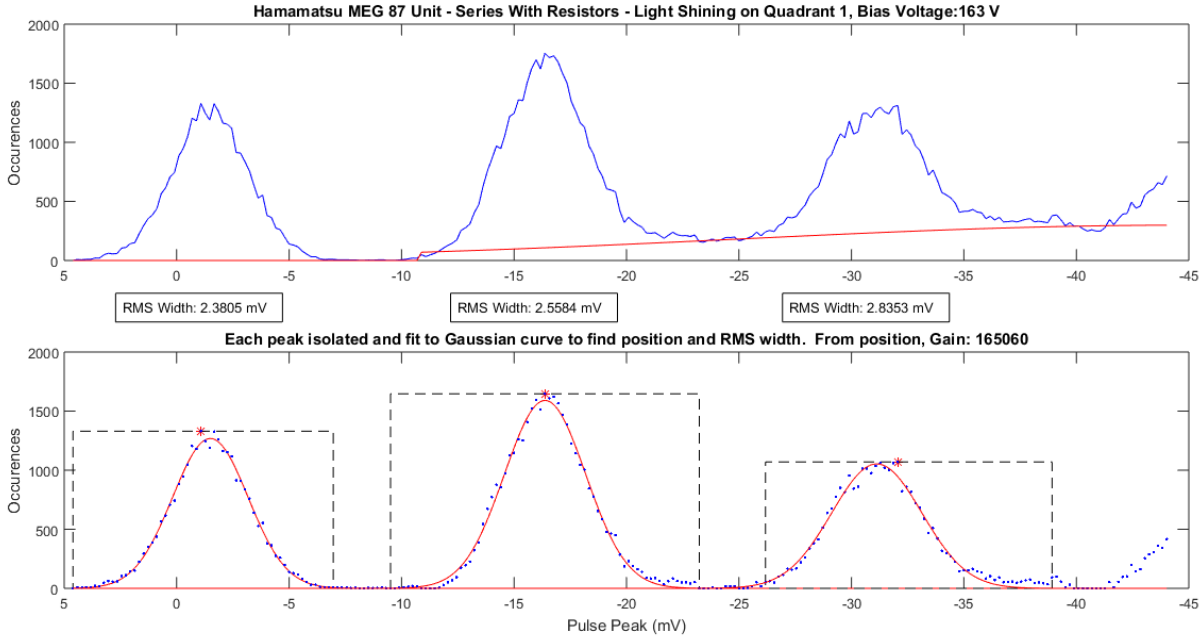

Figure C.19: Hamamatsu MEG Unit 87, Pulsed Light Histogram Analysis for Series Configuration with Light Shining on Quadrant 1- 163 V

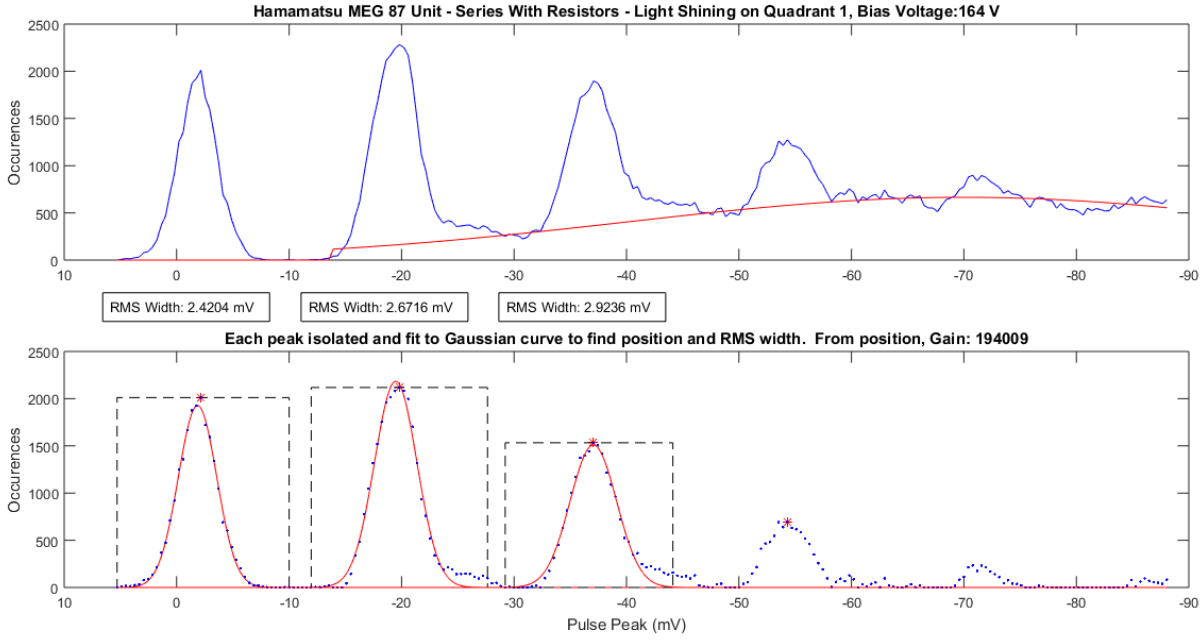

Figure C.20: Hamamatsu MEG Unit 87, Pulsed Light Histogram Analysis for Series Configuration with Light Shining on Quadrant 1- 164 V

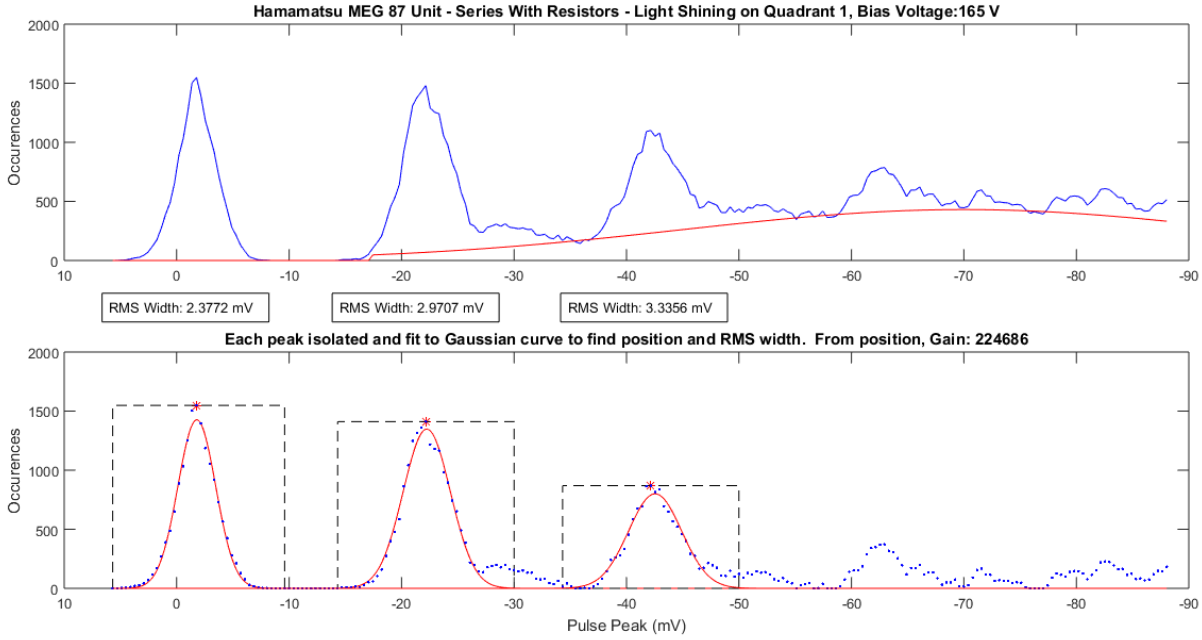

Figure C.21: Hamamatsu MEG Unit 87, Pulsed Light Histogram Analysis for Series Configuration with Light Shining on Quadrant 1- 165 V

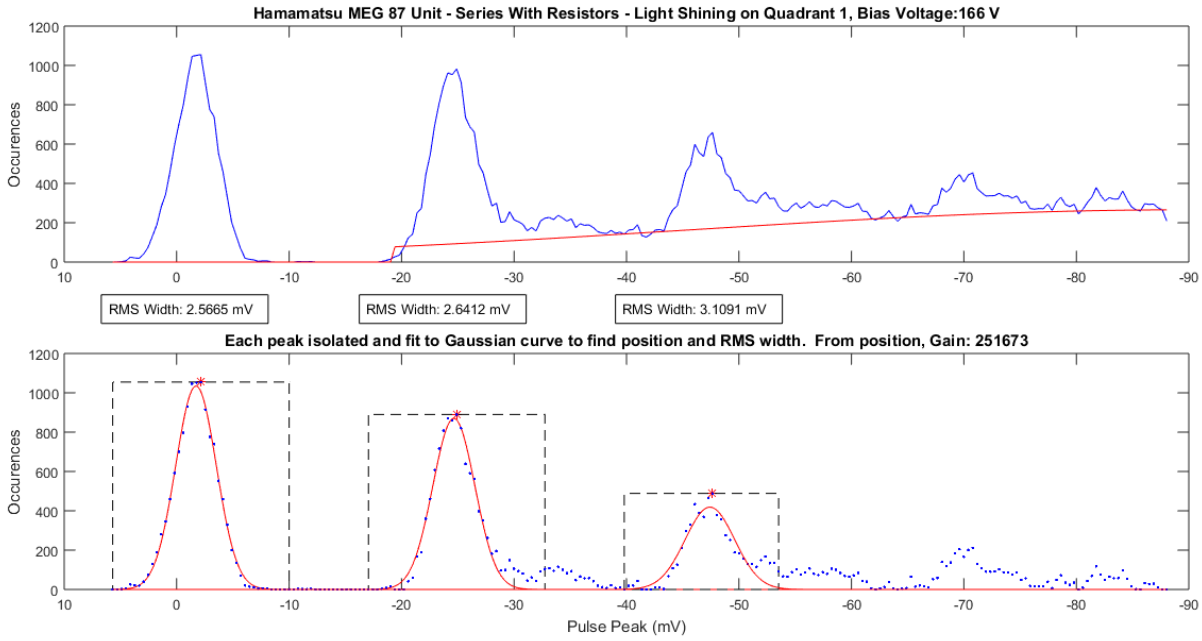

Figure C.22: Hamamatsu MEG Unit 87, Pulsed Light Histogram Analysis for Series Configuration with Light Shining on Quadrant 1- 166 V

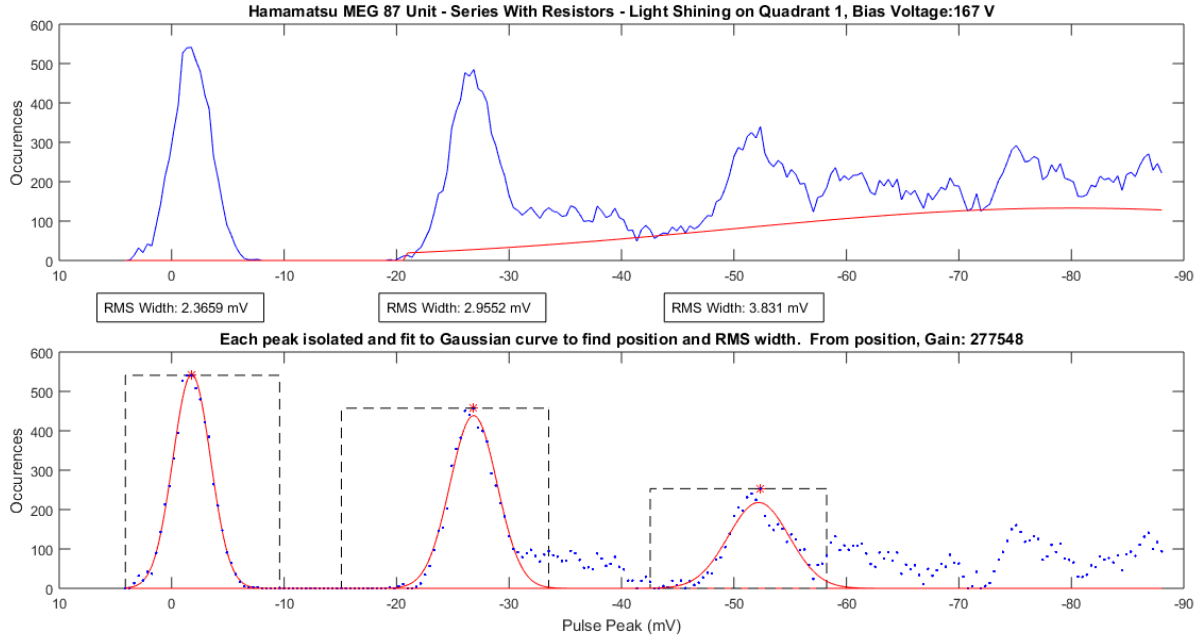

Figure C.23: Hamamatsu MEG Unit 87, Pulsed Light Histogram Analysis for Series Configuration with Light Shining on Quadrant 1- 167 V

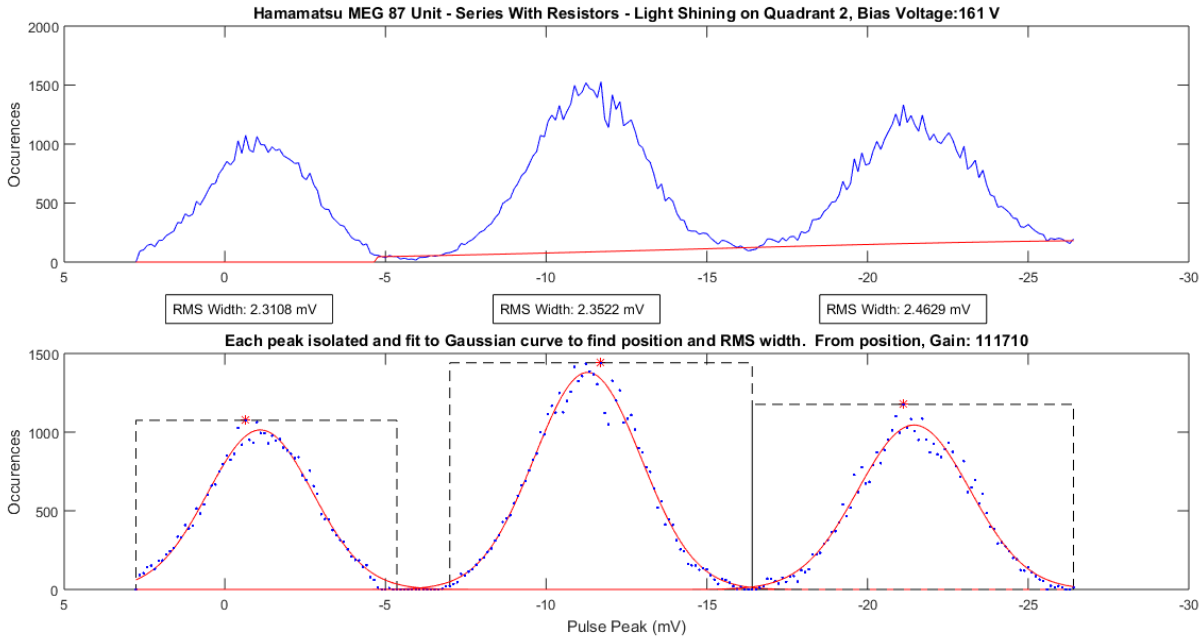

Figure C.24: Hamamatsu MEG Unit 87, Pulsed Light Histogram Analysis for Series Configuration with Light Shining on Quadrant 2- 161 V

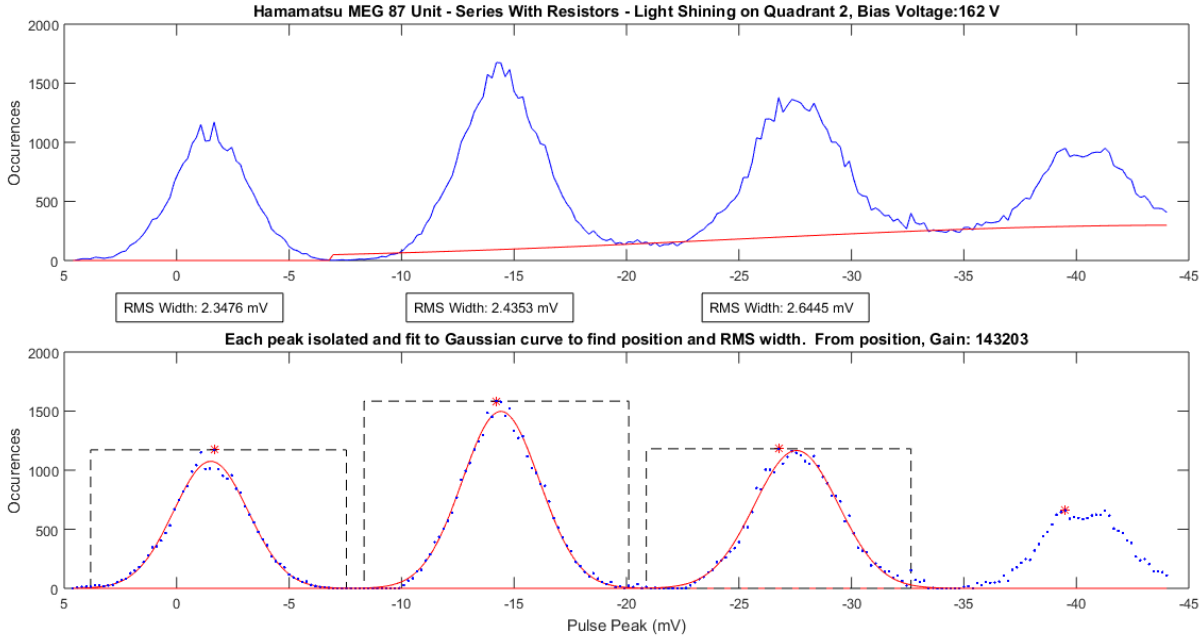

Figure C.25: Hamamatsu MEG Unit 87, Pulsed Light Histogram Analysis for Series Configuration with Light Shining on Quadrant 2- 162 V

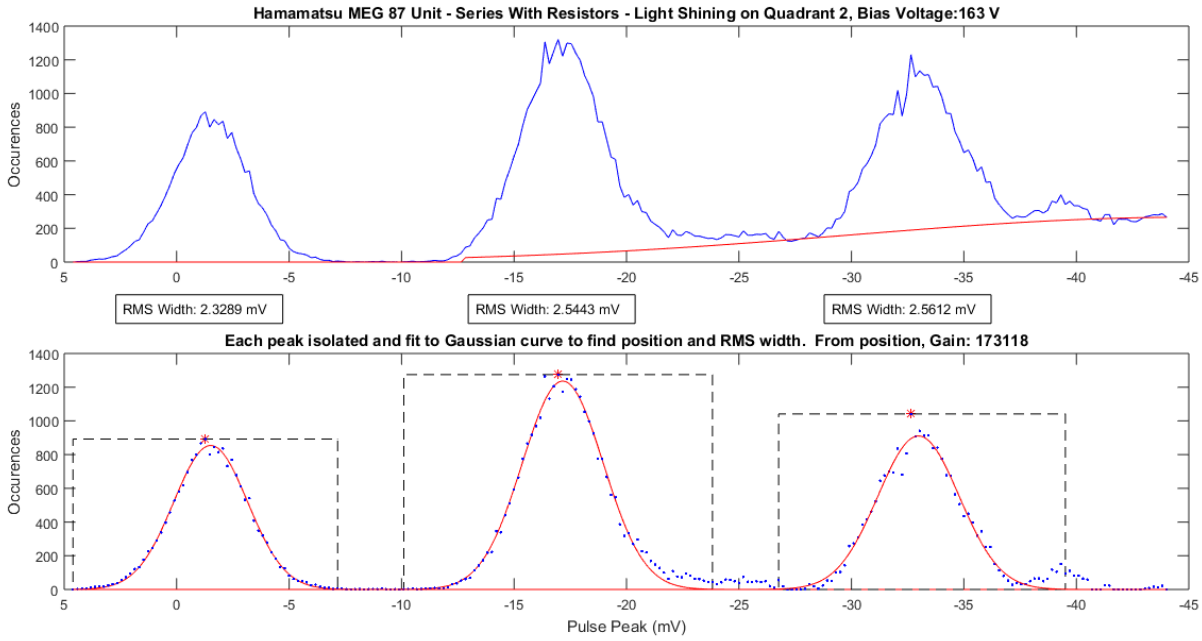

Figure C.26: Hamamatsu MEG Unit 87, Pulsed Light Histogram Analysis for Series Configuration with Light Shining on Quadrant 2- 163 V

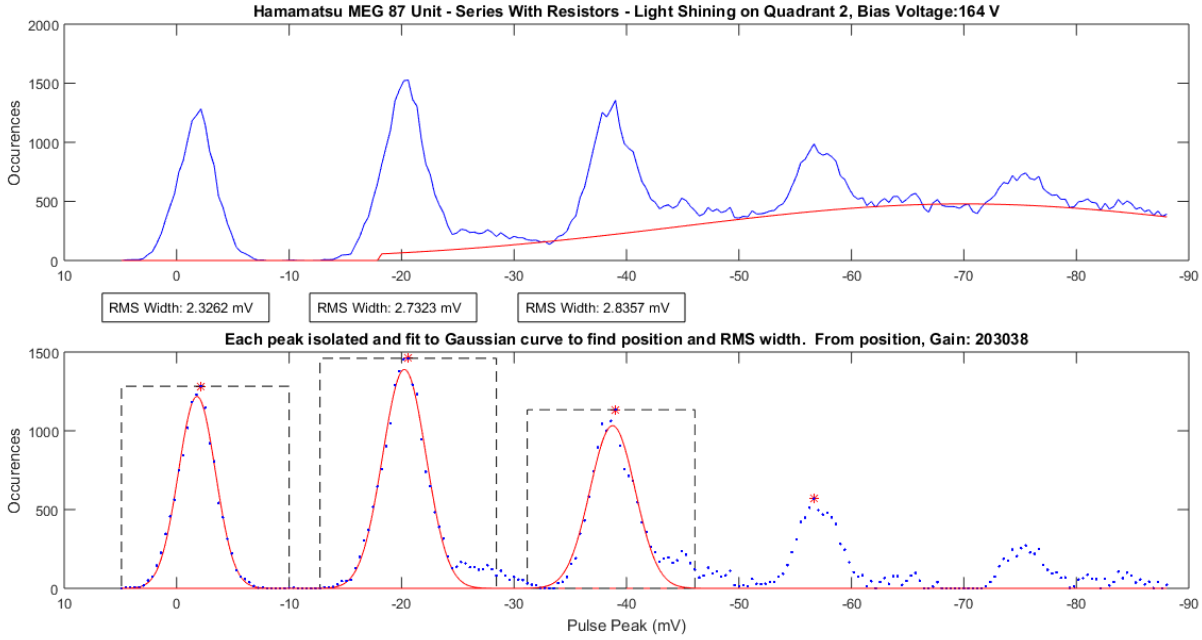

Figure C.27: Hamamatsu MEG Unit 87, Pulsed Light Histogram Analysis for Series Configuration with Light Shining on Quadrant 2- 164 V

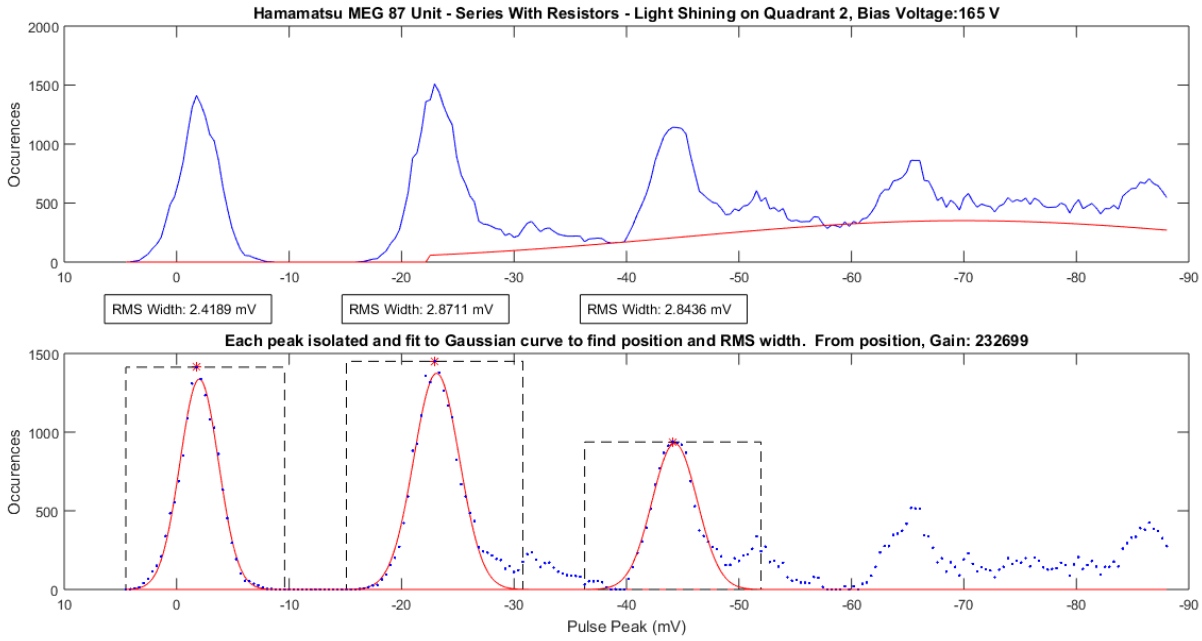

Figure C.28: Hamamatsu MEG Unit 87, Pulsed Light Histogram Analysis for Series Configuration with Light Shining on Quadrant 2- 165 V

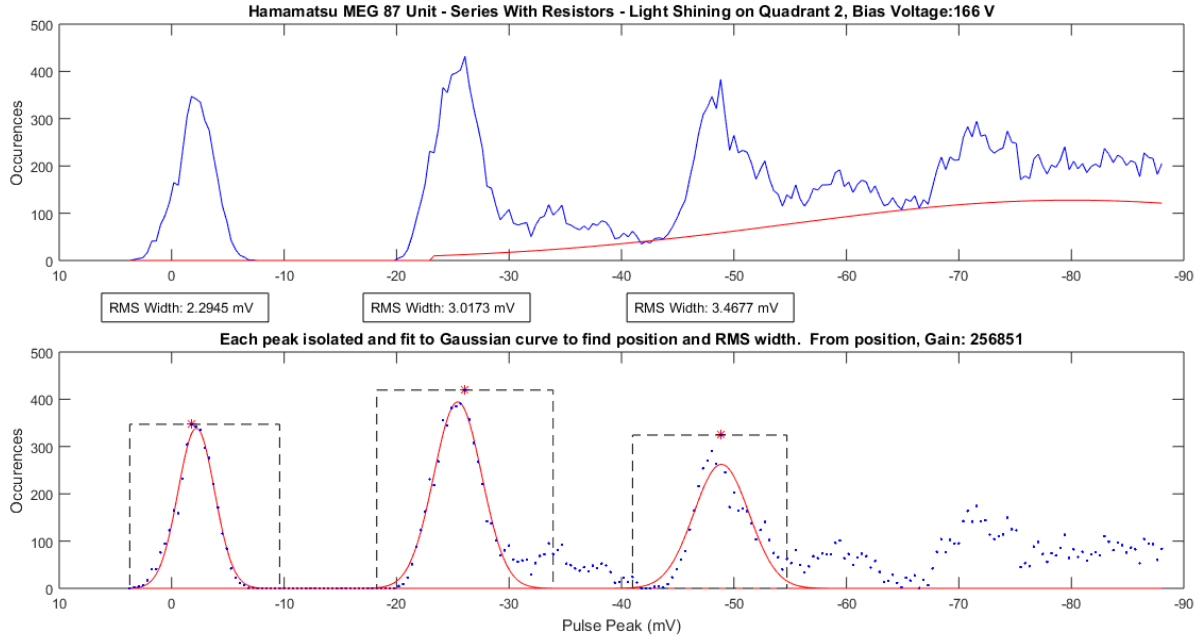

Figure C.29: Hamamatsu MEG Unit 87, Pulsed Light Histogram Analysis for Series Configuration with Light Shining on Quadrant 2- 166 V

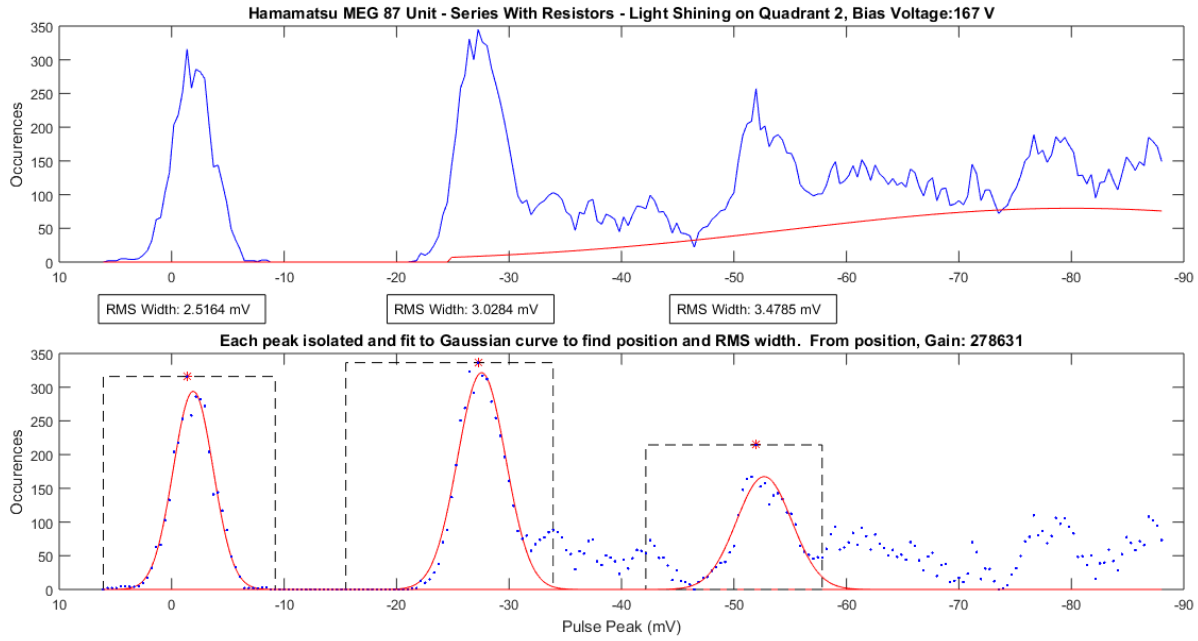

Figure C.30: Hamamatsu MEG Unit 87, Pulsed Light Histogram Analysis for Series Configuration with Light Shining on Quadrant 2- 167 V

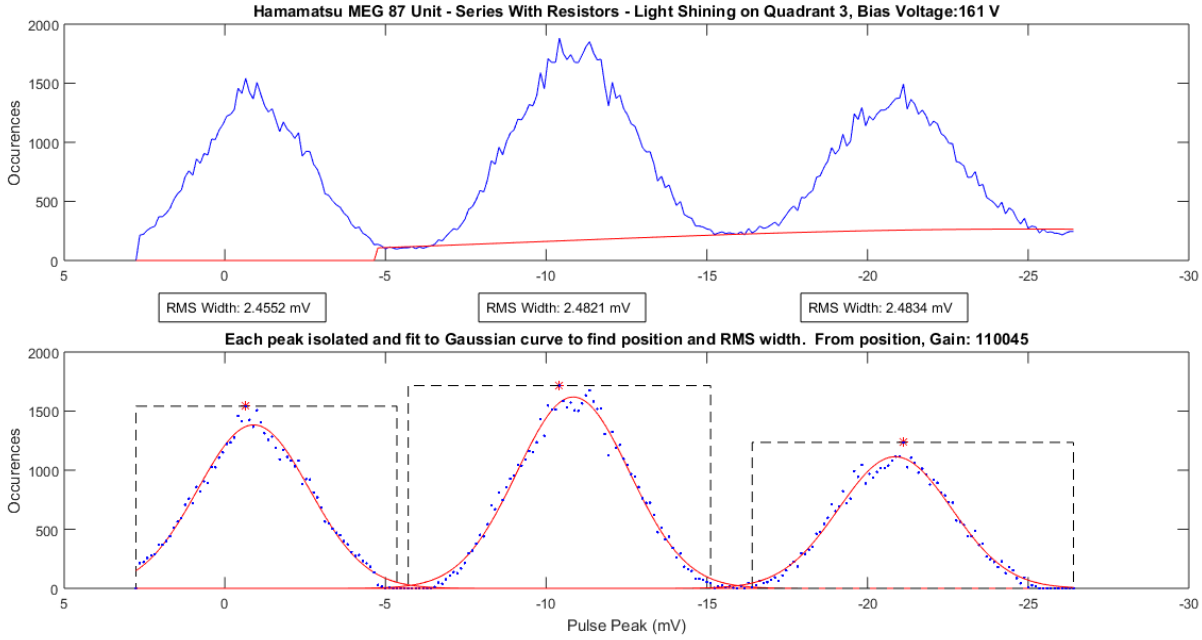

Figure C.31: Hamamatsu MEG Unit 87, Pulsed Light Histogram Analysis for Series Configuration with Light Shining on Quadrant 3- 161 V

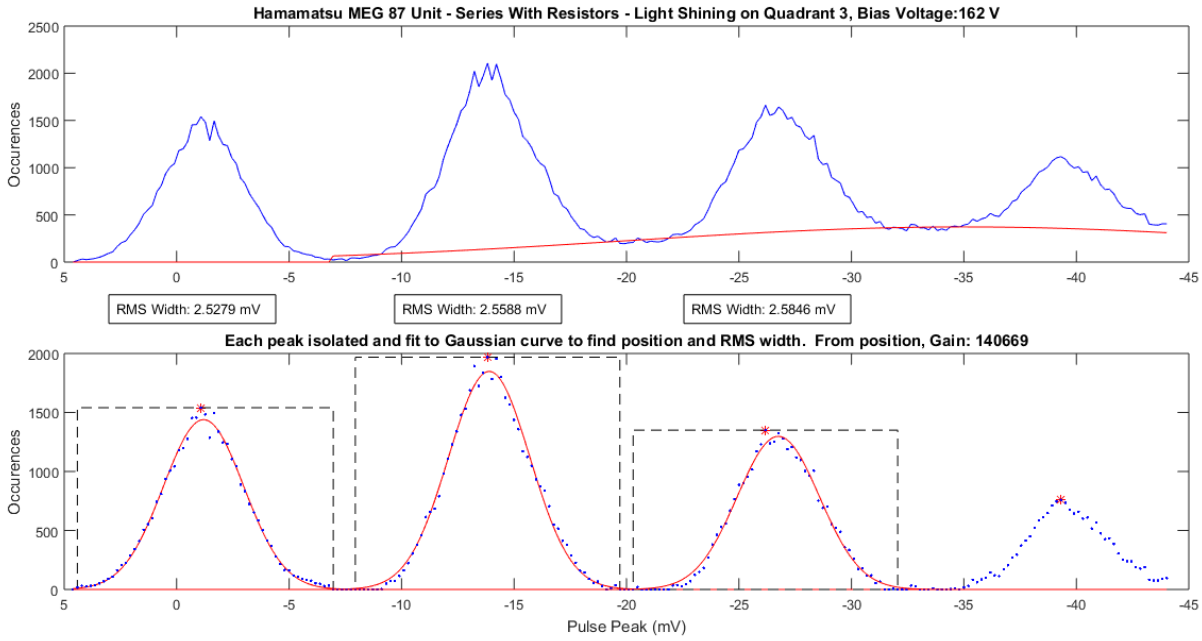

Figure C.32: Hamamatsu MEG Unit 87, Pulsed Light Histogram Analysis for Series Configuration with Light Shining on Quadrant 3- 162 V

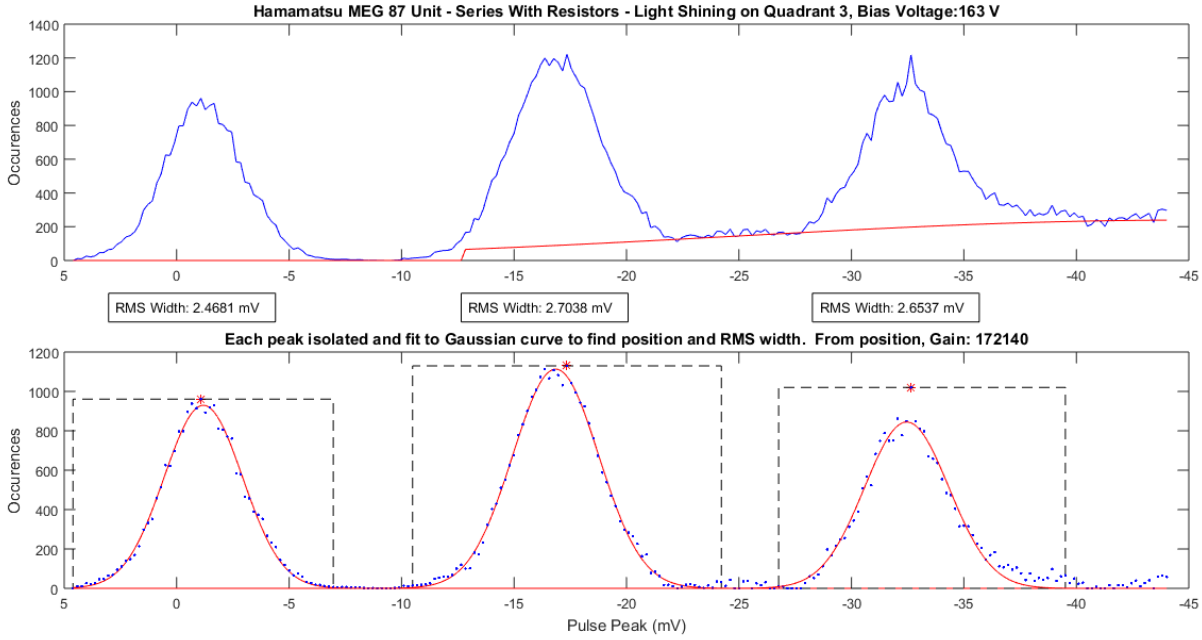

Figure C.33: Hamamatsu MEG Unit 87, Pulsed Light Histogram Analysis for Series Configuration with Light Shining on Quadrant 3- 163 V

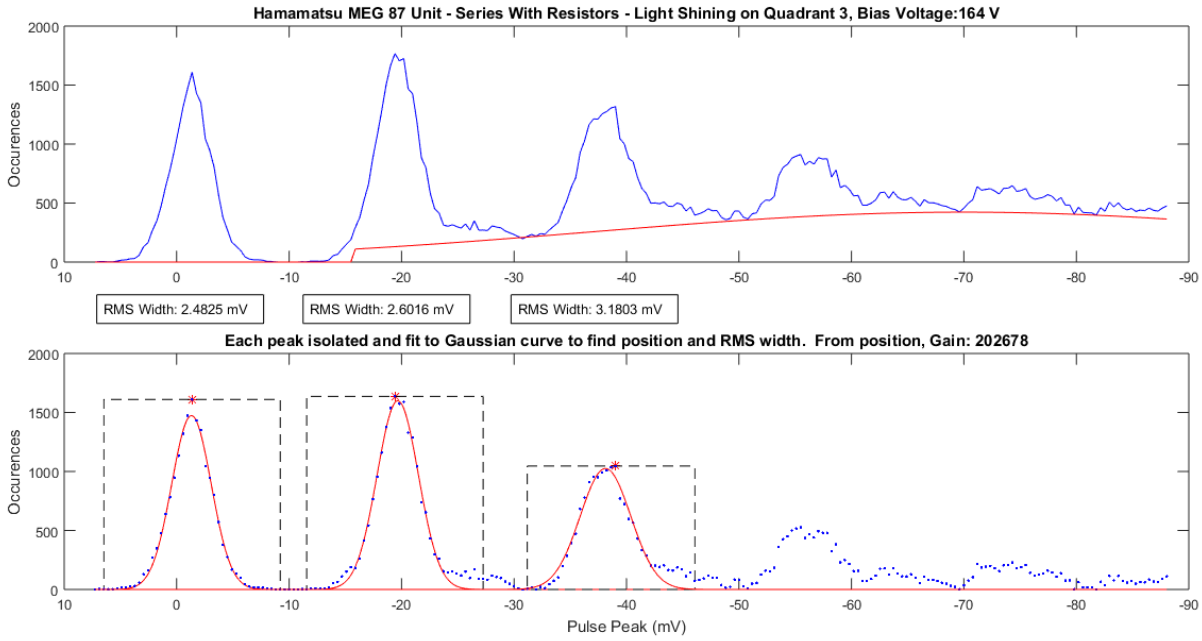

Figure C.34: Hamamatsu MEG Unit 87, Pulsed Light Histogram Analysis for Series Configuration with Light Shining on Quadrant 3- 164 V

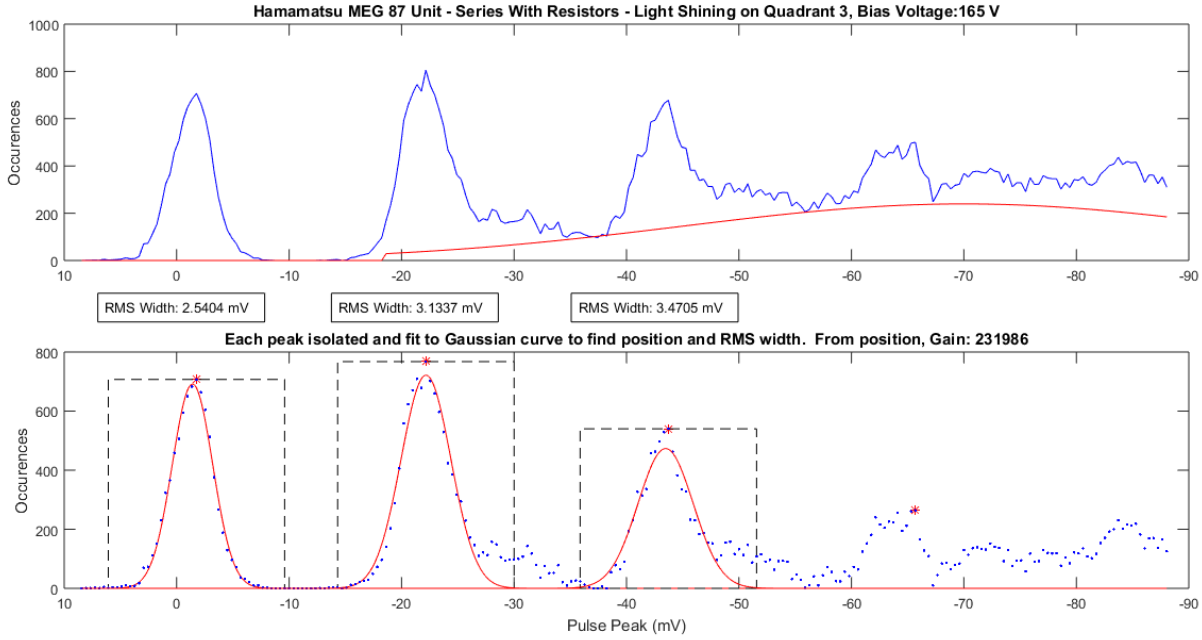

Figure C.35: Hamamatsu MEG Unit 87, Pulsed Light Histogram Analysis for Series Configuration with Light Shining on Quadrant 3- 165 V

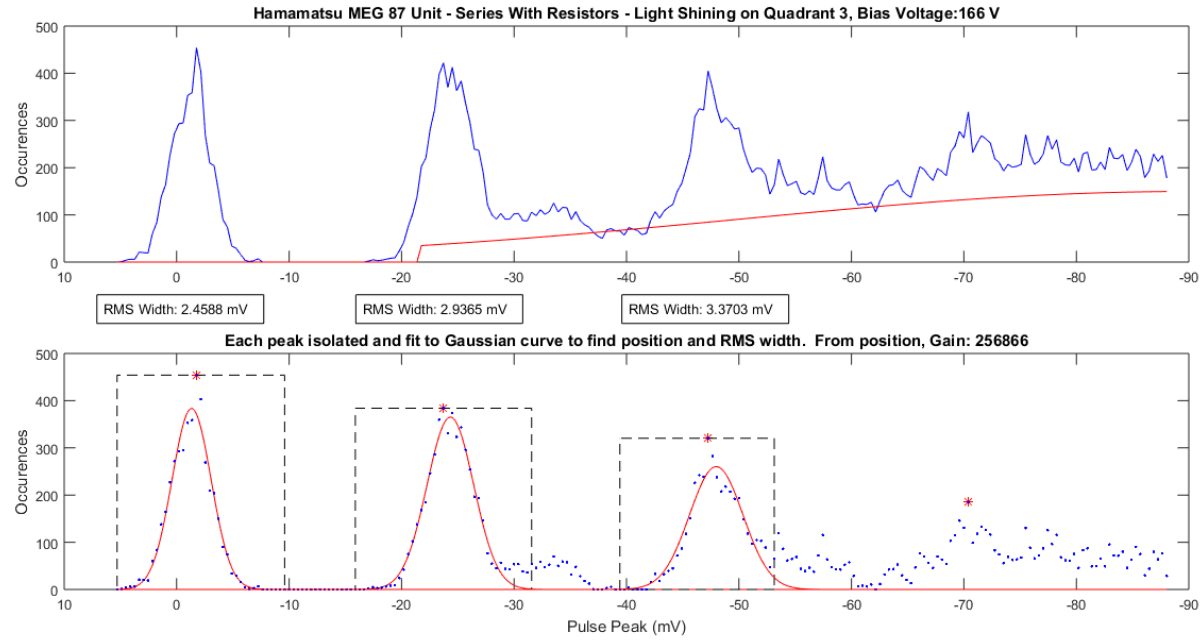

Figure C.36: Hamamatsu MEG Unit 87, Pulsed Light Histogram Analysis for Series Configuration with Light Shining on Quadrant 3- 166 V

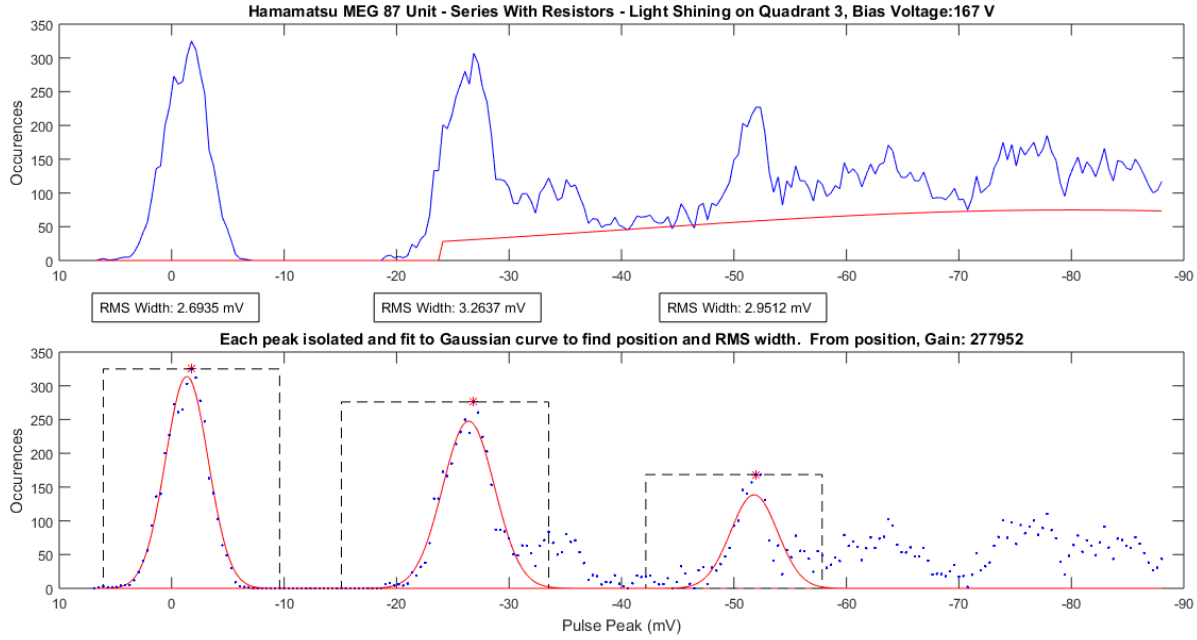

Figure C.37: Hamamatsu MEG Unit 87, Pulsed Light Histogram Analysis for Series Configuration with Light Shining on Quadrant 3- 167 V

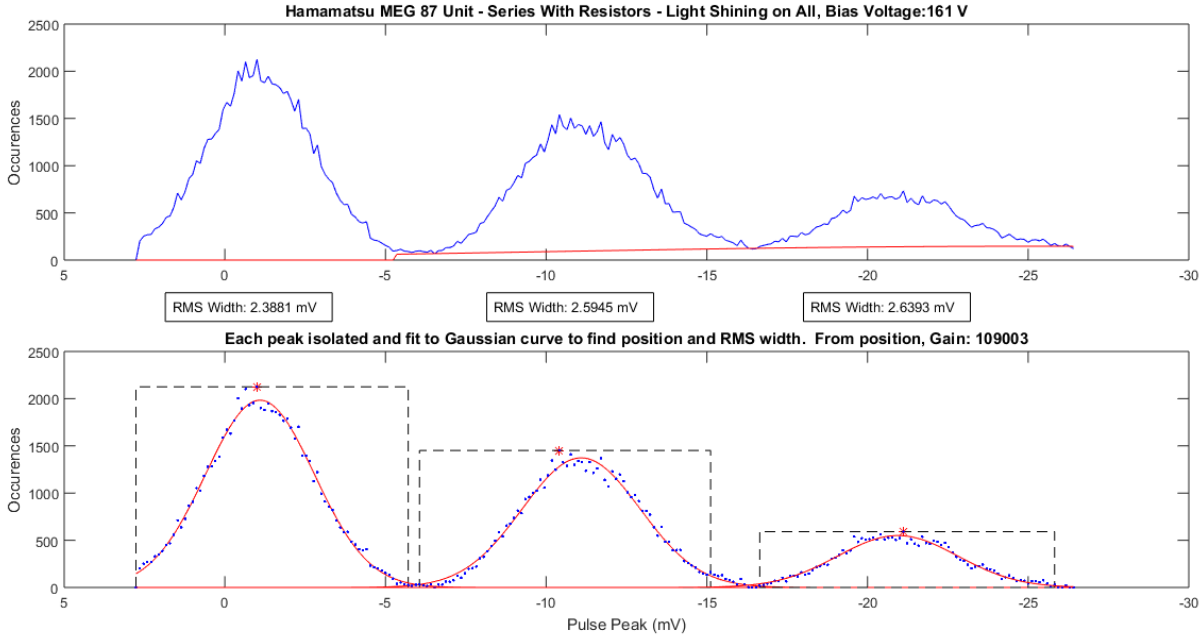

Figure C.38: Hamamatsu MEG Unit 87, Pulsed Light Histogram Analysis for Series Configuration with Light Shining on All Quadrants- 161 V

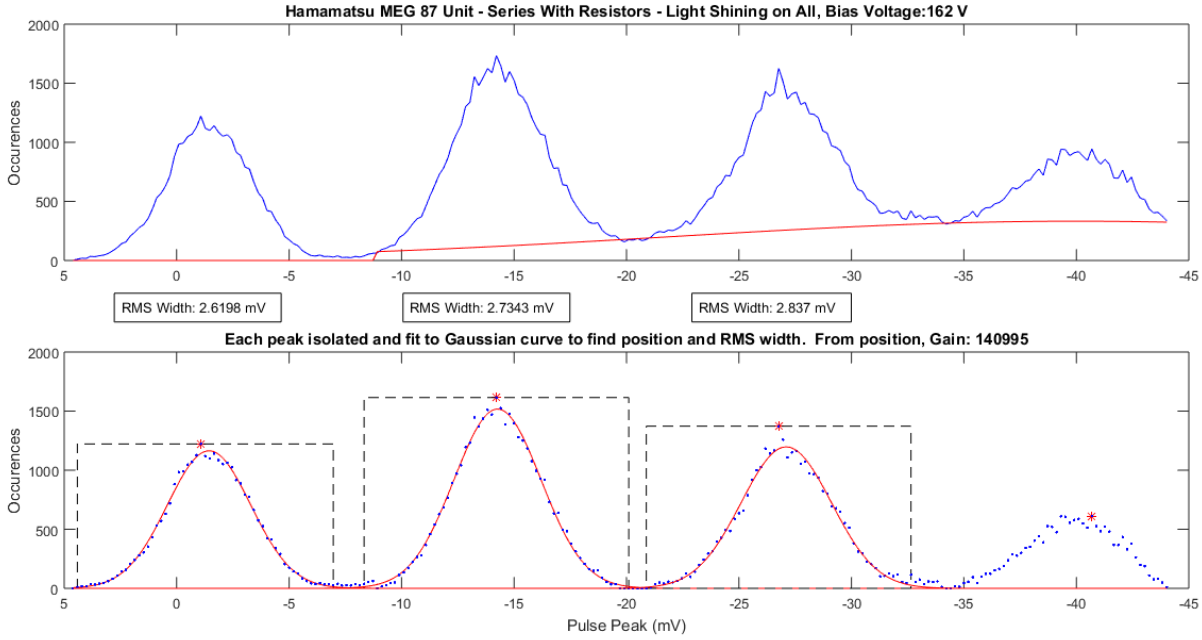

Figure C.39: Hamamatsu MEG Unit 87, Pulsed Light Histogram Analysis for Series Configuration with Light Shining on All Quadrants- 162 V

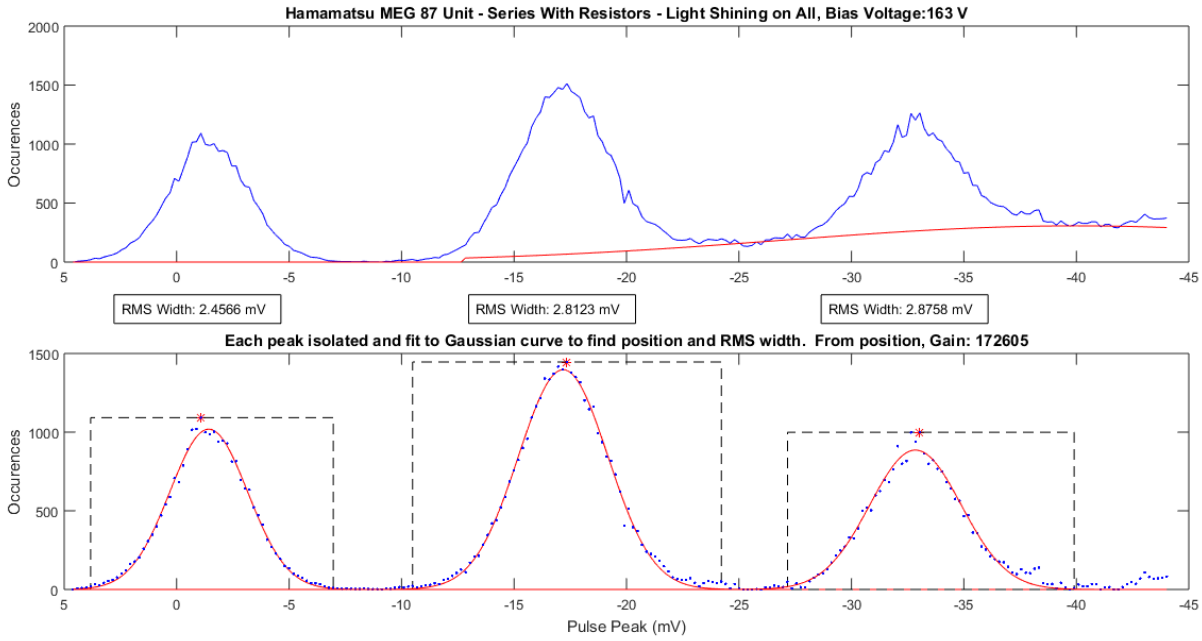

Figure C.40: Hamamatsu MEG Unit 87, Pulsed Light Histogram Analysis for Series Configuration with Light Shining on All Quadrants- 163 V

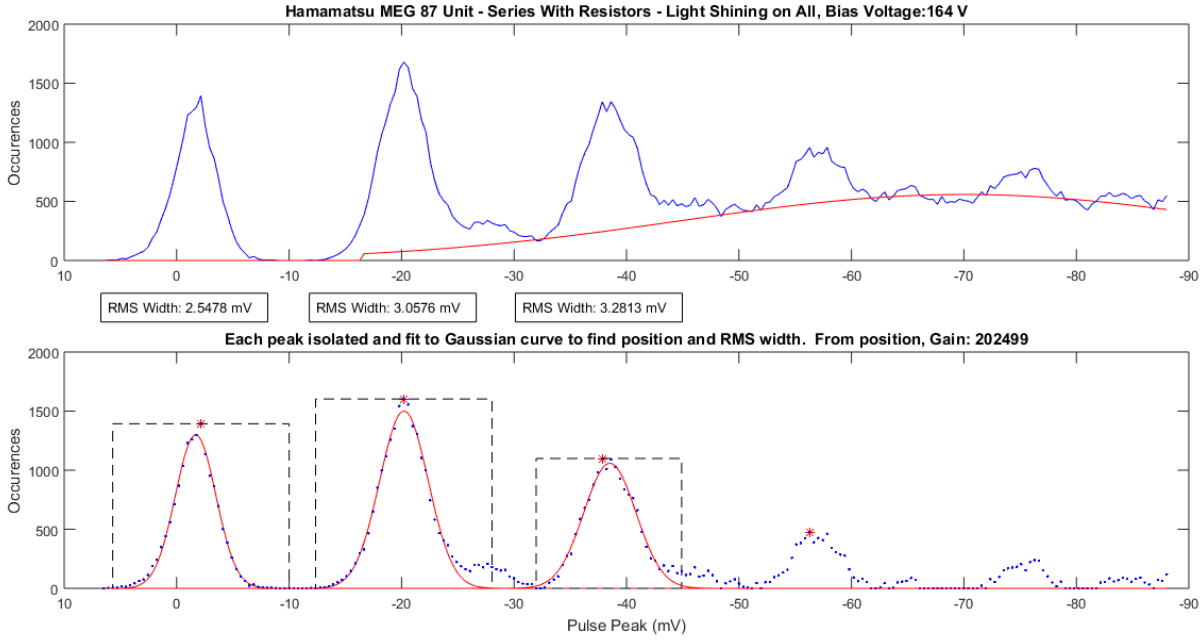

Figure C.41: Hamamatsu MEG Unit 87, Pulsed Light Histogram Analysis for Series Configuration with Light Shining on All Quadrants- 164 V

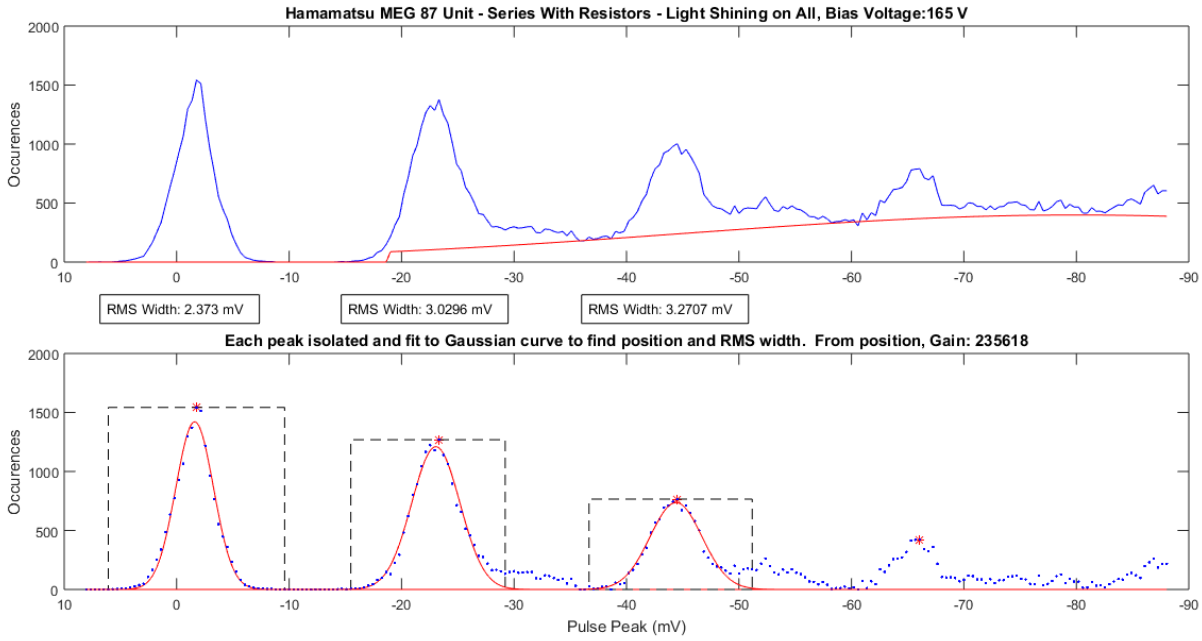

Figure C.42: Hamamatsu MEG Unit 87, Pulsed Light Histogram Analysis for Series Configuration with Light Shining on All Quadrants- 165 V

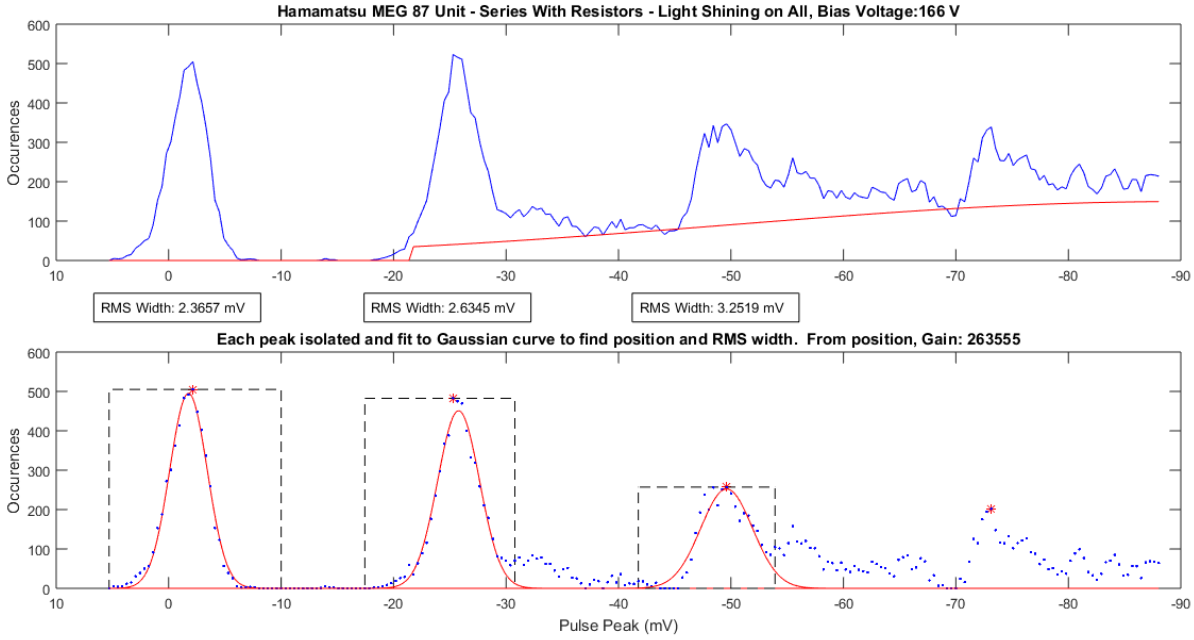

Figure C.43: Hamamatsu MEG Unit 87, Pulsed Light Histogram Analysis for Series Configuration with Light Shining on All Quadrants- 166 V

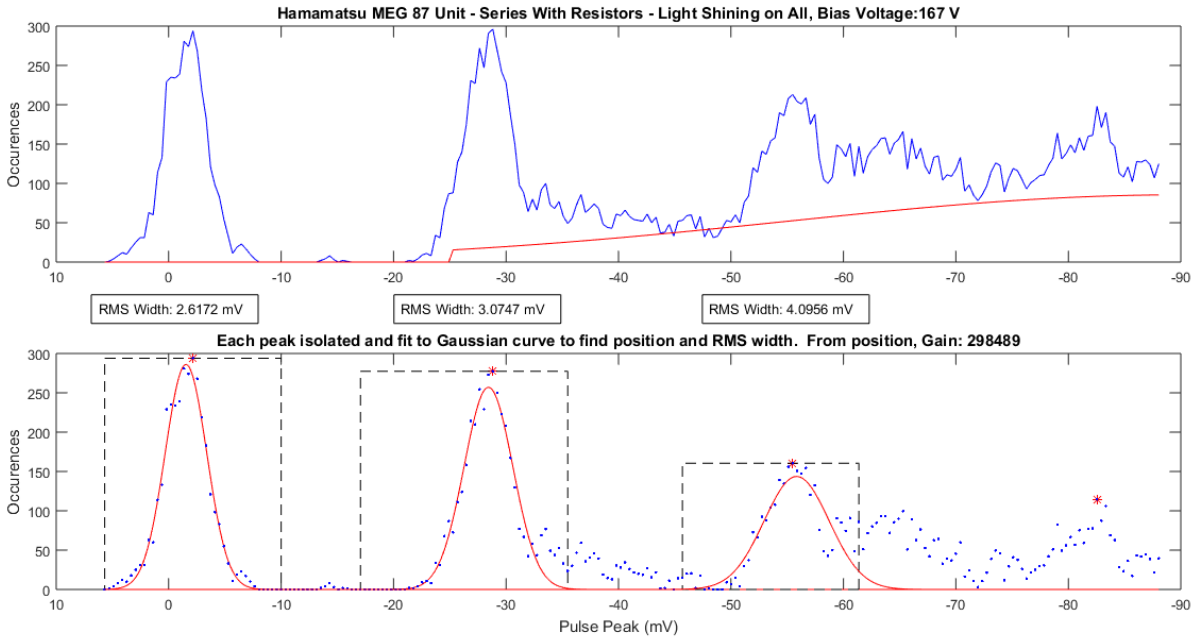

Figure C.44: Hamamatsu MEG Unit 87, Pulsed Light Histogram Analysis for Series Configuration with Light Shining on All Quadrants- 167 V